UCL Université catholique de Louvain

École polytechnique de Louvain (EPL)

epl

Perovskite Sr-doped $LaCrO_3$

An *ab initio* study

Dissertation presented by
Guillaume BRUNIN

for obtaining the Master's degree in
Physical Engineering
Option: Advanced Physics

Supervisor(s)
Geoffroy HAUTIER , Gian-Marco RIGNANESE

Reader(s)
Denis FLANDRE, Xavier GONZE

Academic year 2015-2016

Abstract

In this dissertation, the electronic and crystallographic structures of the perovskite Sr-doped $LaCrO_3$ ($La_{1-x}Sr_xCrO_3$) are theoretically investigated. It is a new p-type transparent conductive oxide (TCO), the Sr atoms replacing La ones to create holes as charge carriers. This material could lead to new routes for the design of future efficient p-type TCOs. Indeed, experimental measures show that the carrier transport may be due to small-polaron hopping in $La_{1-x}Sr_xCrO_3$. This phenomenon is usually not wanted for practical applications because of the low effective mass of the carriers, but in this case the conductivity of the material keeps a high value thanks to the high doping levels that are achieved. The purpose of the *ab initio* computations was thus to find these polarons in the studied materials, and to characterize their electronic properties. Computations were realized using GGA+U with the ABINIT package.

It appeared that polarons are indeed present in this material in the case of $x = 0.25$ and progressively disappear when x increases. There is a transition smearing temperature T^*, *a priori* different for each oxide, above which the material goes from the polaronic state to a metallic one. It has been possible to evaluate the difference of energy between the two states for $x = 0.25$ to about 63 meV (the polaronic state being the most stable of the two). This is nevertheless a rough approximation, and a more precise value could be obtained with a deeper analysis. The study led to the following hypothesis. Under a given fraction x^* of Sr (close to 0.65 according to experiments), the polaronic state would be more stable than the metallic one. Above x^*, the opposite would be true. In other words, a high concentration of Cr^{4+} atoms would favour the metallic state ($SrCrO_3$ having its Cr atoms in the Cr^{4+} state, while $LaCrO_3$ has its Cr atoms in the Cr^{3+} state). This has been observed for $x = 1$. The difference of energy between the two structures in the case of $SrCrO_3$ has been approximated to 43 meV, the metallic one being the most stable state. In order to test this assumption (the existence of a x^*), many computations should be run for different values of x, in order to be able to compute the difference of energy between the insulating and the metallic states in each case.

Acknowledgement

I would like to sincerely thank my two supervisors, Profs. Geoffroy Hautier and Gian-Marco Rignanese, for their precious help during this whole year. Their continuing involvement and the many answers they brought to my questions were crucial for the good development of this master thesis. Profs. Denis Flandre and Xavier Gonze are also heartily thanked in advance for reading this dissertation.

Computational resources have been provided by the supercomputing facilities of the Université catholique de Louvain (CISM/UCL) and the Consortium des Équipements de Calcul Intensif en Fédération Wallonie Bruxelles (CÉCI) funded by the Fond de la Recherche Scientifique de Belgique (F.R.S.-FNRS) under convention 2.5020.11.

Contents

List of Figures

List of Tables

Introduction

The development of new efficient transparent conductive oxides (TCOs) is a very active research field. Indeed, a lot of new technologies became available with the emergence of electrically conducting and optically transparent materials : more efficient solar cells and LEDs, touch panels,... If n-type TCOs are already quite efficient, the electrical conductivity of their p-type counterparts usually lies an order of magnitude lower. However, the use of efficient p-type TCOs together with n-type ones would open the door to even more new applications (transparent electronics like smart windows,...) thanks to the possibility to build transparent p-n junctions. The search for new p-type TCOs is thus very important from this point of view.

Both experimental and theoretical studies are crucial : the theory helps to understand the mechanisms behind the lack of efficiency of p-type TCOs, and how to get around this problem by finding new routes and design rules to develop new materials, while the experimental point of view is necessary to assess the theoretical results or even directly to find new and better materials. This dissertation lies in this problematic : it aims at describing theoretically the properties of a new p-type TCO in order to understand the experimental results associated to it. The recent papers of Zhang *et al.* [1, 2] describing the properties of the Sr-doped $LaCrO_3$ ($La_{1-x}Sr_xCrO_3$) are at the origin of this master thesis. Indeed, they measured a high conductivity linked to a quite good transmittance of light, both being needed for applications. The high conductivity is not due to a maximization of the hole effective mass, which is in this case very low, but to a high concentration of these carriers. They were indeed able to synthesize thin films for values of x up to 0.75, which corresponds to an extremely high doping level.

The first chapter of this dissertation is devoted to a description of the currently used TCOs, and explains the origin of the interesting properties of these oxides. A few examples of applications are also presented.

The experimental measures of the properties of $LaCrO_3$, $SrCrO_3$ and $La_{1-x}Sr_xCrO_3$ are then presented in the second chapter. For each material, the crystalline configuration is first described, followed by the electronic performances. The magnetic and optical characteristics are also introduced. These measures show that the electrical conductivity of $La_{1-x}Sr_xCrO_3$ can be modelled by a small-polaron transport over a given range of temperature and as long as $x < 0.65$. The basic concept of small-polarons and theories of the carrier transport in systems containing them are described in the third chapter. The optical properties of such systems are also introduced.

The fourth chapter describes the Hubbard model used to model the interactions between the electrons in the $3d$ orbitals of the Cr atoms of $La_{1-x}Sr_xCrO_3$. The description of the Density Functional Theory is not realized in the main body of this dissertation but is given in the appendices. This theory is at the basis of all computations realized for this dissertation. The results of the latter are presented in the fifth and last chapter. The determination of a correct Hubbard U parameter is first chosen in order to properly model the crystal properties. $LaCrO_3$ is then completely studied : its crystal configuration, band structure and density of states are computed. The comparison is realized with the experimental values of the obtained parameters. The effect of the doping of Sr atoms (replacing La ones) is then studied. The purpose is to find and isolate small polarons in the material in order to match the experimental behavior. It is then possible to understand the experimental properties described in the second chapter. $SrCrO_3$ is

finally treated in the same way. Unfortunately, there is a lack of experimental informations about this boundary of $La_{1-x}Sr_xCrO_3$. The formation energies of these doped materials are also computed, and the absorption spectrum and transmittance of $LaCrO_3$ are determined.

In the appendices, the reader will find a small chapter about the theory of semiconductors, written here to describe the basics of the physics of these materials. A brief description of the weak localization, which is present in the case of $SrCrO_3$, is also present. The Density Functional Theory is then described, and the convergence studies linked to the computations realized for this dissertation are completely detailed. The atomic positions in the different considered structures are reported in the last chapter.

Chapter 1

Transparent conductive oxides

Contents

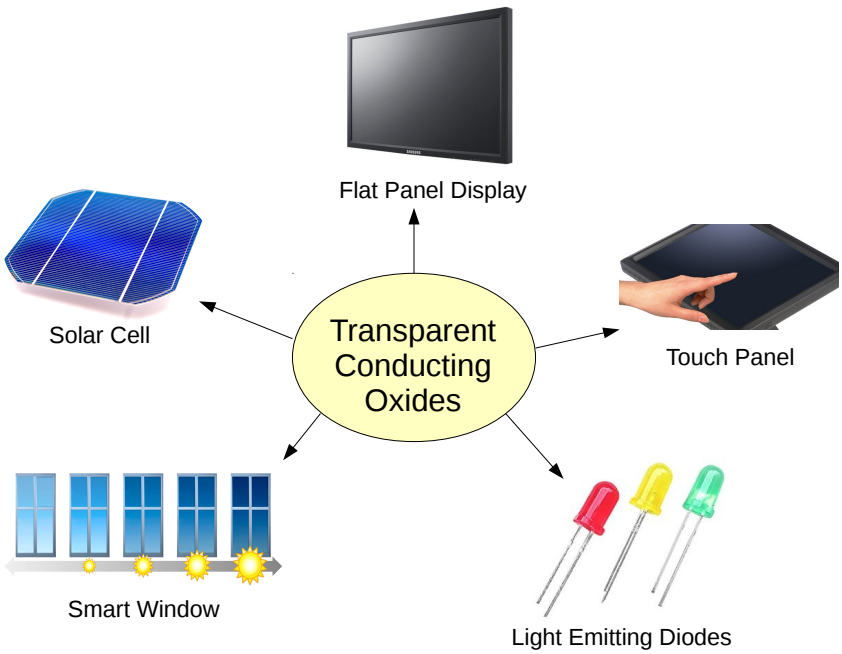

Transparent conductors (TCs) are materials which are both optically transparent and electrically conducting. They can be metals or oxides, in which case they are called transparent conductive oxides (TCO). TCs have been investigated for transparent electrode applications for optoelectronic devices such as solar cells, light-emitting diodes (LEDs), liquid-crystal displays (LCDs),... They are used everytime an application requires a transparent material able to conduct electricity. Many structures exist for such applications, but they usually integrate at least one thin layer of a TC or TCO (sandwiched structures) [3].

In the case of metallic TCs, the transparency is achieved by making the metal layer very thin. This usually leads to a non-uniform surface which can degrade their electrical properties [3]. Nevertheless, the metallic layer thickness can be optimized so that a transmittance of 80% (in the visible spectrum) combined to a very small resistance can be reached.

On the other hand, TCOs can have a much better optical transmittance and can also conduct charge carriers. This last property can be achieved in two different ways. First, the native defect (oxygen vacancies) concentration can be increased. The other way to make an oxide (originally insulating) conducting is by doping the material with higher or lower valence elements. The best TCOs currently have a carrier concentration of 10^{20} to 10^{21} cm^{-3} [3]. Of course, the optical and electrical properties of such an oxide depend on the nature, number and atomic arrangement of the metal ions in the structure, as well as on the presence of defects. In order to improve the understanding of TCOs and to develop new ones, the physics behind these materials needs to be clearly understood.

In this chapter, a small description of the currently used TCOs is first made. A characterization of their physical properties is then realized, which aims at explaining in a simple way how these materials can be both optically transparent and electrically conductive. A few applications of TCOs are described in the third section, to show the importance of the development of new (p-type) ones. Finally, the interest for $La_{1-x}Sr_xCrO_3$ is introduced.

1.1 Current TCOs

The best TCOs are currently n-type ones. The performances of p-type TCOs are still at least an order of magnitude lower than their n-type counterparts. This is why n-type TCOs have been extensively investigated, and why they are the most used ones. Thin films of In_2O_3, SnO_2, ZnO and their mixtures are the n-type TCOs with the most success for optoelectronic devices [4, 5]. Due to historical reasons, ITO (indium tin oxide, Sn doped In_2O_3) is still the predominant one. The 2007 United States Geological Survey estimated the total amount of indium reserves in the world to only 6000 tons [3]. Indium shortage may be a problem in the future and alternatives have thus been searched for. For example, AZO (aluminium zinc oxide, Al doped ZnO) films have been realized with very good electrical and optical properties. Moreover, the materials needed for this TCO are abundant, not toxic and cheap [3]. Nevertheless, the change from ITO to another high-performance n-type TCO in the industrial world is expected to be rather slow [3].

Two options are possible for further improving the performances of TCOs. Either new and more efficient materials have to be found, or better ways of making the existing TCOs have to be developed. It should also be mentioned that the performances of a TCO produced in a laboratory are always better than when it is produced by manufacturing companies. Indeed, the deposition rate in the industry needs to be far greater than what is done in laboratory. The TCO is then of lower quality and has poorer performances [5].

Research mainly focuses on developing new materials. If n-type TCOs are already very present in many devices, it is not the case of p-type ones because of the much larger effective mass of the holes compared to the electrons, as illustrated in Fig. 1.1. However, efficient p-type TCOs would be needed for all transparent electronics applications, like transparent transistors which could be integrated in smart windows [6, 7]. This difference between the performances of p-type

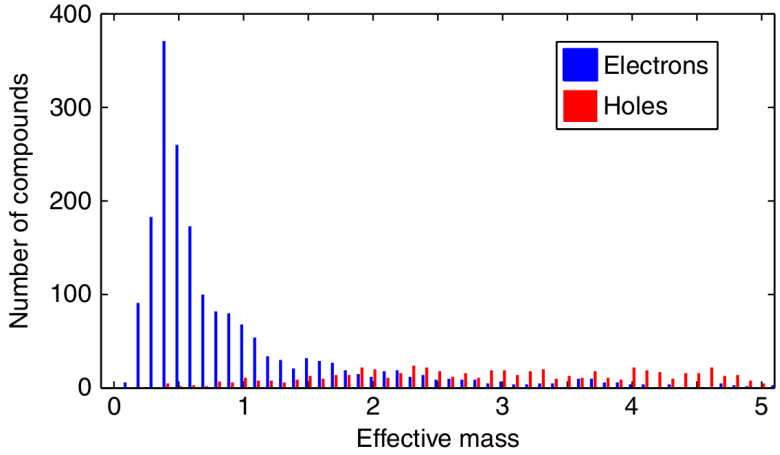

Figure 1.1: Computed effective mass distribution for electrons and holes in a vast selection of oxides [6].

and n-type TCOs also explains why current TCOs are used only for transparent electrodes, while they show an extraordinarily wide controllable conductivity range. Indeed, when efficient p-type TCOs will be commercialized, this will open the door to completely transparent electronic circuits [4, 7] (see Section 1.3.3).

1.2 Properties of TCOs

TCOs are interesting because they are optically transparent and electrically conducting. These two properties are explained here, and difficulties to produce efficient p-type TCOs are made clear.

1.2.1 Electrical properties

TCOs are obtained starting from semiconducting to insulating crystals. Their electrical conductivity is generated either by doping with higher or lower valence elements or by creating intrinsic defects like oxygen vacancies or metal interstitials [3]. The resistivity ρ can be used as a way to screen TCOs, and should be on the order of 10^{-4} Ω cm for practical viability [3].

The basic theory of semiconducting materials can be found in Appendix A. In TCOs, the carrier concentration is usually limited by the solubility of dopants or by the plasma frequency (see next section). The mobility of these carriers is limited by the scattering processes in the lattice. Several scattering processes can take place in a TCO : scattering by ionized impurities, neutral centers, thermal vibrations of the lattice, structural defects, grain boundaries... The main process depends on the carrier concentration and on the crystal quality [3]. The carrier concentration is usually quite high in TCOs. In this case, the main scattering process is the scattering by the ions. All these considerations are based on the assumption that the carriers are free in the crystal. It may happen that this hypothesis is not true. It is for example the case of polaronic materials, as it is described in Chapter 3. Future TCOs should be developed such that the carrier mobility is maximized in order to increase the conductivity [5]. The effective mass should be minimized, or the relaxation time maximized.

The main cause of the difference of performance between n-type and p-type TCOs is the difference between the effective masses of the electrons and the holes. Indeed, the top of the valence band of these oxides mainly shows O $2p$ character, which orbitals are very localized [6]. This leads to flat valence bands (see Fig. 1.2), and hence very high hole effective masses (the effective mass is inversely proportional to the curvature of the band). However, the nature of the top of the conduction band is a hybridization of the O $2p$, O $2s$ (minor contribution) and

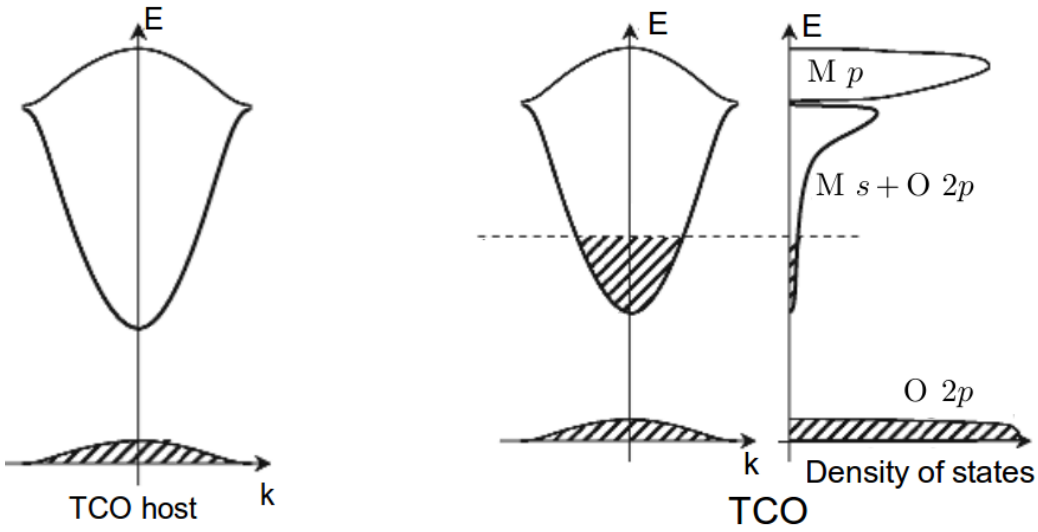

(a) (b)

Figure 1.2: Schematic representation of the band structure of (a) a TCO host and (b) a TCO with a degenerate doping. The valence band of the TCO originates from the interaction between the O $2p$ and the metal M s states, as it is represented by the density of states. Adapted from Ref. [8].

the s orbitals of the metal atoms (see Fig. 1.2), which leads to a higher dispersion and hence to low electron effective masses [6]. Fig. 1.1 represents the mass distribution of a large group of oxides. The main objective in order to get new effective p-type TCOs is then to find materials which have a less localized oxygen valence band. This is the case for TCOs containing copper, because in this case the oxygen orbitals hybridize with the copper ones, which decreases the oxygen character at the top of the valence band [6]. New routes and design rules still need to be found in order to develop new materials with lower hole effective masses.

1.2.2 Optical properties

TCOs are transparent for a certain window of energy of the incoming light [3, 9]. This window depends on the material, and should contain the visible light for any practical use. The upper bound of this window is determined by the effective band gap E_g. Indeed, when photons have an energy larger than the band gap, they may be absorbed by electrons in the valence band which will be able to jump into a higher energy state of the conduction band. The TCO will be transparent for light with an energy slightly smaller than the band gap. But there is also a lower bound : photons of a too small energy will be reflected by the material. This is due to plasma resonance of the electron gas in the conduction band, and the frequency at which the transition happens is called the plasma frequency ω_p : below this frequency (or below the energy $\hbar\omega_p$), the material is reflective and light cannot penetrate it. The Drude model leads to a derivation of the plasma frequency [9] :

$$\omega_p = \sqrt{\frac{ne^2}{\epsilon_0 m^*}} \tag{1.1}$$

where n is the density of free carriers in the material, e is the fundamental charge, ϵ_0 is the vacuum permittivity and m^* is the carrier effective mass.

The positions of the two boundaries defining the window where a TCO is transparent are related to the carrier concentration, their effective mass and to the band gap of the material. When the carrier concentration increases, both boundaries shift to higher energies [3]. Fig. 1.3 represents the window and the shifts for different carrier concentrations in the case of GZO (Ga

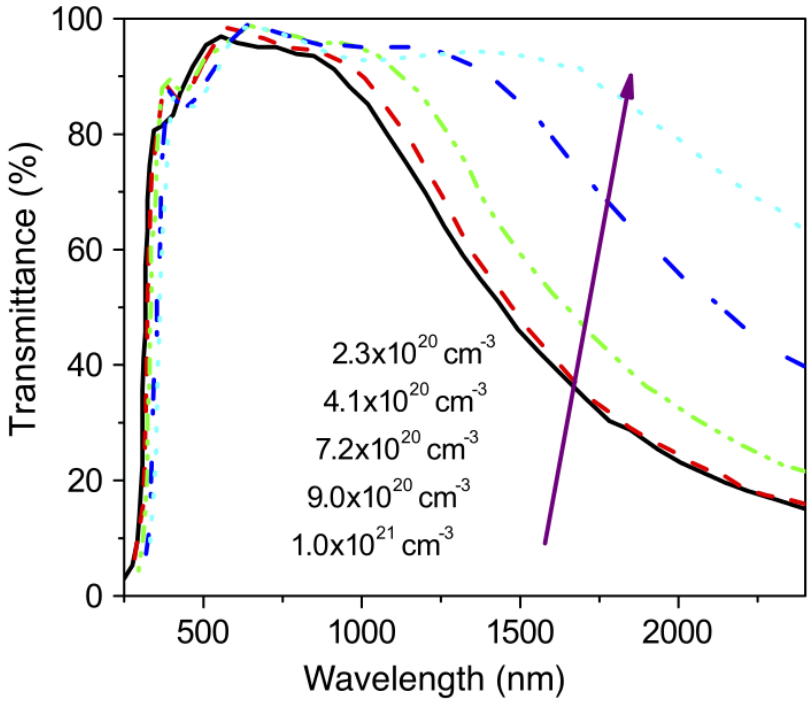

Figure 1.3: Transmittance of films of GZO (Ga doped ZnO) for different carrier concentrations [3].

doped ZnO) films. As it can be seen, the upper boundary (lower in wavelength) does not change a lot with the carrier concentration. However, the lower boundary is very affected.

The plasma frequency depends on the carrier concentration. So does the conductivity. Both properties are thus interconnected. In order to have a good conductivity, the carrier concentration should be large. But in this case, the plasma frequency increases, and may begin to lie in the visible spectrum. A compromise between the conductivity and the transmittance must be found, and TCOs are materials for which it is possible to obtain a transmittance window in the visible light with a sufficiently high conductivity. Another way to increase the conductivity without increasing the carrier concentration is by improving the carrier mobility in the material. In this way, the conductivity can be high enough with a lower carrier concentration, and the material may be transparent for the whole visible spectrum. This is the main reason for the continuing search for new materials with a high carrier mobility.

The specific choice of a material and a carrier concentration depends on the application. For example, an LED emits light in a narrow range around the emission wavelength, and the transparency should be effective for this window only [3]. On the other hand, solar cells need a high transparency in the whole solar spectral range in order to improve their efficiency [3].

1.3 Applications of TCOs

TCOs find many applications in optoelectronics, flat-panel display, light-emitting devices, solar cells,... Only a few of them are described here.

1.3.1 Solar cells

The basic principle of a solar cell relies on the photovoltaic effect. Incident light is absorbed in the depletion zone of a p-n junction, which may create electron-hole pairs (if the energy of the photons is greater than the band gap of the used semiconductor). The carriers are transported

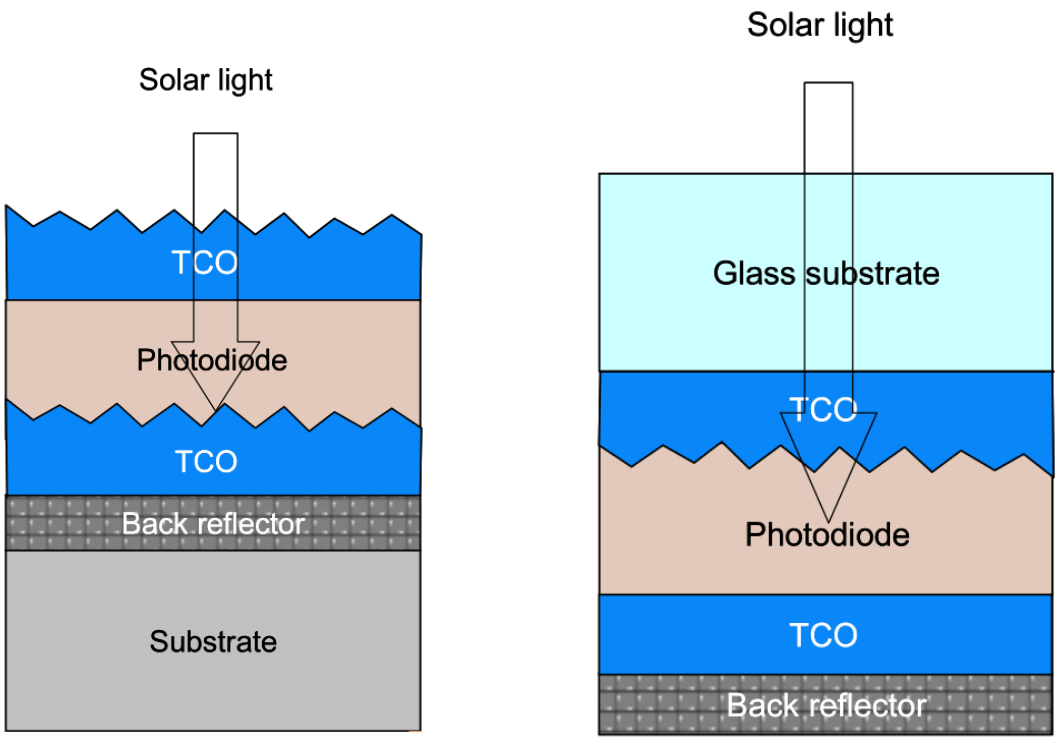

(a) (b)

Figure 1.4: Schematic cross-section of thin-film solar cells in the (a) substrate and (b) superstrate configurations [10].

in opposite directions due to the electric field in the depletion zone and are then used to generate power.

The 1st generation solar cells rely on bulk silicon wafers for absorbing light. The band gap of silicon is indirect, which leads to a low optical absorption coefficient [10]. A thick layer of silicon (typically of several hundreds microns) is then needed to absorb as much light as possible. Many precise designs of the wafers are possible. The theoretical limit of the efficiency of silicon solar cells is about 28%, and the current record for single-crystal silicon cells is 25% [10]. The further improvement of the price per kWh will thus mainly be obtained by decreasing the production cost of the best silicon wafers.

The 2nd generation solar cells, based on thin films, have the same limit in the efficiency as the 1st generation ones. The advantage is the reduction of the production cost because they do not need a semiconductor wafer substrate [10]. In this technology, a TCO layer is used for the front contact. The advantage of this TCO layer is that it can play the role of the electrode over the whole surface of the cell while being transparent. Fig. 1.4 represents two different configurations for these cells. The efficiency of this kind of cell depends on many parameters, among which the resistivity and the transmission of the used TCO [10]. Ref. [10] precisely describes the diversity of technologies that have been developed to increase the efficiency of these cells.

1.3.2 LEDs

An LED can be seen as the opposite of a solar cell. An injection current flows through a p-n junction, which leads to electron-hole pairs annihilation. These recombinations lead to the emission of photons whose energy corresponds to the band gap of the used semiconductor (or at least to the difference of energy between the electrons and the holes). The recombinations can also be non-radiative, but this case will not be considered here.

The properties of TCOs have many advantages for LEDs. First, their transparency is useful

to increase the efficiency of LEDs : more photons will be able to get out of the recombination zone if the contact is transparent than when it is a thin metal film, as it is currently the case [3, 11]. Second, their electrical conductivity is needed in order to be able to bring the carriers which recombine. Moreover, the degradation of an LED at high injection currents can be due to a poor conductivity of the contact. Ohmic contacts obtained using appropriate TCOs could lead to a decrease of this resistivity and then an increase of the lifetime of LEDs [3]. These advantages of TCOs over metallic electrodes could lead to a great improvement of the performances of LEDs, and eventually to a reduction of their cost on the long term (which is what is sought with LEDs).

1.3.3 Transparent electronics

Transparent electronics is an emerging technology field. As its name suggests, it concerns all the transparent electronic circuitry and optoelectronic devices [12]. For example, the windshield of a car could display information for the driver. Windows could be used to produce electrical power. The principles behind this technology would be the same as for the classic non-transparent electronics. The junction between p and n-type semiconductors (to form transistors, diodes,...) is the building block of current electronic devices. That means that transparent semiconductors should be used for transparent electronics. The use of p and n-type TCOs in this technology is therefore obvious.

1.4 Perovskite Sr-doped $LaCrO_3$ as a new p-type TCO

The need of efficient p-type TCOs is clear. Research is very active in this field. The papers of Zhang *et al.* (Refs. [1, 2]) describe the properties of the pervovskite Sr-doped $LaCrO_3$ as a new p-type TCO. They found out very interesting properties : the material remains half transparent for a very high doping level over a large frequency window (the transmittance is over 50% for a thickness of 80 nm and a doping level of 50%). The high doping helps achieving a high conductivity (54 S cm^{-1} for the same film). This material is probably not the one that will be used in future applications, but it has very interesting properties that could lead to new routes in the design of new p-type TCOs. These properties are described in the next chapter and investigated in Chapter 5.

Chapter 2

$La_{1-x}Sr_xCrO_3$ properties

Contents

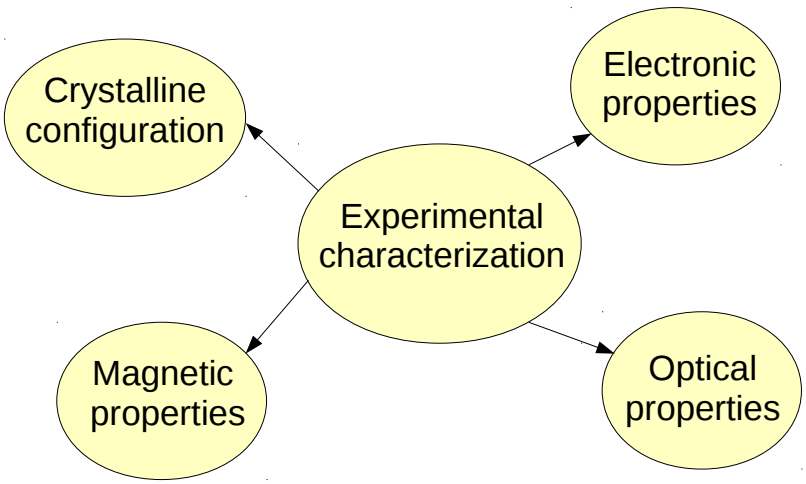

The studied material is a perovskite Sr-doped $LaCrO_3$. In this chapter, $LaCrO_3$ is thus first completely presented by showing its crystalline configuration and experimentally determined properties (electrical, magnetic and optical). Then, perovskite $SrCrO_3$ is also introduced. Finally, the effect of the doping of $LaCrO_3$ by Sr atoms is described.

2.1 Lanthanum chromate $LaCrO_3$

The measured crystalline configuration of $LaCrO_3$ is first detailed. Its electric and magnetic properties are then described. A small point about its optical properties concludes this first section.

2.1.1 Crystalline configuration

Lanthanum chromate $LaCrO_3$ is a perovskite material which has an orthorhombic distorted structure at room temperature [1, 13, 14]. Its space group is *Pbnm* (No. 62) [15, 16, 17]. The unit cell (at room temperature) of $LaCrO_3$ is represented in Fig. 2.1(a), and the octahedral coordination is shown in Fig. 2.1(b). The structure changes from orthorhombic to rhombohedral distorted around 540 K [13, 14, 18] and the space group of $LaCrO_3$ then becomes $R\bar{3}c$ (No. 167). The cell parameters for these two different structures are given in Table 2.1. They have been measured by diffraction techniques on powder samples prepared by the standard solid-state reaction method which produces polycrystals. The molar volume of $LaCrO_3$ represented in Fig. 2.2(a) shows that there is a volume compression at the phase transition, and Fig. 2.2(b) shows that this change of volume is mainly due to a shrinkage of $[CrO_6]$ octahedra while the $[LaO_{12}]$ polyhedra keep the same volume.

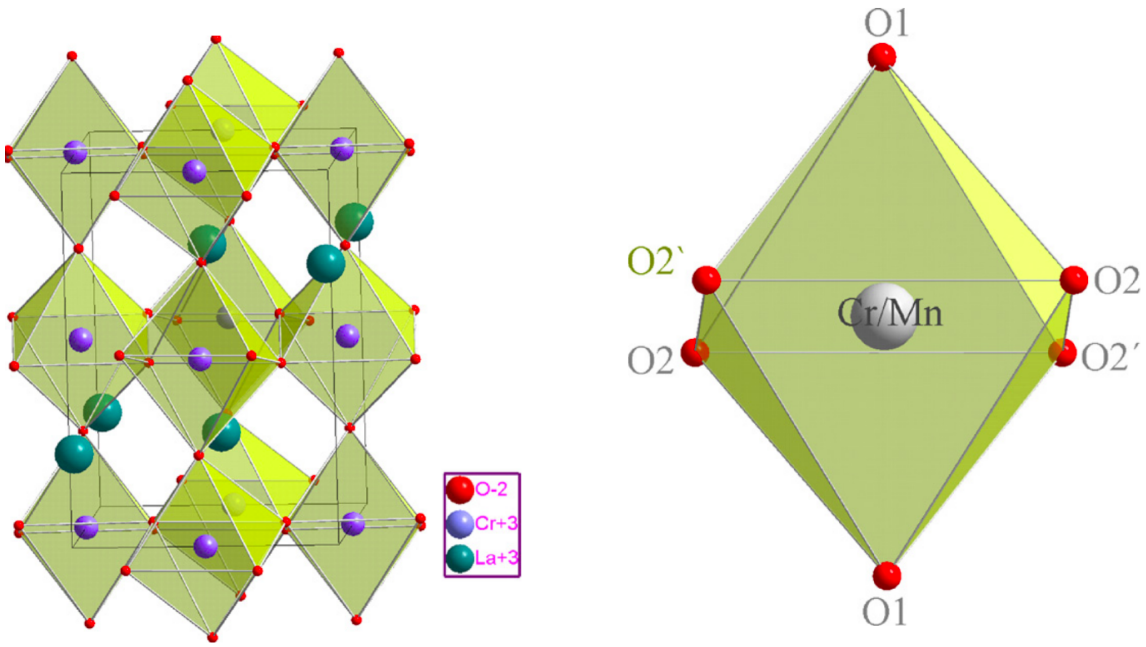

(a) (b)

Figure 2.1: (a) Unit cell of $LaCrO_3$ at 295 K and (b) octahedral coordination in $LaCrO_3$ [13]. The powder samples used were prepared by the standard solid-state reaction method, and were thus made of polycrystals.

Table 2.1: Cell parameters of the $LaCrO_3$ unit cell at room temperature. The powder samples used were prepared by the standard solid-state reaction method, and were thus made of polycrystals.

	Orthorhombic [1, 13, 14, 19]	Rhombohedral [13, 14]
a [Å]	5.52	5.53
b [Å]	5.49	5.53
c [Å]	7.76	13.35

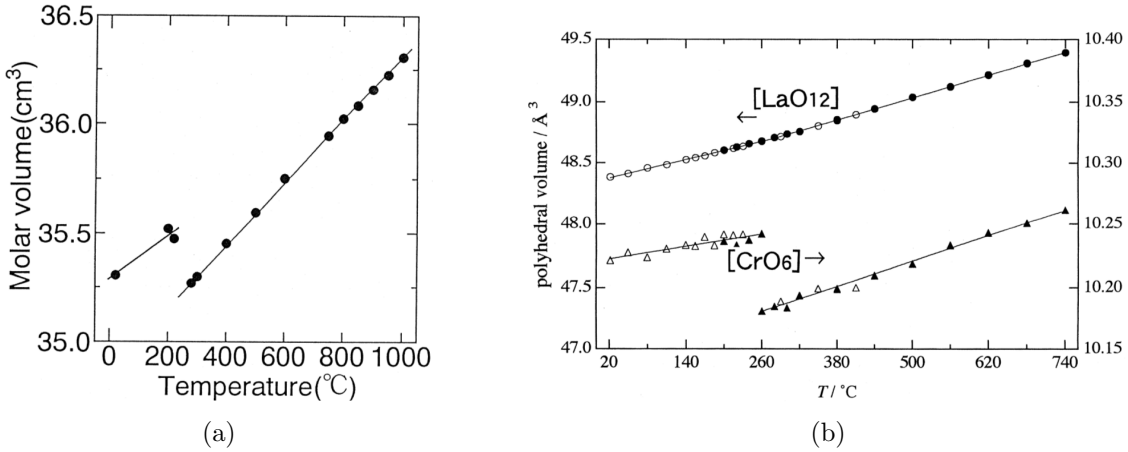

(a) (b)

Figure 2.2: (a) Evolution of the molar volume of $LaCrO_3$ with temperature and (b) dependence of the volume of the $[LaO_{12}]$ polyhedra and $[CrO_6]$ octahedra on temperature [14]. The powder samples used were prepared by the standard solid-state reaction method, and were thus made of polycrystals.

2.1.2 Electronic properties

$LaCrO_3$ is an insulator with a large electronic band gap of about 2.8 eV according to ultraviolet photoemission and Bremsstrahlung isochromat spectroscopic measurements [18]. This band gap has been computationally confirmed by Sushko *et al.* [20]. It is due to intra Cr $d-d$ transitions, while the O $2p$ − Cr $3d$ transitions happen for an energy of about 5 eV [20].

2.1.3 Magnetic properties

$LaCrO_3$ has an antiferromagnetic ordering [13, 20]. The magnetic properties are mainly due to the Cr^{3+} ions, which couple with their oxygen nearest neighbours (see Fig. 2.1) in order to arrange in a G-type configuration [13, 20] (both intra-plane and inter-plane couplings are antiferromagnetic, see Fig. 2.3).

The evolution of the magnetization of $LaCrO_3$ with temperature under a weak applied magnetic field ($H = 200$ Oe) is represented in Fig. 2.4(a). In order to obtain these curves, a sample is first cooled to 5 K without any applied magnetic field. The temperature is then increased with a fixed magnetic field (ZFC for zero field cooling). Once the maximal temperature is reached, the sample is again cooled but this time the magnetic field is still applied (FC for field cooling). There is a clear transition at the temperature where the ZFC and FC curves meet. This temperature (called the Néel temperature T_N) is approximately 293 K [19]. Under T_N, the material is antiferromagnetic, and above T_N, the material is paramagnetic. At $T = 5$ K, Fig. 2.4(b) shows that the response of the material to an applied magnetic field is linear. This is a characteristic of a pure antiferromagnetic phase. There is a small deviation to the linear law due to the alignment of the weak excess magnetization (this phenomenon also leads to the difference between ZFC and FC curves).

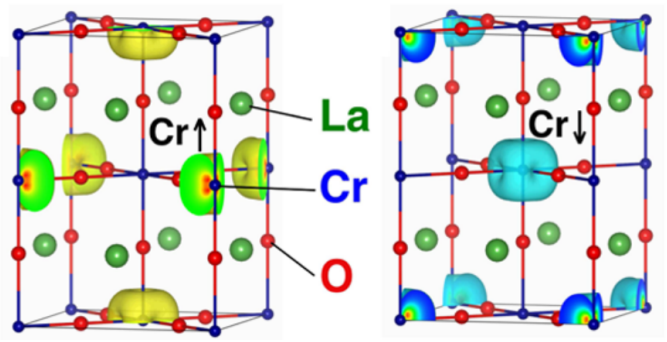

Figure 2.3: Magnetic ordering of $LaCrO_3$ at 1.5 K [20].

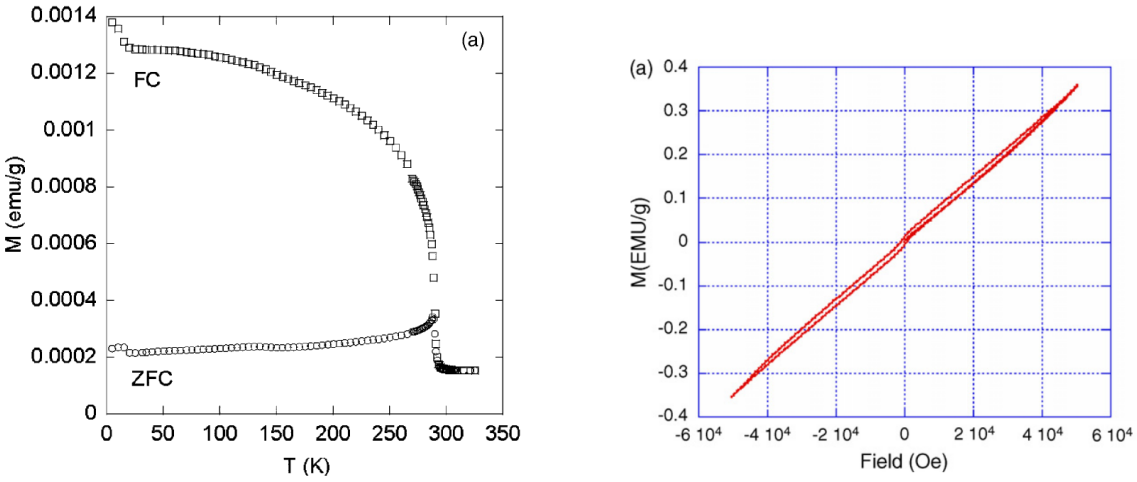

(a) (b)

Figure 2.4: (a) Magnetization of $LaCrO_3$ as a function of temperature under an applied magnetic field of 200 Oe and (b) hysteresis curve of $LaCrO_3$ at T = 5 K [13]. The powder samples used were prepared by the standard solid-state reaction method, and were thus made of polycrystals.

The magnetic moment at chromium sites has been measured by Maiti *et al.* [18] and is of 3.85 μ_B, which is close to the theoretical value of 3.87 μ_B [18].

2.1.4 Optical properties

The band gap of 2.8 eV indicates that the absorption of light starts for photons of a wavelength around 440 nm. The photons with a greater wavelength are not absorbed by $LaCrO_3$, which gives it a green color [18, 20]. The transmittance of $LaCrO_3$ can be seen in Fig. 2.11(a) and the absorption coefficient spectrum is depicted in Fig. 2.11(b). The discussion about these graphs will be done at the same time as for the case of $La_{1-x}Sr_xCrO_3$. The measured density of states (by X-ray photoemission and absorption spectroscopies) is also represented in Fig. 2.11(c). The samples used to create Fig. 2.11 were thin epitaxial films grown on (001)-oriented $SrTiO_3$ substrate by molecular beam epitaxy (MBE). They were thus very pure monocrystals. These figures show that there are no excitonic effects in $LaCrO_3$, because there is no peak of absorption before 2.8 eV.

2.2 Strontium chromate $SrCrO_3$

Now that the measured properties of $LaCrO_3$ have been described, $SrCrO_3$ can be characterized. This material has not been extensively described in the literature. The same subsections are

nevertheless used as in the case of $LaCrO_3$.

2.2.1 Crystalline configuration

Strontium chromate $SrCrO_3$ is a perovskite material which has a cubic structure with a lattice parameter of 3.82 Å at room temperature [21, 22]. This has been measured both on powder samples prepared by a solid-state reaction and on epitaxial films grown by MBE. The space group of $SrCrO_3$ is $Pm3m$ (No. 221) [15, 16, 17]. The unit cell (at room temperature) of $SrCrO_3$ is represented in Fig. 2.5.

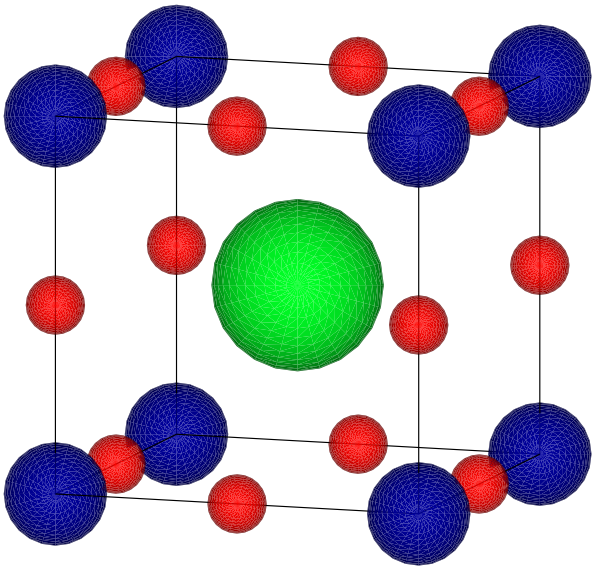

Figure 2.5: Unit cell of $SrCrO_3$ at room temperature. Inspired from Ref. [23]. Green : Sr, blue : Cr, red : O.

2.2.2 Electronic properties

Fig. 2.6 shows the evolution of the resistivity of $SrCrO_3$ with temperature. For $T > 50$ K, the temperature coefficient $\frac{d\rho}{dT}$ is positive. The room temperature resistivity is $1.3 \cdot 10^{-3}$ Ω cm, and it lowers to $5.2 \cdot 10^{-4}$ Ω cm at 50 K [21]. This indicates a metallic behavior with strong electron-electron scattering [21]. Previously, an insulator like behavior was observed in polycrystalline powders. This difference may be due to scattering at grain boundaries. The upturn of the resistivity at $T \sim 50$ K is usually observed for metallic transition metal oxides or for polar/unpolar perovskite heterojunctions [21]. It is thought that this upturn is due to weak localization. A simple description of this phenomenon can be found in Appendix B.

2.2.3 Magnetic properties

The magnetic susceptibility of $SrCrO_3$ is represented in Fig. 2.7. The dependence on temperature is strong below 100 K. The curve in the inset of this figure shows that the behaviour of $SrCrO_3$ cannot be described by Curie-Weiss law, where the inverse susceptibility is linear with respect to the temperature. In fact, this behavior is typical of an antiferromagnetic material. It is indeed the observed magnetic ordering (C-type, which means that the intra-plane coupling is antiferromagnetic and the inter-plane coupling is ferromagnetic) ground-state of $SrCrO_3$ [21]. Pure $SrCrO_3$ is thus a metallic yet antiferromagnetic compound.

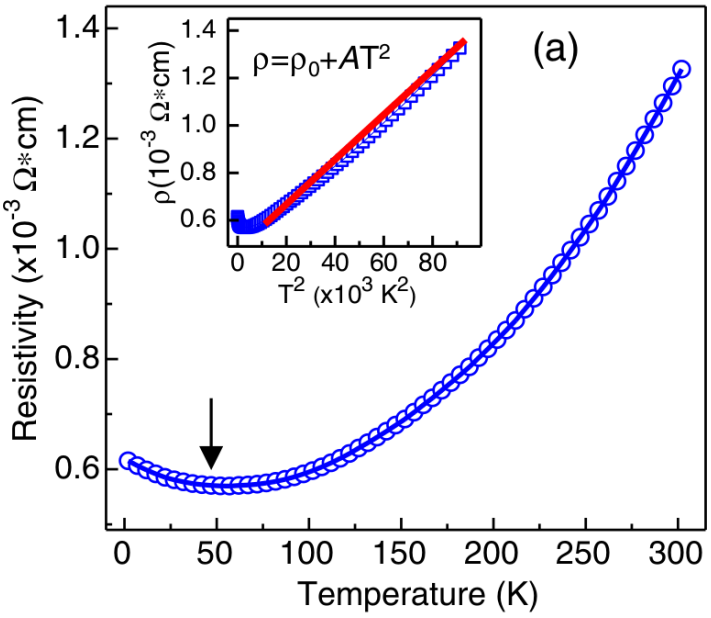

Figure 2.6: Evolution of the resistivity of $SrCrO_3$ with temperature [21]. The samples used were epitaxial films grown by MBE.

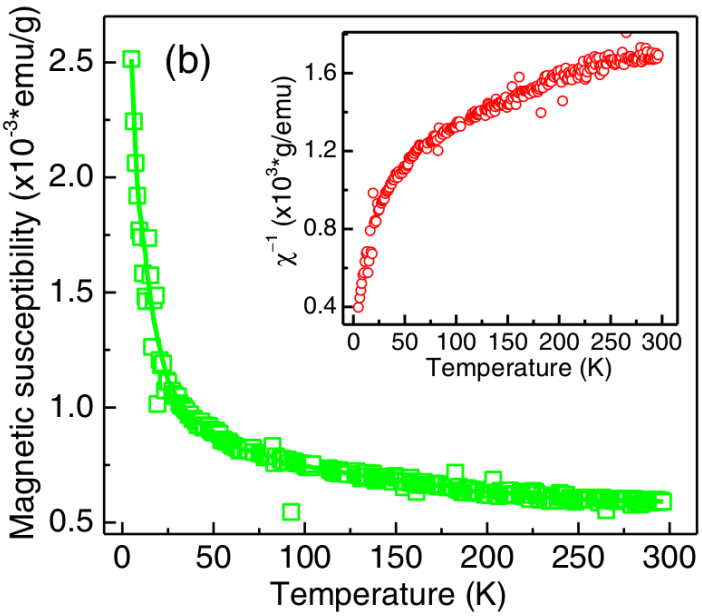

Figure 2.7: Evolution of the magnetic susceptibility of $SrCrO_3$ with temperature [21]. The samples used were epitaxial films grown by MBE.

2.2.4 Optical properties

$SrCrO_3$ is a metal and is therefore not transparent. Only a few papers have been published about $SrCrO_3$, and not a lot of data are available.

2.3 Strontium doped lanthanum chromate $La_{1-x}Sr_xCrO_3$

Now that the boundary materials ($x = 0$ and $x = 1$) of $La_{1-x}Sr_xCrO_3$ have been described, the properties of the materials with intermediate values of x can be detailed.

2.3.1 Crystalline configuration

As mentioned previously, the space group of $LaCrO_3$ is *Pbnm* while the one of $SrCrO_3$ is $Pm3m$ at room temperature. The unit cell volume for different values of x in epitaxial $La_{1-x}Sr_xCrO_3$ has been measured by Zhang *et al.* The results are represented in Fig. 2.8 (red squares) where the blue and green lines represent the expected behavior (by assuming a linear evolution between the two boundary values) for two limiting cases : the green one stands for the case of a bulk material, while the blue one supposes strained films and uses the Poisson ratios of $LaCrO_3$ and $SrCrO_3$. It appears that a partial relaxation takes place in $La_{1-x}Sr_xCrO_3$, except for $x = 0.5$ which is fully relaxed.

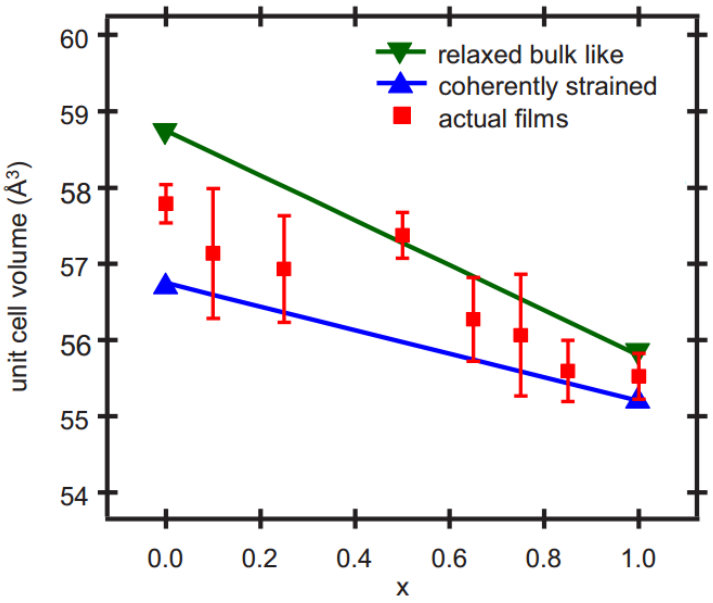

Figure 2.8: Unit cell volumes of $La_{1-x}Sr_xCrO_3$ [2]. The green and blue lines represent two limiting cases (the bulk volume, totally relaxed, and the volume of fully strained films). The films used were grown by MBE.

2.3.2 Electronic properties

A metal-insulator transition is usually observed for transition-metal oxide systems [18]. This transition can happen by changing the oxygen stoichiometry or the structure of the material in a fixed environment (pressure and temperature). In particular, $3d$ transition-metal perovskite oxides of the form ABO_3 ($LaTiO_3$, $LaCoO_3$,...) are insulators which can be converted into conducting materials by doping. $La_{1-x}Sr_xCrO_3$ is an exception to this trend : this material does not undergo an insulator to metal transition at low temperature (even when the maximal doping is achieved) and remains insulating [18]. However, at higher temperature, an insulator to metal

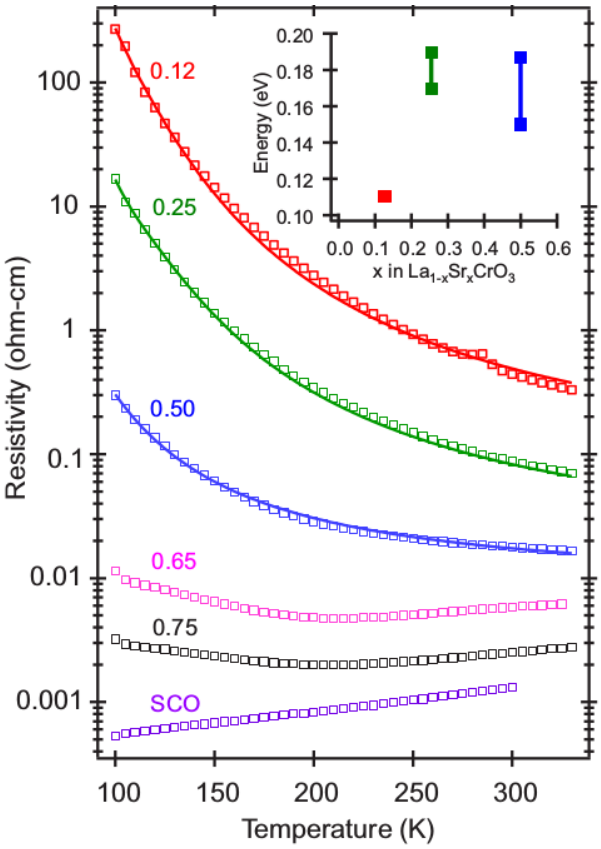

Figure 2.9: Temperature dependence of the electrical resistivity of epitaxial $La_{1-x}Sr_xCrO_3$ films [2].

transition is well observed for $x \geq 0.65$ [2]. This phenomenon is represented in Fig. 2.9. The curves for $x \leq 0.50$ are characteristic of insulating or semiconducting material : $\frac{d\rho}{dT} < 0$ for all T, while it is not the case for higher Sr concentrations. This insulator to metal transition is observed when the $La_{1-x}Sr_xCrO_3$ films are grown on a substrate on which they are in compressive in-plane strain for all x. When they are grown on another substrate on which they are in tension, no insulator to metal transition is observed [2].

Increasing the Sr doping effectively increases the concentration of holes in the material and therefore the conductivity. It is important to measure the conductivity of $La_{1-x}Sr_xCrO_3$ on high purity samples, because grain boundaries in polycrystalline samples have a great effect on charge carriers transport in this material [2], as it has been mentioned for $SrCrO_3$. Fig. 2.10 represents the conductivity of a few $La_{1-x}Sr_xCrO_3$ films. Comparing Figs. 2.9 and 2.10 leads to two different models for the charge transport in the films. The measure of the resistivity shows that the band conduction model can be used :

$$\rho \propto \exp\left(\frac{E_g}{kT}\right) \tag{2.1}$$

where E_g is the activation energy for this phenomenon (the band gap energy) and k is the Boltzmann constant. The measure of the conductivity also shows that the small-polaron hopping model can be used between 100 and 300 K :

$$\rho \propto T \exp\left(\frac{E_a}{kT}\right) \tag{2.2}$$

where E_a is the activation energy for the hopping. This apparent contradiction simply indicates that the transport in $La_{1-x}Sr_xCrO_3$ is best described using a hybrid model. Zhang *et*

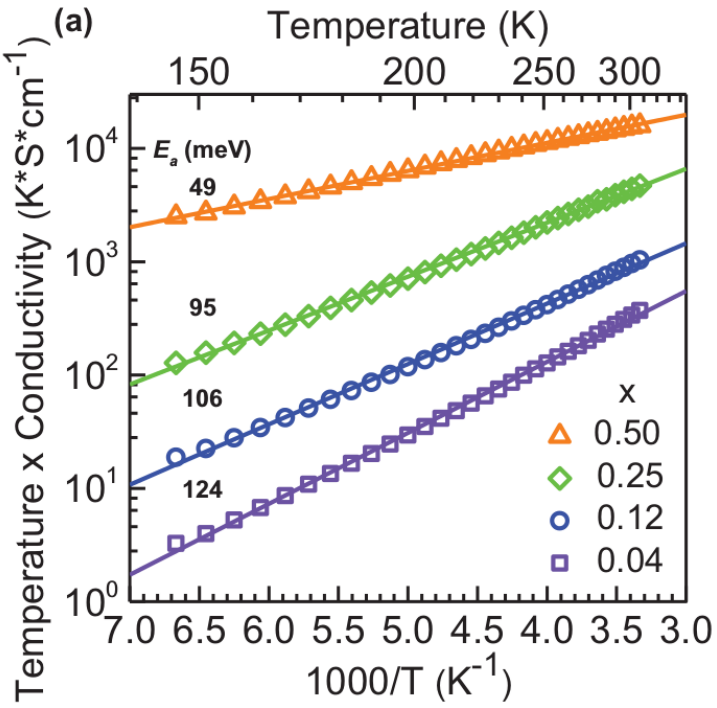

Figure 2.10: Temperature dependence of the electrical conductivity of epitaxial $La_{1-x}Sr_xCrO_3$ films [1].

al. suggested that polaron hopping is frozen out below a given temperature T_0. This gives the resistivity

$$\rho(T) = \rho_0 \exp\left(\frac{E_a}{kT}\right) + \frac{CT \exp\left(\frac{E_a}{kT}\right)}{1 + \exp\left(\frac{T_0 - T}{\Delta T}\right)} \tag{2.3}$$

where ΔT is the temperature range over which the freezing occurs. The resistivity in Fig. 2.9 has been interpolated using this equation.

Room-temperature conductivity for $La_{1-x}Sr_xCrO_3$ is given in Table 2.2. This table also gives the values of the mobility and hole concentration, which have been obtained from the values of the conductivity and assuming a small-polaron hopping model. This shows that even if the mobility is really small, the high values of the hole concentration lead to high conductivities.

Table 2.2: Room-temperature conductivity σ, mobility μ and hole concentration p of epitaxial $La_{1-x}Sr_xCrO_3$ films [1].

x	σ [S cm^{-1}]	μ [cm^{2}V^{-1}s^{-1}]	p [$\times 10^{20}$ cm^{-3}]
0	×	×	×
0.04	1.2	0.0095	7.9
0.12	3.6	0.018	12
0.25	15	0.027	34
0.50	54	0.04	75

2.3.3 Magnetic properties

Doping $LaCrO_3$ results in lowering the Néel temperature to 200 K for $x = 0.50$ [19]. Nevertheless, the material remains antiferromagnetic for all values of x [18] at low temperature. The magnetic

moment at Cr sites decreases when the fraction of Sr increases. Table 2.3 gives the magnetic moment at this site for different x.

Table 2.3: Magnetic moment at the Cr site of $La_{1-x}Sr_xCrO_3$ [18].

x	Magnetic moment [μ_B]
0.0	3.85
0.1	2.41
0.2	2.11
0.3	1.93
0.5	2.36

2.3.4 Optical properties

The transmittance values of a few $La_{1-x}Sr_xCrO_3$ films are given in Table 2.4 and Fig. 2.11(a) represents the evolution of this transmittance with the wavelength of the incident light. In Table 2.4, the values of the transmittance have been obtained by averaging the values for different wavelengths. They also include the contribution of the substrate on which the films have been grown ($SrTiO_3$). The thicknesses of the different films are different, and these differences have to be taken into account for a quantitative analysis.

The absorption coefficient of these films as a function of the energy of the incoming light is depicted in Fig. 2.11(b). Figs. 2.11(a) and 2.11(b) show that the absorption increases when the Sr doping increases. Fig. 2.11(c) represents the measured density of states for the same $La_{1-x}Sr_xCrO_3$ films. In the case of LCO, Zhang *et al.* analysed these results as the transition of electrons from the Cr 3*d* t_{2g} orbitals[1] to the Cr 3*d* e_g ones (at $\sim$ 2.7 eV, see transition A in Fig. 2.11(b)). In the case of $La_{1-x}Sr_xCrO_3$, the Cr 3*d* t_{2g} orbitals split in two and the transition occurs between these two parts at $\sim$ 0.8 eV (see transition B in Fig. 2.11(b)). Fig. 2.11(d) summarizes these explanations in a schematic way.

Table 2.4: Transmittance T and thickness d of $La_{1-x}Sr_xCrO_3$ films [1].

x	T [%]	d [nm]
0	69.1	100
0.04	66.9	100
0.12	63.4	67
0.25	54.2	80
0.5	42.3	50

[1]Due to a crystal field splitting, the Cr 3*d* orbitals are separated in two groups : three t_{2g} ones and two e_g ones. This will be detailed in Chapter 5.

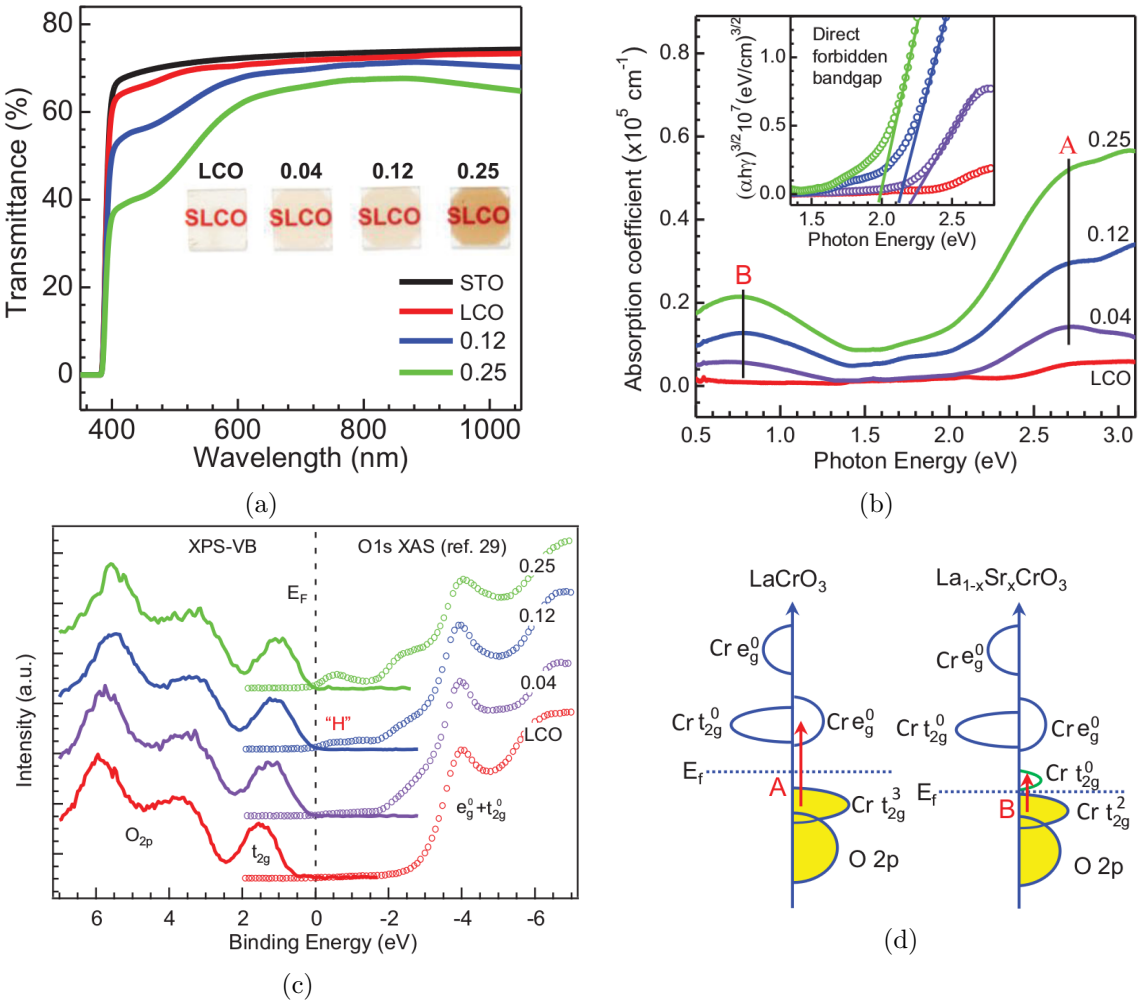

Figure 2.11: (a) Transmittance of $La_{1-x}Sr_xCrO_3$ films. STO ($SrTiO_3$) is the substrate on which the films are grown. The transmittance is represented for $x = 0.04$, $x = 0.12$ and $x = 0.25$. (b) Optical absorption spectra for the same $La_{1-x}Sr_xCrO_3$ films. (c) Measured density of states of $La_{1-x}Sr_xCrO_3$ films. XPS = X-ray photoemission spectroscopy, XAS = X-ray absorption spectroscopy. (d) Schematic representation of the A and B transitions of (b). From Ref. [1].

Chapter 3

Small-polaron hopping

Contents

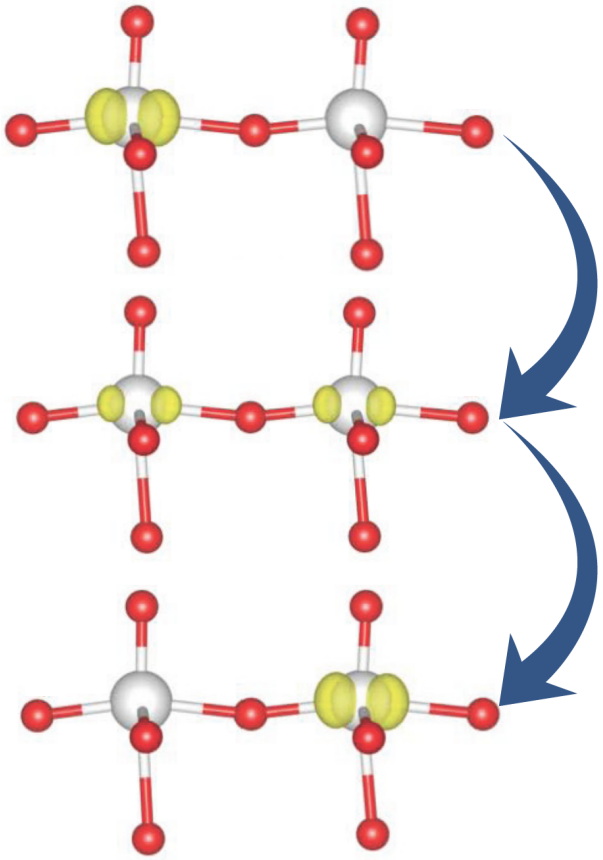

The conducting electrons of a material interact with the ions of the lattice which are vibrating around their equilibrium position. If this interaction is strong enough, an electron (or a hole) can induce a large deformation of the lattice around itself, which traps the carrier and creates a quasiparticle called a polaron (see Fig. 3.1). This phenomenon has been observed in many semiconductors and polymers [24].

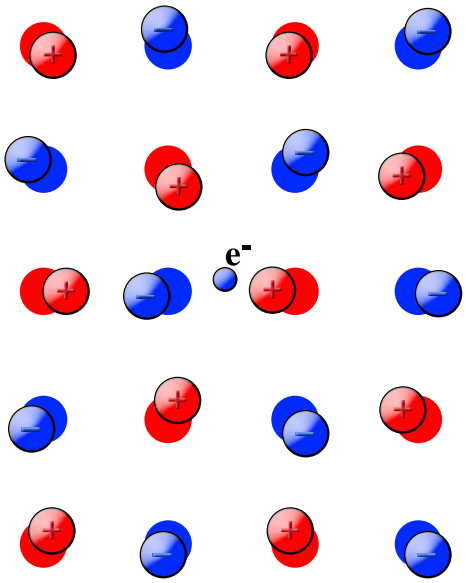

Figure 3.1: Artistic view of a polaron [25]. The conduction electron deforms the lattice which in return screens the electron.

When the characteristic frequencies of the phonons in a material are low, the displacement of the ions creates a potential well around the carrier. There are two families of polarons : large and small ones. Large polarons spread over many lattice sites, and the material can be considered as a continuous polarizable medium. When their kinetic energy is low, they propagate through the medium like free carriers with a larger effective mass [24]. Small polarons are localized on one lattice site. In this case, the discreteness of the lattice is important and the interactions between the carrier and the vibrations of the ions are more important : it is the strong-coupling regime. Only small polarons will be considered here, because the experimental results for $La_{1-x}Sr_xCrO_3$ correspond to small-polaron hopping and not to large polarons [1, 2].

If the temperature is large enough, the carrier trapped in a polaron can hop from one lattice site to another in the presence of electron-phonon interactions : the transport is thermally activated. The deformation at the first site completely disappears and is transferred to the other site [26].

First, a phenomenological theory is introduced : Marcus model for the transport of small polarons. The more formal theory of small-polaron transport of Holstein is then presented. It leads to an expression of the mobility of the polaron which can be used to model the conductivity of the material. Finally, the optical properties are described, and the optical conductivity is given.

3.1 Marcus theory of transport mechanism

Marcus theory is phenomenological and helps to understand what happens in a small-polaron system. It is almost equivalent to the Holstein theory [27]. The description of this model is

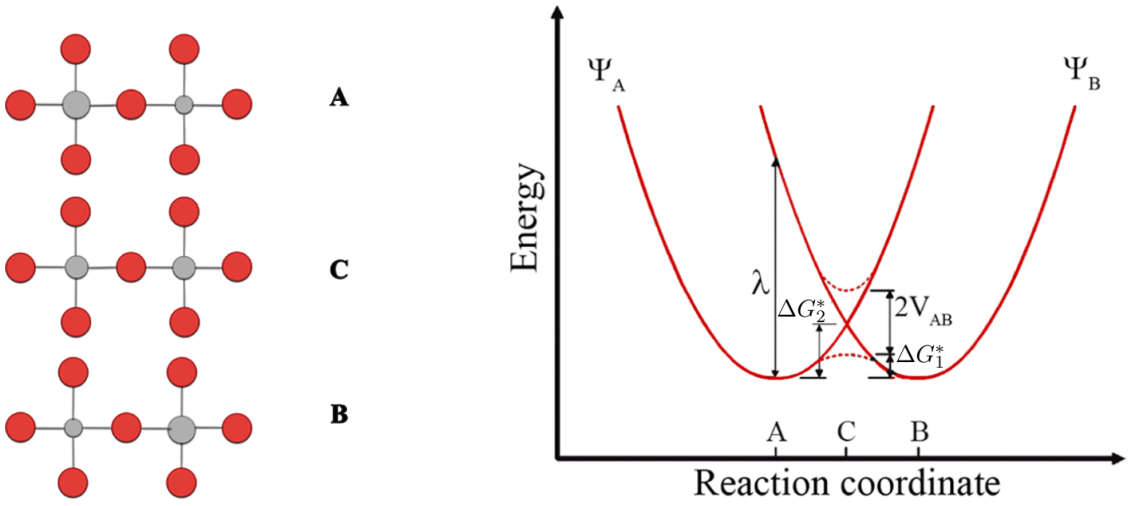

(a) (b)

Figure 3.2: (a) Schematic representation of the charge carrier transfer between two ions. At the top (A), the charge carrier is localized on the grey ion on the left. At the bottom (B), the carrier is localized on the ion next to the first one. At the transition state (C), the carrier is shared between the two ions. (b) Energy representation of the situation in (a) according to Marcus theory. Ψ_A and Ψ_B are the states of the two situations A and B in (a). Adapted from Ref. [28].

based on Refs. [27, 28].

The charge carrier transfer is schematically represented in Fig. 3.2(a). In configuration A, the charge carrier is localized on the grey ion on the left. In configuration B, the carrier is localized on the ion right next to the first one. The transition state C corresponds to a situation where the carrier is spread over both ions. Fig. 3.2(b) represents the energy profiles for this process in an ideal case. Ψ_A and Ψ_B are the states corresponding to the two localized states.

A few parameters are introduced in Fig. 3.2(b). λ is the reorganization energy which corresponds to the energy of the final state Ψ_B at the configuration A. V_{AB} is the carrier coupling, equal to the carrier transfer integral J in Holstein theory [27] (see next section). When the carrier coupling is strong, V_{AB} is large and the energy barrier is decreased by this quantity. In this case, the main transfer mechanism is the thermal hopping. On the other hand, if the coupling is small, the main mechanism for the transfer of the polaron is the tunnelling of the carrier through the barrier. In the first case, ΔG_1^* is the activation barrier while it is given by ΔG_2^* in the second case (noted E_a in Holstein theory).

Following Marcus model, the transmission coefficient, i.e. the probability for a carrier to transfer from one site to another, is

$$\kappa = \frac{2P_{12}^0}{1 + P_{12}^0} \tag{3.1}$$

where P_{12}^0 is the probability of conversion to the final state per passage through the intersection (at configuration C). It is given by [27]

$$P_{12}^0 = 1 - \exp\left(-\frac{V_{AB}^2}{h\nu_0}\sqrt{\frac{\pi^3}{\lambda kT}}\right) \tag{3.2}$$

where ν_0 is the frequency of longitudinal phonons. When κ is close to 1, the transfer is mainly due to thermal hopping.

3.2 Holstein theory of transport mechanism

In polaronic materials, the mobility of charge carriers is so low that the transport theory usually based on Boltzmann equation is not valid [29]. Indeed, this theory relies on the hypothesis that the interactions between the carriers and the phonons are not too strong. It is however not the case in systems with small polarons. In these cases, it has been observed that the carrier mobility is thermally activated at high temperature : there is a phonon activated hopping mechanism [29]. In other words, if the temperature is large enough, the carrier trapped in a polaron can hop from one lattice site to another in the presence of electron-phonon interactions. The deformation at the first site completely disappears and is transferred to the other site [26].

It can be shown that the effective mass of a small polaron can be quite large, and the width of the allowed band for this state ΔE_p can be pretty small [29] :

$$\Delta E_p \propto \exp\left(-\gamma \coth\left(\frac{\hbar\omega_0}{2kT}\right)\right) \tag{3.3}$$

where γ is a coupling constant greater than 10 and ω_0 is the limiting frequency of longitudinal phonons. When the temperature increases, the bandwidth decreases, and at some point it can be considered as a state of a small polaron localized at a lattice site [29]. The hopping from site to site is then due to a transport mechanism through an energy barrier, or by a tunnelling.

At high temperature ($kT > \frac{\hbar\omega_0}{2}$), it can be shown that the probability $W(T)$ for the hopping of a carrier from one lattice site to the neighbouring one is [29]

$$W(T) = \frac{\omega_0}{2\pi} f(\eta_2) \exp\left(-\frac{E_a}{kT}\right) \tag{3.4}$$

where E_a is the activation energy given by

$$E_a \simeq \frac{\gamma}{2}\hbar\omega_0 \tag{3.5}$$

and $f(\eta_2)$ is a dimensionless function of $\eta_2 = \frac{J^2}{\hbar\omega_0\sqrt{E_a kT}}$ (J is an overlap integral characterizing the width ΔE of the original electron band) which does not exceed unity. These expressions are valid for a small J. The diffusion coefficient D is then, following a random walk approach for the motion of the polarons (where individual hops are uncorrelated) [29],

$$D = \frac{a^2}{2} W(T) \tag{3.6}$$

where a is the distance between two lattice sites for the localization. Einstein relation then leads to the hopping mobility μ_h :

$$\mu_h = \frac{eD}{kT} = \frac{ea^2}{2\hbar}\frac{1}{2\pi}\frac{\hbar\omega_0}{kT} f(\eta_2) \exp\left(-\frac{E_a}{kT}\right). \tag{3.7}$$

In this case, the resistivity of the material is thus given by [30]

$$\rho(T) = \rho_0 T \exp\left(\frac{E_a}{kT}\right). \tag{3.8}$$

At low temperature, it has been suggested that the usual Boltzmann transport takes place, but in the narrow polaron band [29]. In this case, the mobility is

$$\mu_B = \frac{ea^2}{\hbar}\frac{\hbar\Delta\omega}{kT}\gamma^{-2}\sinh^2\left(\frac{\hbar\omega_0}{2kT}\right) \tag{3.9}$$

where $\Delta\omega$ is the width of the dispersion band for longitudinal phonons.

A more detailed theory also takes into account the tunnelling of electrons. When the energy barrier is small enough, the mechanism is thermally activated, but when the energy barrier is too large, carriers tunnel through it from one lattice site to the next one.

3.3 Optical properties

In a usual insulator, it has been explained in Chapter 1 that absorption of light begins above the optical band gap value, and light is reflected under the plasma frequency. This picture has to be modified when the material is polaronic.

Fig. 3.3 represents what happens when a small-polaron system absorbs light according to Holstein model (equivalent to Marcus model in this case). The carrier is initially in its ground state at $q = -1$ (corresponding to the reaction coordinate A in Fig. 3.2(b)). This ground state is actually broadened by phonon fluctuations which lead to an energy variance Δ [30]. If the electron half-bandwidth $\frac{\Delta E}{2}$ is much smaller than Δ, the excitation of the small polaron is possible if the energy of the absorbed photon is close to the double[1] of the polaron binding energy E_p defined in Fig. 3.3. Once excited, the polaron may relax to the ground state corresponding to its initial configuration or to the ground state corresponding to the neighbouring lattice site [30].

In the case of thermal hopping, and when $\frac{\Delta E}{2} \ll \Delta$, the optical conductivity (which reflects the absorption of the material : it is the conductivity due to carriers excited by the absorption of light) is given by [30]

$$\sigma(\omega, T) = \sigma(0, T) \frac{\sinh\left(2\hbar^2\omega_{\max}\omega/\Delta^2\right)}{2\hbar^2\omega_{\max}\omega/\Delta^2} \exp\left(-\frac{(\hbar\omega)^2}{\Delta^2}\right). \tag{3.10}$$

The optical conductivity shows a peak at $\omega_{\max} = \frac{2E_p}{\hbar}$ and looks like a slightly distorted gaussian curve. If the condition $\frac{\Delta E}{2} \ll \Delta$ is not fulfilled, then the position of the maximum in the optical conductivity is lowered [30] : $\hbar\omega_{\max} = 2E_p - \frac{(\Delta E)^2}{8E_p}$ and Eq. (3.10) is not valid anymore.

Moreover, under the hypothesis that $\frac{\Delta E}{2} \ll \Delta$, the phonon fluctuation of the ground state is given by [30]

$$\Delta^2 = \begin{cases} 8E_p\frac{\hbar\omega_0}{2} & \text{if } \hbar\omega_0 \gg kT \\ 8E_pkT & \text{if } \hbar\omega_0 \ll kT. \end{cases} \tag{3.11}$$

The fit of the optical conductivity curve leads to the determination of Δ and thus of the polaron binding energy as well.

The optical conductivity of the small-polaron system $Pr_{1-x}Ca_xMnO_3$ (PCMO) has been measured by Mildner *et al.* and is given in Fig. 3.4 as an example. It shows that in this system, the first two peaks in the optical conductivity can be modelled by the small-polaron theory and fitted by Eq. (3.10). The other two peaks do not correspond to small-polaron transitions (they happen at too high photon energies) and should be subtracted from the absorption spectra of Fig 3.4 in order to completely analyse the data. In is interesting to note that in Fig. 2.11(b), a first peak is also observed in the case of $La_{1-x}Sr_xCrO_3$. Together with the electrical resistivity developed at Section 2.3.2, it indicates that $La_{1-x}Sr_xCrO_3$ indeed contains small polarons.

[1]The factor 2 has been determined by Dynamical Mean-Field Theory [30].

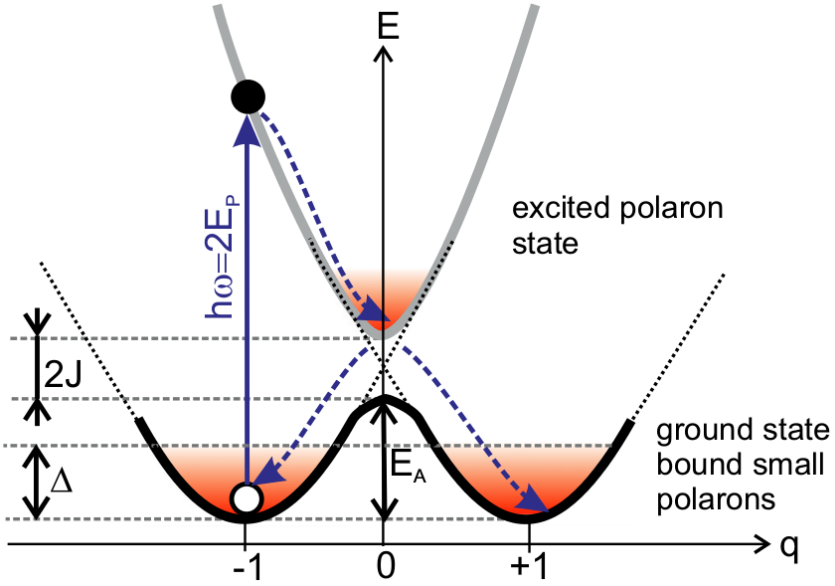

Figure 3.3: Schematic representation of a small-polaron excitation in the two-site model [30].

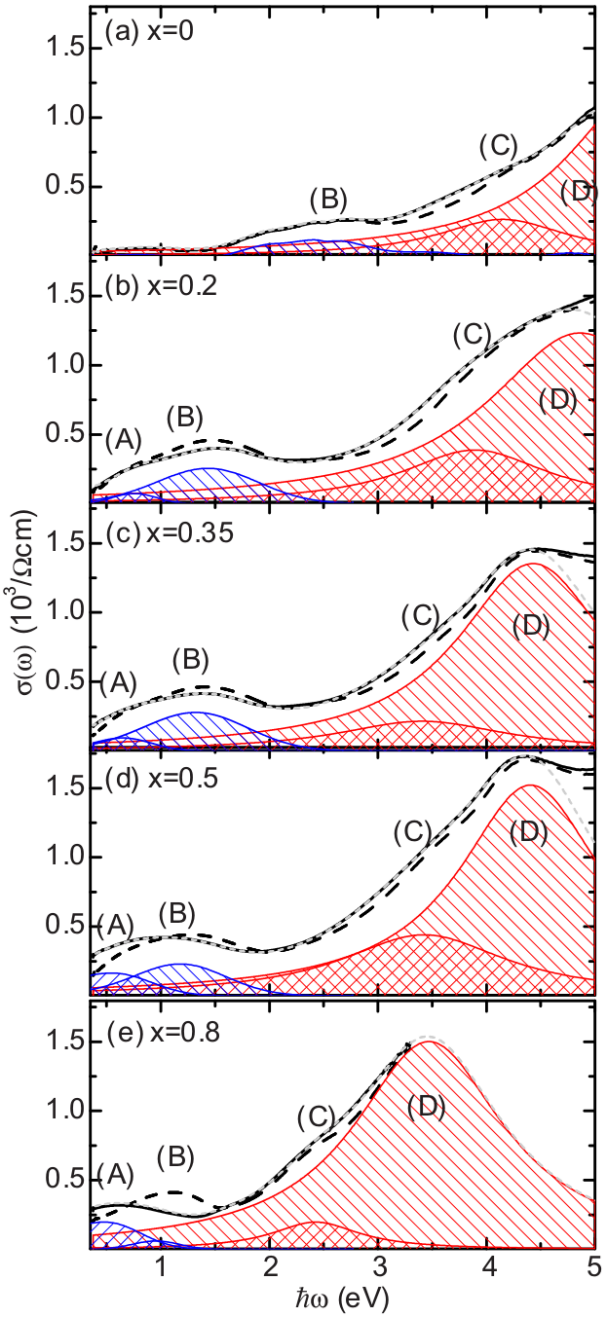

Figure 3.4: Optical conductivity of $Pr_{1-x}Ca_xMnO_3$ films for various x. The solid black lines correspond to the measure at 300 K, while the dashed black lines correspond to the measure at 80 K. The blue hatched curves are fit results from the application of Eq. (3.10) for peaks (A) and (B), and the red hatched curves are fit results by Lorentzian functions for peaks (C) and (D). The sums of the fit are represented by the light-gray dashed lines. From Ref. [30].

Chapter 4

Hubbard model in Density Functional Theory

Contents

The present chapter describes the Hubbard model for insulators and explains why a U term is important in the case of $La_{1-x}Sr_xCrO_3$. A description of the Density Functional Theory (DFT) is given in Appendix C. Usually, the standard Local Density Approximation (LDA) or Generalized Gradient Approximation (GGA) work well. They tend to delocalize the electrons over the whole crystal, considering that they feel a mean-field Coulomb potential. However, the interactions between the electrons in some crystals containing rare-earth elements or transition metals are too important to be represented by usual DFT [31]. Indeed, in these materials, electrons in partially filled d or f orbitals are localized around the atoms and they undergo much larger Coulomb repulsion. The delocalization of LDA or GGA is not efficient to model their behavior. In order to correctly predict properties of these materials, a localized term U called the Hubbard term is added to the density functional [31, 32]. This is the DFT+U. Unless said explicitly, the main sources for this small chapter are Refs. [32, 33, 34, 35], which provide complete reviews of the technique and of the Hubbard model. The principles of the method are first presented. A brief discussion about the determination of the value of U is then given.

4.1 Review of the method

Usual LDA and GGA lead to an excessive delocalization of electrons. The electron-electron interaction energy E_{ee} is the sum of the Hartree energy E_H and the exchange-correlation energy E_{xc}. E_H contains an electron self-interaction term that needs to be cancelled out by the exchange-correlation energy. The problem of the usual approximations is actually that the self-interaction is not completely cancelled. It can be seen as if fragments of a given electron were to repel each other (through the density associated with each fragment), which leads to the excessive delocalization of the wave functions.

This lack of cancellation of the electronic self-Coulomb interaction is not the only problem coming from the approximate functionals. Indeed, it reflects only the single-electron interaction. However, a correct treatment of the correlation term should take precisely into account the many-body terms of the electronic energy. In order to do so, new methods have been developed recently (Dynamical Mean-Field Theory DMFT, Reduced Density Matrix Functional Theory RDMFT), leading to better results for correlated materials. The drawback of these methods is that they are much more computationally expensive than usual DFT calculations. Moreover, these techniques are difficult to implement in already existing DFT codes. This is why DFT+U has been developed : it is one of the simplest theory and leads to quite good results for correlated materials. Moreover, the computation time does not vary too much compared to usual DFT : in DFT+U, only the localized electronic states of a system are described using the Hubbard model. Other valence electrons are treated within classic DFT.

4.1.1 Hubbard model

Hubbard model is a simplified model that has been derived to describe strongly interacting electrons in a solid. It takes into account the motion of electrons in a solid and the non-linear repulsive interaction between them, but in a too simple way to be completely exact. It is nevertheless able to predict many properties of various solids : metal-insulator transition, superconductivity, (anti)ferromagnetism, ferrimagnetism,...

The most simplified Hubbard model considers a crystal lattice Λ constituted of atomic sites numbered by the index I, K,... The main assumption of this oversimplified model is that each atom has only one non-degenerate electronic orbital. The idea behind this hypothesis is that in a real crystal, the electrons in other states do not have a great influence on this state. The philosophy of this approach is illustrated in Fig. 4.1. It is actually very similar to the tight-binding approach on which the previous assumption is added. In this model, localized electrons (dark grey orbitals in Fig. 4.1) can tunnel from one atom to another with a non-negligible probability.

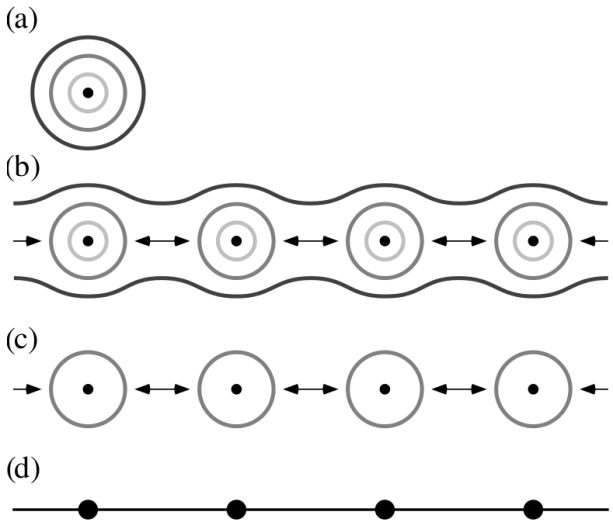

Figure 4.1: Schematic representation of the simplest Hubbard description [35]. (a) A single atom with multiple electrons in different orbitals. (b) In a solid, electrons of the outer orbital (black) become itinerant, while the other ones (grey) stay localized on their original atomic site. The electrons in the grey orbitals mostly stay on their atomic site, but they can tunnel from one grey orbital to another with a non-negligible probability. (c) Only the electrons in the dark grey orbitals are considered in this model. (d) If these orbitals are non-degenerate, (c) is equivalent to a lattice model where electrons are localized on lattice sites and hop from one site to another.

The Hamiltonian H of the Hubbard model is

$$H = H_{\text{hop}} + H_{\text{int}} \tag{4.1}$$

where the first term refers to the hopping mechanism and the second term stands for the interaction between electrons on the same lattice site. They are given by

$$H_{\text{hop}} = \sum_{I,K\in\Lambda} \sum_{\sigma=\uparrow,\downarrow} t^{IK} c^{\dagger,I\sigma} c^{K\sigma} \tag{4.2}$$

$$H_{\text{int}} = \sum_{I\in\Lambda} U^I N^{I\uparrow} N^{I\downarrow} \tag{4.3}$$

where $t^{IK} = t^{KI}$ is a real number representing the quantum mechanical amplitude that an electron hops from I to K, $c^{\dagger,I\sigma}$ is the creation operator at the lattice site I for the spin σ ($\uparrow$ or $\downarrow$), $c^{I\sigma}$ is the annihilation operator, and $N^{I\sigma} = c^{\dagger,I\sigma} c^{I\sigma}$ is the number operator (the observable that counts the number of electrons of spin σ at lattice site I : it can only have the values 0 or 1 because of Pauli exclusion principle). $U^I > 0$ is a constant called the U term in the Hubbard model. It represents the non-linear interaction energy raise when two electrons occupy the same orbital on a given lattice site. This is an extremely short-range interaction, in contrast with the Coulomb force. It can be seen as if the Coulomb interaction is screened by the electrons in different orbital states. It is interesting to note that in H_{hop}, the electron behaves like a wave while in H_{int} it behaves like a particle. This can be shown by a deeper analysis of the two terms (see Ref. [35]) but it is also quite physically understandable. The competition between the wave-like and the particle-like characters leads to many interesting physical properties mentioned before. When both Hamiltonians play a non-negligible role in the description of the electrons of the crystal, an analytical solution is impossible to find. However, a numerical treatment is possible.

4.1.2 Application of Hubbard model for DFT+*U*

The total energy of a system can be computed with DFT+U and can be written as

$$E_{\mathrm{DFT}+U}[n(\mathbf{r})] = E_{\mathrm{DFT}}[n(\mathbf{r})] + E_{\mathrm{Hub}}[g^{I\sigma}_{mm'}] - E_{\mathrm{dc}}[g^{I\sigma}] \tag{4.4}$$

where $n(\mathbf{r})$ is the density, E_{DFT} is the energy computed with DFT and E_{Hub} is the correction containing the Hubbard Hamiltonian to model correlated states. The term E_{dc} will be explained later. $g^{I\sigma}_{mm'}$ are the occupation numbers of localized orbitals defined by

$$g^{I\sigma}_{mm'} = \sum_{k,\nu} f^{\sigma}_{k\nu} \left\langle \psi^{\sigma}_{k\nu} \middle| \phi^{I}_{m'} \right\rangle \left\langle \phi^{I}_{m} \middle| \psi^{\sigma}_{k\nu} \right\rangle \tag{4.5}$$

where m is the state index (the eigenstates of L_z, the z component of the angular momentum operator, for a certain angular quantum number l), k is the k point of reciprocal space, ν is the band index, $f^{\sigma}_{k\nu}$ is the occupation of the Kohn-Sham states, ψ are the Kohn-Sham orbitals (noted as ϕ^{KS} in Appendix C) and ϕ are the states of a localized basis set of choice. The following notations are adopted :

$$g^{I\sigma}_{m} = g^{I\sigma}_{mm}, \tag{4.6}$$

$$g^{I\sigma} = \sum_{m} g^{I\sigma}_{m}, \tag{4.7}$$

$$g^{I} = \sum_{\sigma} g^{I\sigma}. \tag{4.8}$$

The correction E_{Hub} in (4.4) is simply added to the DFT energy, which means that there is a double-counting of the correlated electrons. In order to prevent this double-counting, the contribution of these electrons to the DFT energy is removed (E_{dc}). This term is not uniquely defined and different formulations exist. Two of them are most widely used : the Around Mean-Field (AMF) and Fully Localized Limit (FLL) implementations of DFT+U. The AMF gives better results in the case of materials where electrons are weakly correlated, while the FLL is better for strongly correlated systems. The latter is therefore more popular and will be described here : it is the one which has been used in this work. In the simplest FLL formulation, the energy is corrected in the following way :

$$E_{\mathrm{DFT}+U}[n(\mathbf{r})] = E_{\mathrm{DFT}}[n(\mathbf{r})] + \sum_{I} \left(\frac{U^I}{2} \sum_{m,\sigma \neq m',\sigma'} g^{I\sigma}_{m} g^{I\sigma'}_{m'} - \frac{U^I}{2} g^{I} \left(g^{I} - 1 \right) \right) \tag{4.9}$$

with U^I the Hubbard correction term at atomic site I, also called the effective (screened) Coulomb interaction. It should be noted that the formulation introduced here is not invariant under a rotation of the atomic orbital basis set. Another formulation, invariant under such a transformation, is usually wanted and has been derived. The expression of the correction is in this case more general and, for example, the double-counting energy is given by

$$E_{\mathrm{dc}}[g^{I}] = \sum_{I} \left(\frac{U^I}{2} g^{I} \left(g^{I} - 1 \right) - \frac{J^I}{2} \left(g^{I\uparrow} \left(g^{I\uparrow} - 1 \right) + g^{I\downarrow} \left(g^{I\downarrow} - 1 \right) \right) \right) \tag{4.10}$$

where J is the correction for the exchange interaction, which needs to be determined. It is a higher-order parameter than U and is usually much lower ($J \approx 10\%$ of U), except in the case of Fe superconductors. In a simplified formulation of the rotationally invariant one, the correction can be written as

$$E_{\mathrm{Hub}}[g^{I\sigma}_{mm'}] - E_{\mathrm{dc}}[g^{I\sigma}] = \sum_{I,\sigma} \frac{U^I_{\mathrm{eff}}}{2} \mathrm{Tr} \left(\mathbf{n}^{I\sigma} \left(1 - \mathbf{b}^{I\sigma} \right) \right) \tag{4.11}$$

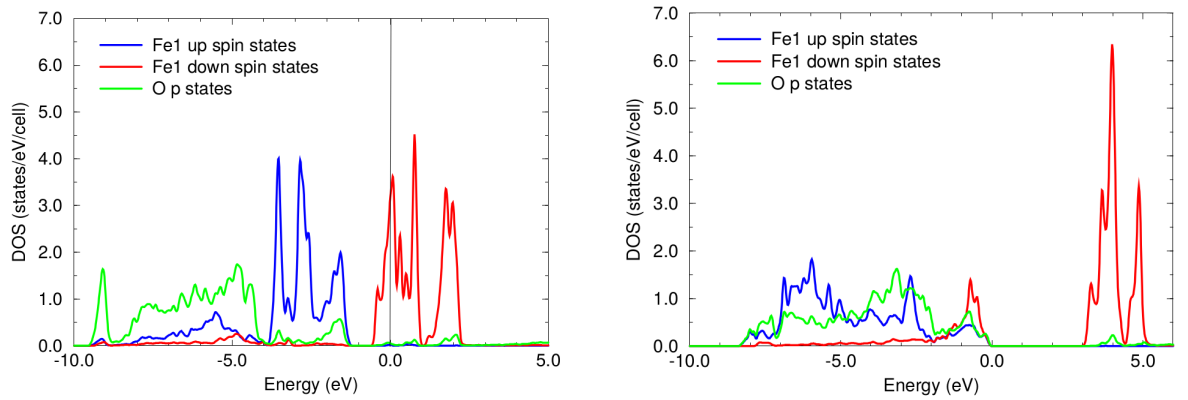

(a) (b)

Figure 4.2: Density of states of Fe_2SiO_4 obtained with (a) GGA and (b) GGA+U [32]. The material should be a metal according to GGA, while it is correctly predicted to be an insulator using GGA+U.

where U_{eff} is the effective correction. It is usually written as $U_{\text{eff}} = U - J$. This expression of U_{eff} is actually an artificial way to take the exchange correction into account. This approach can be discussed, because it is not completely justifiable.

The Hubbard correction in Eq. (4.4) may open the band gap obtained with usual DFT. In some cases, DFT predicts that a material is a metal, while it is actually an insulator. This material is then called a Mott insulator if the top of the valence band and the bottom of the conduction band are of same character, which means that a particular band is not completely filled but the material is insulating. The band actually splits in two due to electron-electron interactions. The use of DFT+U corrects this wrong prediction, as it can be seen for Fe_2SiO_4 in Fig. 4.2.

4.2 Determination of the coupling U

As Eq. (4.11) suggests, the results of the correction depend drastically on the value of U_{eff}. The determination of this parameter is however not trivial. Moreover, the value of U_{eff} for the given orbitals of an atom should be determined each time this atom is found in a crystal : there is not only one U_{eff} for one type of atom. Usually, a semi-empirical way is followed : many different values are used, and the one leading to a good agreement with experimental measures is chosen. Because this procedure is not formal, there is not only one way to determine U_{eff}. The chosen method should therefore be mentioned in every DFT+U work. For example, the value of U can be chosen such that the computed band gap corresponds to the real one. Another possibility is to choose U such that the experimental and theoretical absorption spectra correspond. The first approach has been chosen in this work.

One way to theoretically compute U is the linear response technique. Fig. 4.3 shows the evolution of the energy with the number of electrons in a system. Usual DFT is very efficient to measure the difference of energy between states of integer occupancy. The physical situation between these integer numbers of electrons (approximately linear evolution) can be recovered using DFT+U with U being equal to the curvature of the DFT curve (LDA or GGA). In other words, a first approximation is to use [31]

$$U = E[N+1] - 2E[N] + E[N-1] = \frac{d^2E}{dn^2}. \tag{4.12}$$

U can thus be computed *ab initio*. It should be noted that it is not necessary for the occupation to vary by one electron : the occupation shift can be infinitesimal, and a perturbation approach

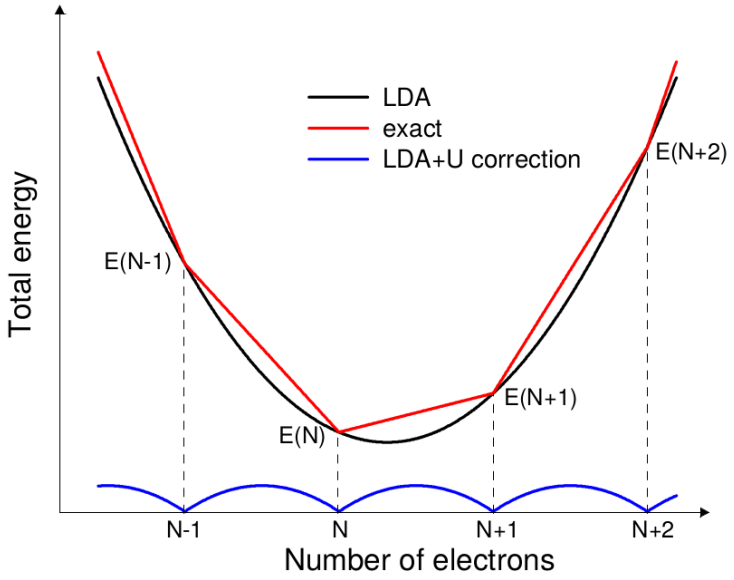

Figure 4.3: Total energy profile as a function of the number of electrons [33].

can thus be adopted.

Chapter 5

Ab initio results

Contents

Ab initio computations are the main part of this master thesis which makes this chapter crucial. They have been realized using the ABINIT code. It is a package developed mainly at the Université Catholique de Louvain. The description of ABINIT given on the website devoted to its presentation, development, distribution,... is the following [36] :

"ABINIT *is a package whose main program allows one to find the total energy, charge density and electronic structure of systems made of electrons and nuclei (molecules and periodic solids) within Density Functional Theory, using pseudopotentials and a planewave or wavelet basis.* ABINIT *also includes options to optimize the geometry according to the DFT forces and stresses, or to perform molecular dynamics simulations using these forces, or to generate dynamical matrices, Born effective charges, and dielectric tensors, based on Density-Functional Perturbation Theory, and many more properties. Excited states can be computed within the Many-Body Perturbation Theory (the GW approximation and the Bethe-Salpeter equation), and Time-Dependent Density Functional Theory (for molecules).*"

First, the different necessary convergence studies are realized. The value of the Hubbard U term which has been used for Cr atoms is also determined. The crystal structure, the band structure and the density of states are then determined for $LaCrO_3$, different x in $La_{1-x}Sr_xCrO_3$ corresponding to different levels of doping and $SrCrO_3$ in order to determine the effects of the replacement of La atoms by Sr ones. The results are analysed and interpreted from the small-polaron model point of view. The formation energies of the different compounds are also computed. Finally, the absorption coefficient and the transmittance are roughly computed for $LaCrO_3$. When possible, comparisons with available experimental data presented in Chapter 2 are realized.

5.1 Convergence study

The first step in any *ab initio* simulation is to study the convergence of the total energy and the unit cell parameters of the studied material with respect to some crucial variables like the cut-off energy for the plane wave basis set or the number of k points used to sample the Brillouin zone. Indeed, if these parameters are very high, precise values of the properties of the studied material will be obtained, but the computation time will also be extremely large. In ABINIT, the scaling for this time with the cut-off energy (`ecut`) is $\mathcal{O}(\texttt{ecut}^3 \log \texttt{ecut})$ and is linear with the number of k points. This shows that it is important to determine the good parameters for given convergence criteria.

The PAW atomic datasets that are used in this work are the JTH ones [37]. The Generalized Gradient Approximation (GGA) is used with the PBE (Perdew, Burke and Ernzerhof) functionals.

The convergence studies have been realized for $LaCrO_3$ and for $SrCrO_3$, considering in the following that the determined parameters also suit for $La_{1-x}Sr_xCrO_3$. The complete convergence studies can be found in Appendix D. It shows that for $LaCrO_3$ as well as for $SrCrO_3$, the choice $E_{\text{cut}} = 30$ Ha (cut-off energy), $E_{\text{cut}}^{\text{PAW}} = 50$ Ha (cut-off energy for the double grid) and `ngkpt` $= 6 \times 6 \times 6$ (k-points sampling) leads to a precision of 0.5 mHa (13.6 meV) per atom in the unit cell for the total energy, and the cell parameters are less than 2% shorter or longer than the asymptotic values.

5.2 Determination of the value of U

In order to correctly model the properties of $La_{1-x}Sr_xCrO_3$, the first step is to determine the appropriate U term corresponding to the Cr atoms. It is indeed around these atoms that charge carriers are localized in d states. The technique used to determine the appropriate U has been to compute the band gap of $LaCrO_3$ for different values of U. The U giving the experimental value of the band gap ($E_g = 2.8$ eV) has then been chosen. The crystal structure that has been

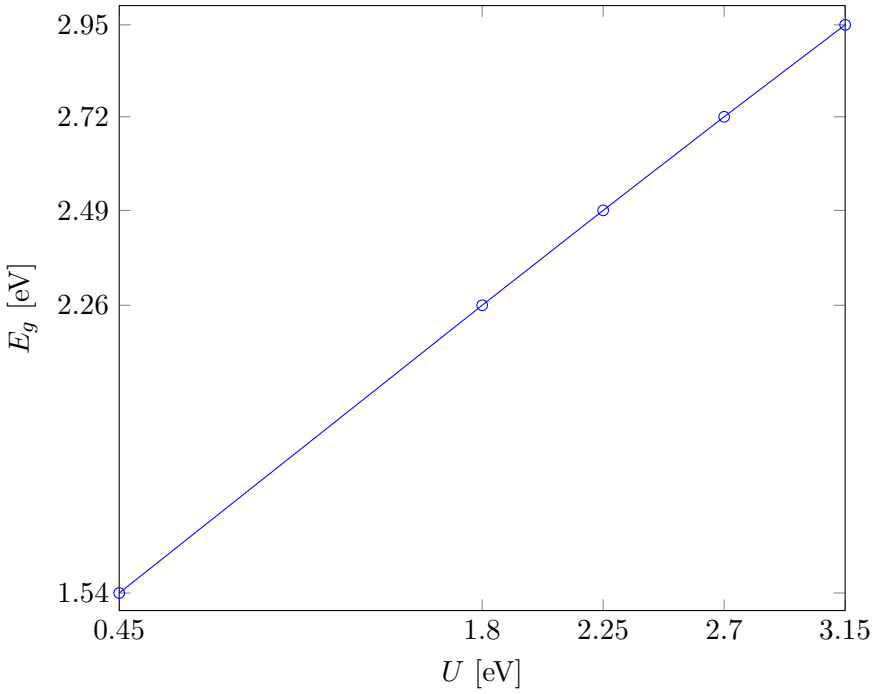

Figure 5.1: Evolution of the band gap E_g of $LaCrO_3$ with U. A linear relationship is observed, which allows to estimate that $U = 2.85$ eV is needed to obtain $E_g = 2.8$ eV, the experimental value.

used for the computation of the band gap was fixed and has been chosen as the one obtained with $U = 2$ eV, a value supposed to be close to the exact one. It should not change too much with a U close to 2 eV, which has been confirmed afterwards. Fig. 5.1 represents the evolution of the band gap with the U term. A linear relationship is observed, which allows to estimate that $U = 2.85$ eV is needed to reach $E_g = 2.8$ eV. J has been set to 0 so that $U_{\text{eff}} = U$ in this work.

5.3 $LaCrO_3$

The first boundary of $La_{1-x}Sr_xCrO_3$ is first analysed. The crystal structure is completely determined, as well as the magnetic properties of $LaCrO_3$. The band structure and the density of states around each atom are then computed.

5.3.1 Crystal structure

A smearing of the occupation number first needs to be imposed. Indeed, $SrCrO_3$ is supposed to be a metal and therefore needs a given smearing and occupation function. In order to be able to compare the energies of the different structures, a smearing has then also been imposed for $LaCrO_3$, even if it is an insulator. The approximation of a Gaussian smearing has been used in this work. The broadening needs to be quite small, but depends on the k-points sampling of the Brillouin zone : the smaller the smearing, the higher the density of k points needs to be in order to avoid numerical errors. It has been determined that for a $6 \times 6 \times 6$ grid, a Gaussian smearing with a temperature corresponding to 0.01 Ha (the smallest value considered for $SrCrO_3$, see Section 5.5) is converged : the structure is the same as the one obtained with a $8 \times 8 \times 8$ grid and the energy change is on the order of the nano Ha for each atom.

The structure of $LaCrO_3$ can then be computed. The structure provided by the Materials Project [38] has been chosen as the starting point for the structural relaxation. The result

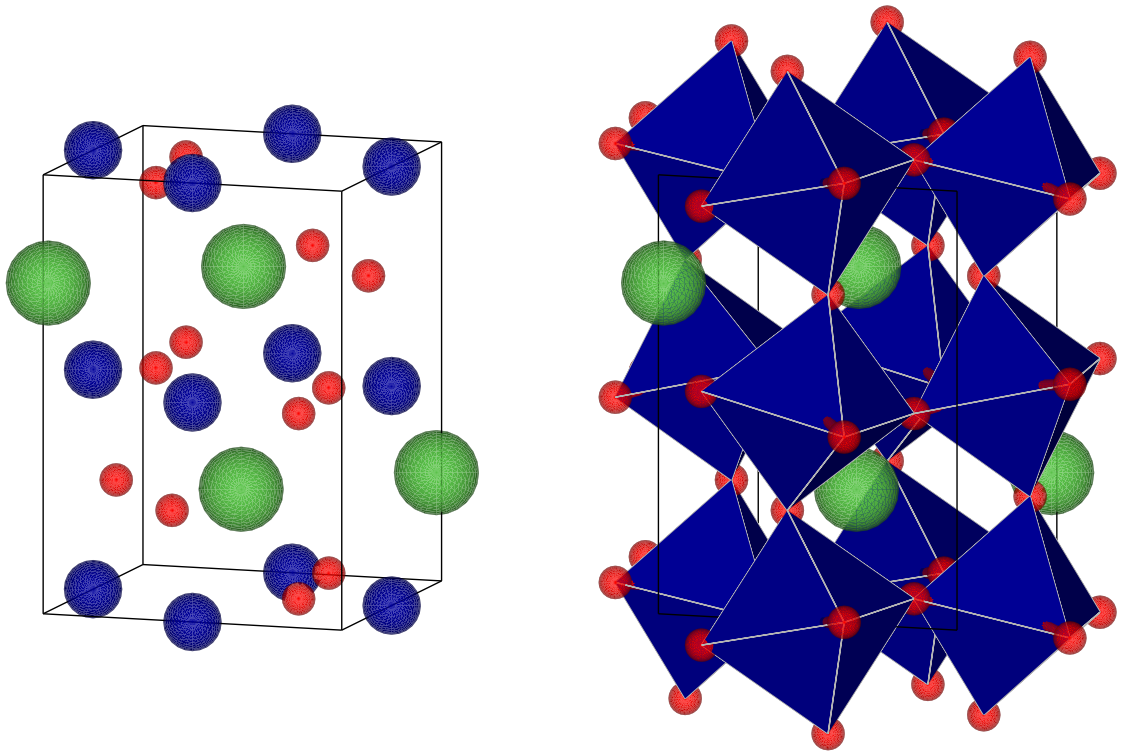

(a) (b)

Figure 5.2: (a) Computed unit cell of $LaCrO_3$. (b) Representation of the octahedra around Cr atoms. Dark green : La, blue : Cr, red : O.

obtained is indeed a distorted orthorhombic perovskite. The unit cell parameters are given in Table 5.1, where they are compared to experimental values, and in Table 5.2, where they are compared to the cell parameters of the other structures. The structure is represented in Fig. 5.2, and the atomic positions are given in Table E.1. The errors on the cell parameters lie in the usual range (2% within DFT).

Table 5.1: Computed unit cell parameters of $LaCrO_3$.

	a [Å]	b [Å]	c [Å]
Expt.	5.52	5.49	7.76
GGA+U	5.57	5.56	7.85
Error [%]	0.9	1.3	1.2

5.3.2 Magnetic properties

In $LaCrO_3$, each Cr atom is at the center of an octahedron formed by its six closest O neighbours. These O anions produce a static electric field that lifts the degeneracy of the Cr $3d$ orbitals : they are separated in three t_{2g} orbitals and two e_g ones (crystal field splitting), as it is represented in Fig. 5.3(a). An isolated Cr atom has the $[Ar]3d^5 4s^1$ electron configuration. In $LaCrO_3$, each Cr atom is in the Cr^{3+} state, and has the $[Ar]3d^3$ configuration. There are three electrons located on the t_{2g} orbitals, as it is represented in Fig. 5.3(b). Usually, the high-spin configuration is adopted. In this case, a magnetic moment of about $\pm 3\mu_B$ should be found on each Cr atom. An approximate value of $\pm 2.7\mu_B$ has been obtained (and is reported in Table 5.4 which compares the magnetic moments around Cr atoms for each considered x in $La_{1-x}Sr_xCrO_3$),

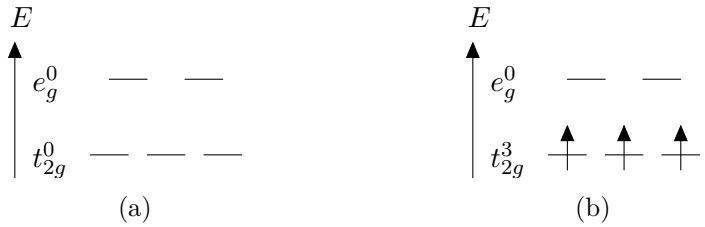

Figure 5.3: Schematic representation of the Cr $3d$ states (a) in an octahedron and (b) in the case of $LaCrO_3$.

which confirms the high-spin configuration. The structural relaxation has been realized first considering an antiferromagnetic ordering (the magnetic moments of the Cr atoms cancel each other), and then a ferromagnetic one (the magnetic moments point in the same direction). The ferromagnetic structure lies 0.1 eV/at. above the antiferromagnetic one, and the material is thus antiferromagnetic. This result is in agreement with experiments.

5.3.3 Band structure

The band structure of a material is an important characteristic of its electronic structure. The path in k-space along which the bands have been computed is defined as $\Gamma - X - S - Y - \Gamma - Z - U - R - T - Z|Y - T|U - X|S - R$ in order to correspond to what is found in literature for orthorhombic cells [39]. Fig. 5.4 represents the Brillouin zone of an orthorhombic unit cell and locates the symmetry points used to define the path.

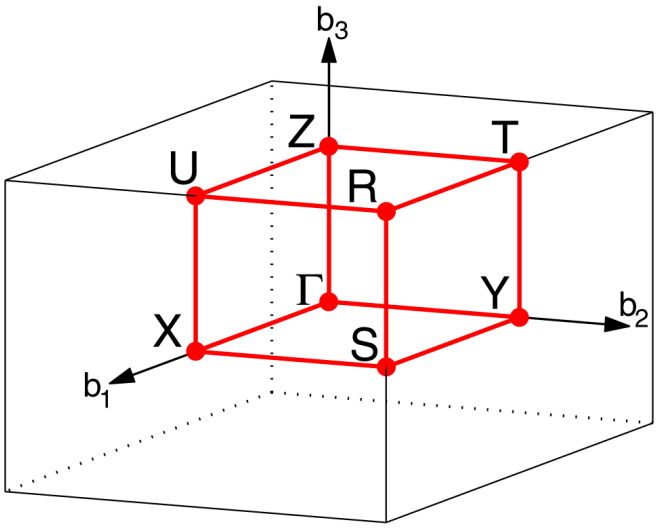

Figure 5.4: Brillouin zone of an orthorhombic unit cell [39].

Both experiments and computations indicate that $LaCrO_3$ is an antiferromagnetic crystal. Nevertheless, the computation of the band structure for the Materials Project [38] considered a ferromagnetic material. It is given in Fig. 5.5. In order to validate the calculation for the antiferromagnetic material, the computation has also been realized for the ferromagnetic one. The band structure in this case is represented in Fig. 5.6. Both computations give similar results. The band structure obtained for the antiferromagnetic $LaCrO_3$ is given in Fig. 5.7. As expected, the band gap is of 2.8 eV with $U = 2.85$ eV.

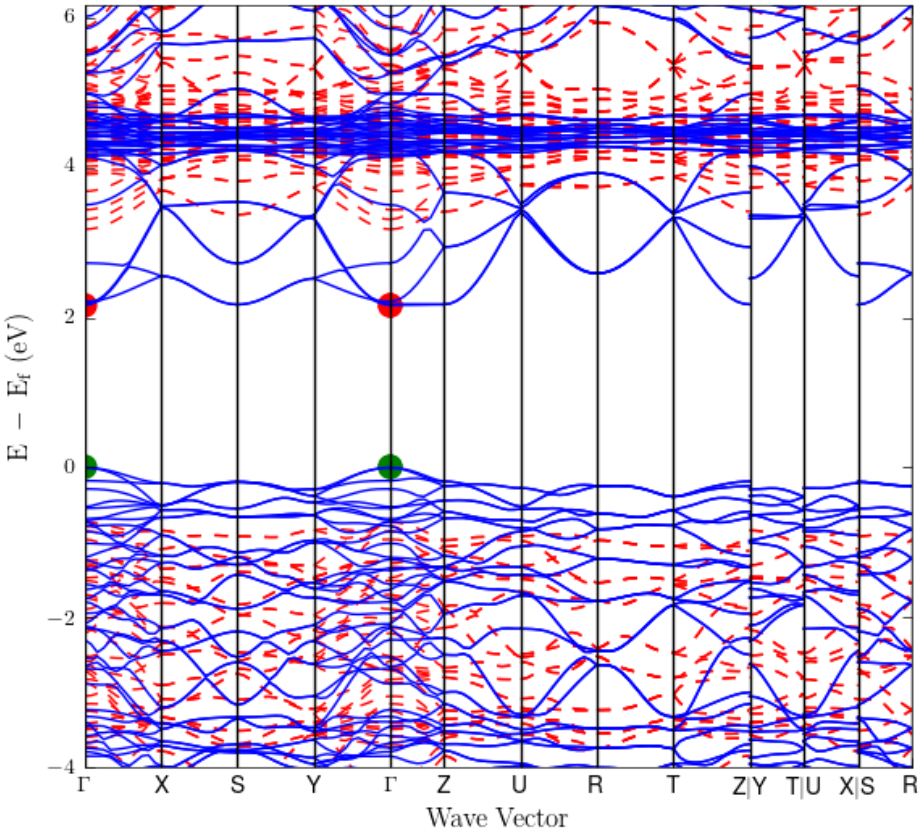

Figure 5.5: Band structure of ferromagnetic $LaCrO_3$ computed with $U = 3.7$ eV (obtained with VASP and other atomic data) for the Materials Project [38]. The red and blue colors represent states of opposite spins.

5.3.4 Density of states

The projected density of states (DOS) has been computed around each atom of $LaCrO_3$ by projecting the density on atomic orbitals around selected atoms. The results are given in Figs. 5.8, 5.9 and 5.10. In these plots, the usual convention is used to represent the contributions of spin-up and spin-down electrons : the spin-down DOS is represented in the negative part of the plot. Fig. 5.8 confirms that the antiferromagnetic state is due to the opposite magnetic moments of Cr atoms (which has already been mentioned after the computation of these moments), all other atoms having the same contributions to the projected DOS for the spin-up and spin-down electrons. Figs. 5.9, and 5.10 show that the transition at the band gap is mainly due to the d orbitals of the Cr atoms hybridized with a little bit of the O orbitals (mainly of p character), which corresponds to what has been deduced by Zhang *et al.* [1] (see Fig. 2.11(c)).

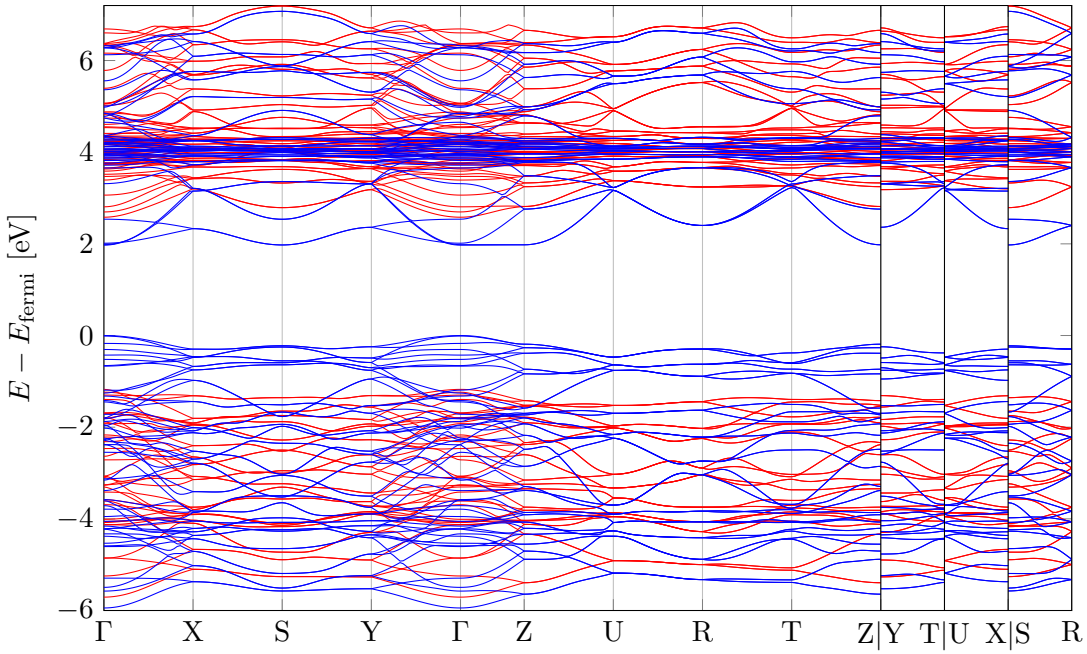

Figure 5.6: Band structure of ferromagnetic $LaCrO_3$ computed with $U = 2.85$ eV. The red and blue colors represent states of opposite spins.

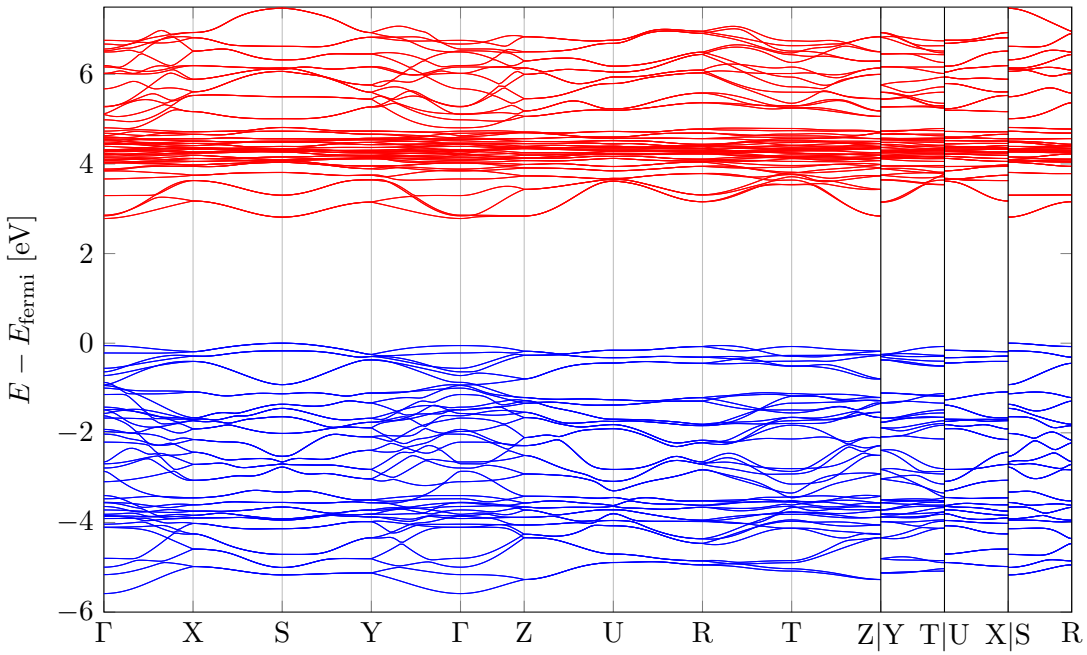

Figure 5.7: Band structure of antiferromagnetic $LaCrO_3$. The obtained band gap is of 2.8 eV for $U = 2.85$ eV. Blue states are occupied at $T = 0$ K, and red ones are not.

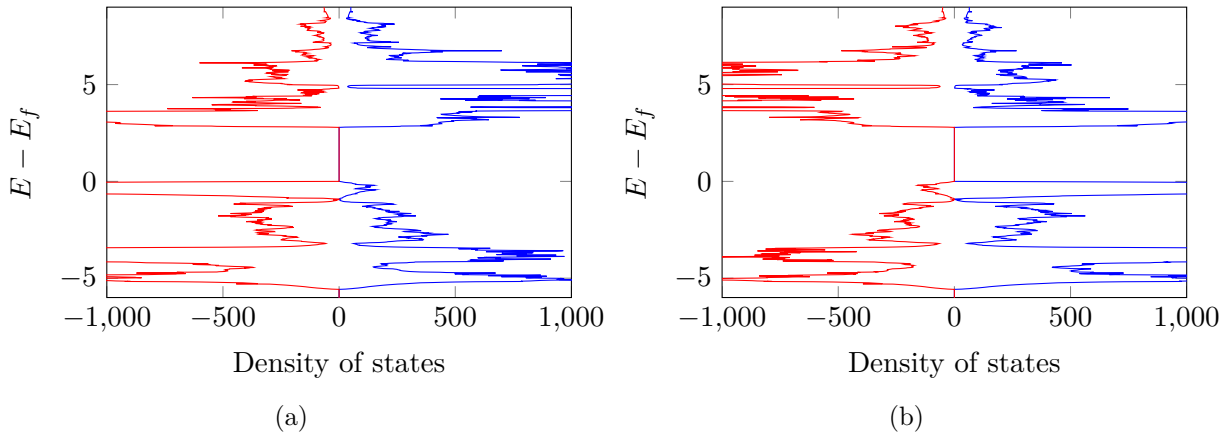

Figure 5.8: Sum of the projections of the DOS on atomic orbitals around Cr atoms of opposite magnetic moment in $LaCrO_3$. The material is indeed antiferromagnetic.

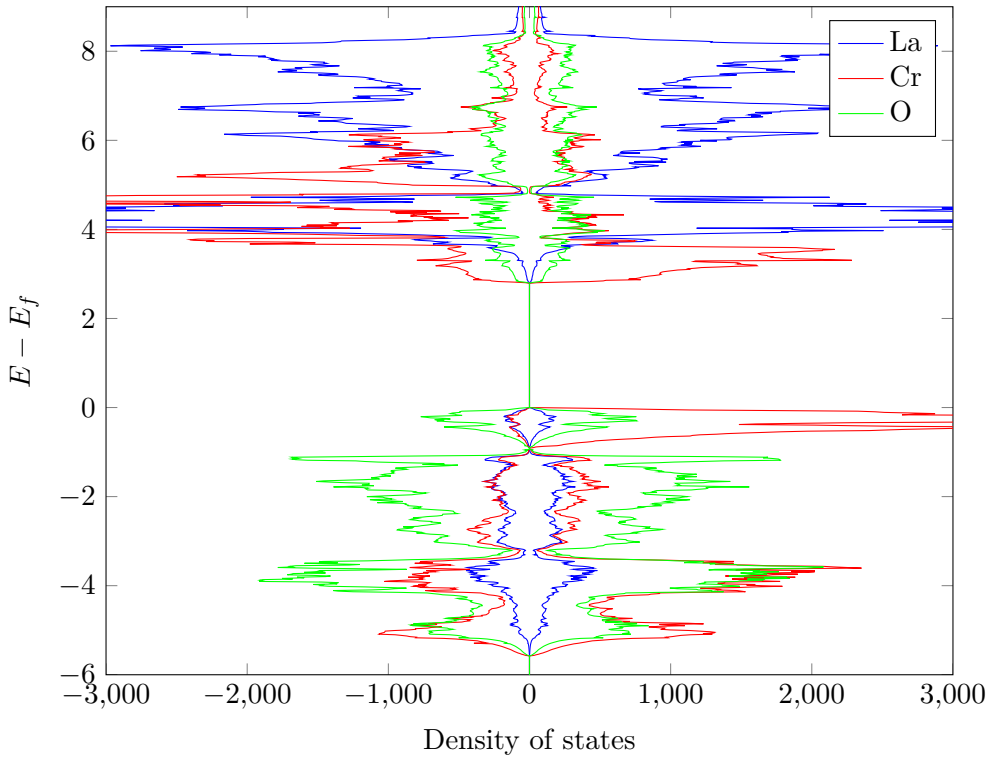

Figure 5.9: Comparison between the sum of the projections of the DOS on atomic orbitals around the atoms of $LaCrO_3$. At the band gap, the contribution of the orbitals around Cr atoms is more important than the one around the other atoms.

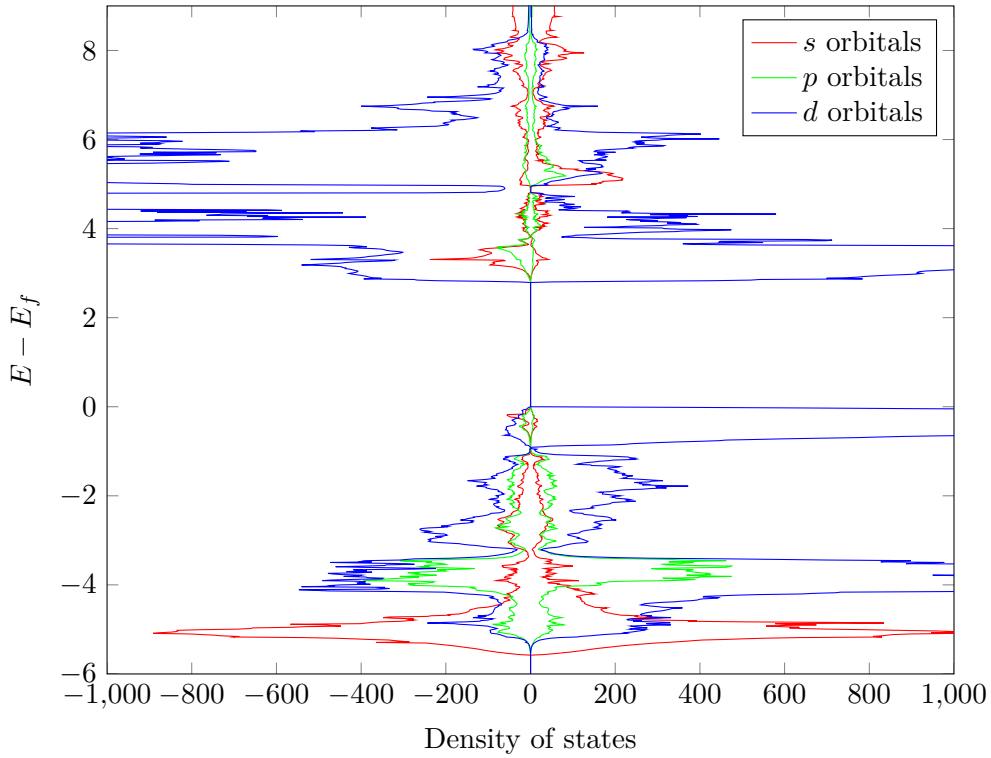

Figure 5.10: Comparison between the projections of the DOS on atomic orbitals around a Cr atom in $LaCrO_3$. At the band gap, the contribution of the d orbitals is much larger than the contribution of the other orbitals.

5.4 $La_{1-x}Sr_xCrO_3$

Now that the properties of $LaCrO_3$ have been determined, it is possible to analyse the effects of the replacement of La atoms by Sr ones. The chosen values of x are 0.25, 0.50 and 0.75. Each one of the corresponding materials is completely described following the same steps as for $LaCrO_3$. The crystal structure is first computed. In every case, the number of independent configurations is infinite. Indeed, theoretically, the number of unit cells can always be increased and the location of doping element can be chosen for each configuration. In this work, only one configuration has been considered for each x. Each time, the relaxation has been realized imposing the relaxed structure of $LaCrO_3$ as the starting point of the calculation in order to maintain the perovskite structure.

Small polarons are expected to appear in these materials. A first observation of this phenomenon is made possible by the localization of holes around Cr atoms : it is expected that each hole will localize on one Cr atom. These atoms should then be in the Cr^{4+} state instead of the Cr^{3+} one : one electron is removed (one hole is added) from (on) the t_{2g} orbitals. All other Cr atoms should be in the initial Cr^{3+} state, as represented in Fig. 5.3(b). The estimation of the magnetic moments around Cr atoms can thus be a first observation of the emergence of polarons in $La_{1-x}Sr_xCrO_3$ and is realized at the same time as the determination of the crystal structure.

The band structures have also been determined. Sometimes, a rigid band structure model can be adopted to describe a doped material because the doping level is very low. In this case, the percentages are too large to apply this model : the structures change too much. This is why the structural relaxation was necessary in all cases. The projected DOS has also been computed in the case of $x = 0.25$.

5.4.1 $La_{0.75}Sr_{0.25}CrO_3$

Crystal structure and magnetic properties

For $x = 0.25$, a single $LaCrO_3$ unit cell has been used where a La atom has been replaced by a Sr one. The relaxed structure is represented in Fig. 5.11 and the atomic positions are given in Table E.2. The unit cell parameters are given at Table 5.2. However, this configuration does not present a polaronic state : the magnetic moments around the Cr atoms are all the same ($\pm 2.5 \mu_B$, see Table 5.4). The hole is not localized on a given Cr atom, and the situation can be schematically represented by Fig. 5.12. This state is actually metallic, because there is one free hole delocalized over the crystal. Experimental measures nevertheless show that the transport is due to small-polaron hopping for $x < 0.65$. The polaronic state should therefore be found. In order to do so, the initial structure (before the relaxation) has been changed so that one of the Cr atoms has its O neighbours in the same configuration as in $SrCrO_3$ (the O atoms are closer to the Cr ones in this material). Unfortunately, the relaxation led to the configuration of the metallic material. Another try has been realized, with first a relaxation with a much larger U on one of the Cr atoms. This also led to the metallic state.

Another shot has been given using VASP instead of ABINIT (VASP is another *ab initio* simulation package). Using this software, it has been possible to isolate a polaron in $La_{0.75}Sr_{0.25}CrO_3$. The structure of this polaronic material is represented in Fig. 5.13 and its unit cell parameters are given in Table 5.2. This shows that the structures can be very similar, but small differences can trigger the formation of polarons. Table 5.3 compares the Cr-O bond lengths of the two structures. In the metallic state, all Cr-O bond lengths lie between 1.97 and 2.00 Å, and there is no significant difference between the four Cr atoms. In the polaronic state, the bond lengths decrease for one of the Cr atoms, while all other Cr atoms have longer Cr-O bonds : the O atoms are more localized around one of the Cr atoms. The decrease is represented by the Cr_1-O bond lengths differences in Table 5.3, while the increase is represented

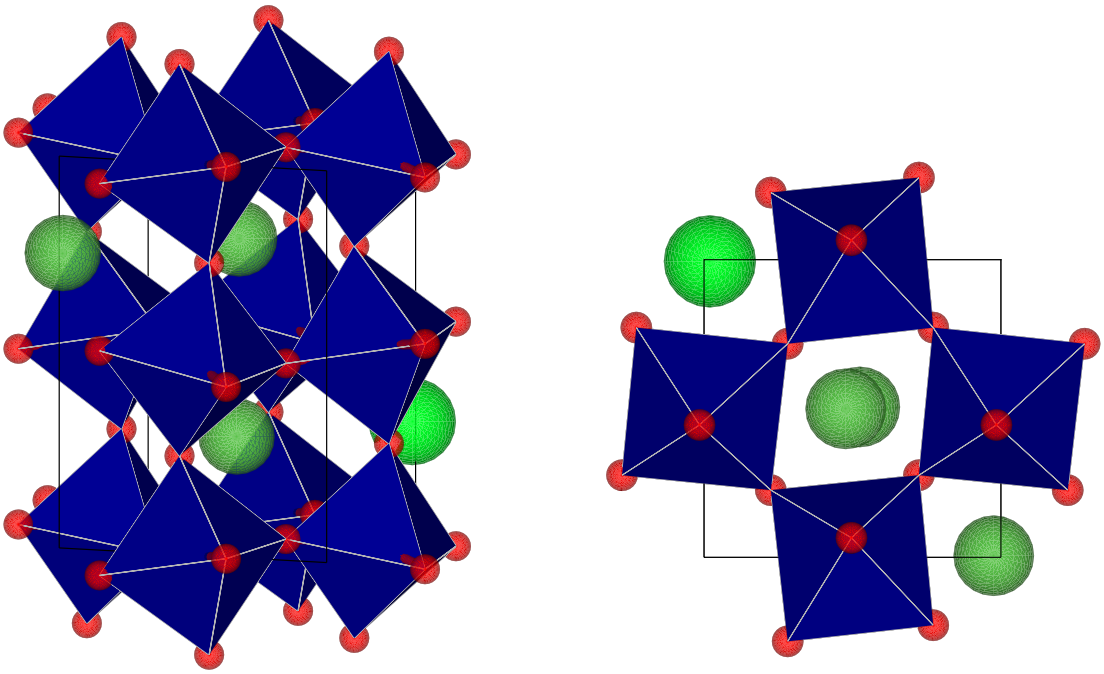

(a) (b)

Figure 5.11: (a) Computed unit cell of metallic $La_{0.75}Sr_{0.25}CrO_3$. (b) View of the unit cell along the **c** axis. Dark green : La, light green : Sr, red : O.

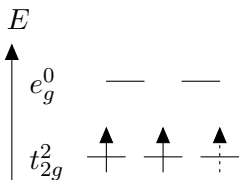

Figure 5.12: Schematic representation of the Cr $3d$ states in metallic $La_{0.75}Sr_{0.25}CrO_3$.

Table 5.2: Computed unit cell parameters of $La_{1-x}Sr_xCrO_3$ as a function of x.

	a [Å]	b [Å]	c [Å]
$LaCrO_3$	5.52	5.49	7.76
$La_{0.75}Sr_{0.25}CrO_3$ (metallic)	5.53	5.54	7.81
$La_{0.75}Sr_{0.25}CrO_3$ (polaronic)	5.58	5.56	7.84
$La_{0.50}Sr_{0.50}CrO_3$	5.50	5.53	7.77
$La_{0.25}Sr_{0.75}CrO_3$	5.48	5.50	7.74
$SrCrO_3$ (smearing of 0.01 Ha)	5.57	5.56	7.85
$SrCrO_3$ (smearing of 0.04 Ha)	5.49	5.50	7.76

by the Cr_2-O bond lengths differences. In this configuration, one of the Cr atoms has a different magnetic moment than the other ones. The value of $\pm 2\mu_B$ is expected on this Cr atom, while all the others keep the same magnetic moment as in $LaCrO_3$. The obtained values are of $-1.9\mu_B$ and $\pm 2.7\mu_B$, which confirms the localization of the hole and the emergence of the polaron.

Table 5.3: Computed Cr-O_i bond lengths in metallic and polaronic $La_{0.75}Sr_{0.25}CrO_3$.

	Metallic	Polaronic	Δ [%]
Cr_1-O_1 [Å]	1.99763	1.97472	−1.15
Cr_1-O_{12} [Å]	1.96759	1.93035	−1.89
Cr_1-O_8 [Å]	1.99651	1.99227	−0.21
Cr_1-O_5 [Å]	1.98034	1.96626	−0.71
Cr_1-O_{10} [Å]	1.97262	1.94135	−1.59
Cr_1-O_3 [Å]	1.98932	1.96849	−1.05
Cr_2-O_{12} [Å]	1.96757	2.04076	+3.72
Cr_2-O_1 [Å]	1.99765	2.05169	+2.71
Cr_2-O_9 [Å]	1.99651	2.01750	+1.05
Cr_2-O_4 [Å]	1.98034	2.00077	+1.03
Cr_2-O_2 [Å]	1.98933	2.01071	+1.07
Cr_2-O_{11} [Å]	1.97261	1.99110	+0.94

Table 5.4: Magnetic moments around Cr atoms in $La_{1-x}Sr_xCrO_3$ as a function of x. This is a rough approximation computed by integrating the total density in spheres around each atom.

	Magnetic moment [μ_B]
$LaCrO_3$	±2.7 (×2)
$La_{0.75}Sr_{0.25}CrO_3$ (metallic)	±2.5 (×2)
$La_{0.75}Sr_{0.25}CrO_3$ (polaronic)	−1.9, 2.7 (×2), −2.7
$La_{0.50}Sr_{0.50}CrO_3$	2.5 (×2); −1.9; −2.3
$La_{0.25}Sr_{0.75}CrO_3$	−1.9 (×2); 1.9; 2.6
$SrCrO_3$	±1.9 (×2)

The origin of the differences between the results obtained with the two softwares (ABINIT giving a metallic state, while VASP gives the polaronic state) has been found to be the used smearing of the occupation. Indeed, VASP uses the tetrahedron method to integrate over the Brillouin zone, while a Gaussian smearing of the occupation has been used with ABINIT. The smearing that has been used in the latter was too large : 0.01 Ha = 0.27 eV. This gave the system the possibility to relax into the metallic state, in other word to lose the polaron. VASP,

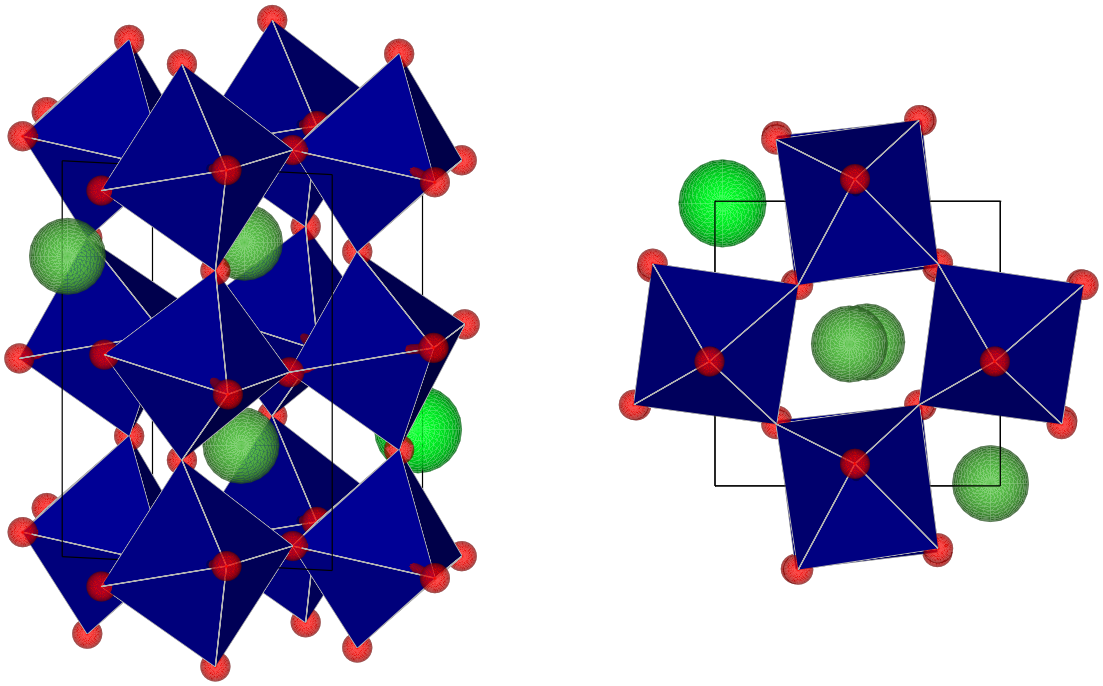

(a) (b)

Figure 5.13: (a) Computed unit cell of polaronic $La_{0.75}Sr_{0.25}CrO_3$. (b) View of the unit cell along the **c** axis. Dark green : La, light green : Sr, red : O.

on the other hand, treats the material as an insulator near 0 K, and therefore does not give the system the same possibility and stabilizes the polaron.

In light of these considerations, different computations have been realized with VASP: the structure has been computed for different smearing temperatures (using this time a Gaussian broadening instead of the tetrahedron method). A transition is indeed observed in the evolution of the magnetic moments around the Cr atoms, as it is represented in Fig. 5.14. The computations have been realized for a fixed k-points grid. The exact values of the magnetic moments are thus not the ones given in this figure, because a denser k-points grid should be used when the smearing temperature decreases. The more precise values computed afterwards are reported in Table 5.4. Nevertheless, Fig. 5.14 gives an idea of what happens. Before a given smearing temperature T^* (the smearing energy is given by kT for a given temperature T), one of the Cr atoms has a lower magnetic moment than the other ones and $La_{0.75}Sr_{0.25}CrO_3$ is in the polaronic state. Above this temperature, the magnetic moment around this Cr atom increases and the magnetic moments around the other three Cr atoms decrease to reach an average value, and the material is metallic.

Zhang *et al.* reported that the charge carrier transport in $La_{1-x}Sr_xCrO_3$ samples is only due to band conduction below a certain temperature T_0, while it is due to both band conduction and small-polaron hopping above T_0 [2]. This means that below T^*, the material is polaronic but the hopping mechanism is activated only above T_0 (corresponding to the activation energy).

It should be noted that the smearing which has been used being Gaussian, the value of the used temperature is not physical. A Fermi-Dirac distribution could be used, for which the value of the used temperature for the smearing would have a more physical meaning. An estimation of this temperature could then be computed.

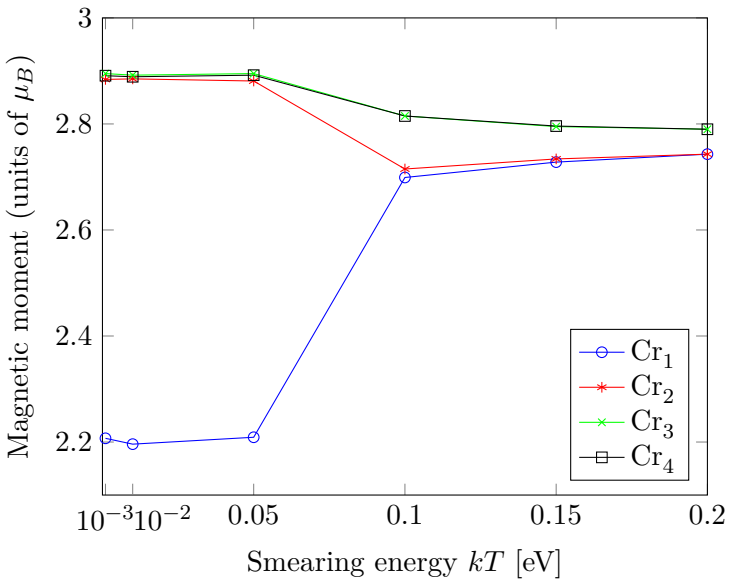

Figure 5.14: Evolution of the magnetic moment of the four Cr atoms in $La_{0.75}Sr_{0.25}CrO_3$ with the smearing temperature. The computations have been realized with VASP for a fixed k-points grid.

Band structure

As it has been mentioned, $La_{1-x}Sr_xCrO_3$ is polaronic for $x = 0.25$, but it also presents a transition to a metallic state when the smearing is high enough (in other words, when the temperature is high enough). Figs. 5.15 and 5.16 represent the band structures of the metallic and the polaronic systems, respectively. The latter has been computed considering the polaronic crystal structure determined with VASP, and the smearing of 0.01 Ha. A single state appears in the forbidden band. This state is thus the consequence of the localization of the hole around one of the Cr atoms due to the crystal structure obtained with the tetrahedron method (similar to a very small smearing). It lies 0.29 eV above the valence band (which explains why a smearing of 0.27 eV during the structural relaxation could lead to the metallic state), and its bandwidth is of 0.17 eV. Other than that, the two band structures have only few differences. The metallic material has many degenerated (or close to be degenerated) states, while in the polaronic one these are well separated.

Density of states

Fig. 5.17 compares the different projections of the DOS on atomic orbitals around the atoms of the metallic material, and Fig. 5.18 details the atomic orbital contributions to the projected DOS around a Cr atom of the same structure. The transition at the band gap looks very much like the one of $LaCrO_3$: it is mainly due to Cr $d - d$ orbitals.

Fig. 5.19 gives the different projections of the DOS on the atomic orbitals around the atoms of the polaronic material. It can be seen that the state appearing in the middle of the forbidden band is mainly due to Cr contributions. Fig. 5.20 compares the contributions of the different Cr atoms in $La_{0.75}Sr_{0.25}CrO_3$. It shows that the DOS is much larger in this localized band around the Cr_1 atom. It is indeed around this atom that the magnetic moment is much lower (see Fig. 5.14) and that the hole is localized. Fig. 5.21 shows that this state is mainly of d character.

In $LaCrO_3$, the three valence electrons of the Cr^{3+} ions occupy the three t_{2g} orbitals (see Fig. 5.3(b)). In the case of polaronic $La_{0.75}Sr_{0.25}CrO_3$, only two electrons are left on the orbitals of the localized Cr atoms, and the empty t_{2g} state actually goes higher in energy than the other two, which creates a small gap. Fig. 5.22 represents this phenomenon. This is the state

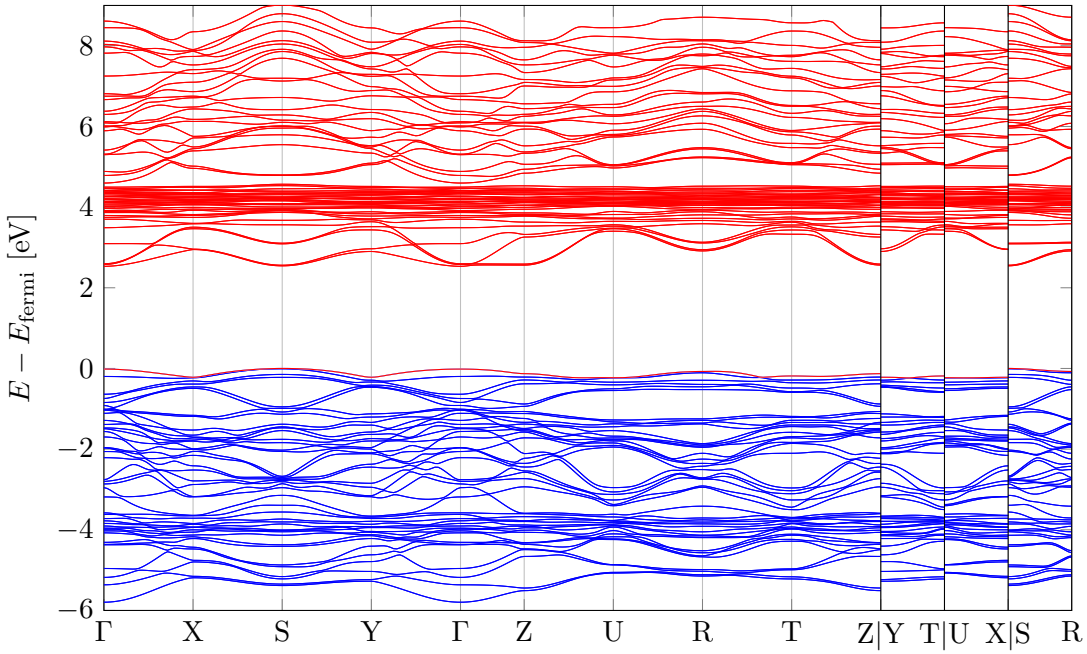

Figure 5.15: Band structure of non-polaronic $La_{0.75}Sr_{0.25}CrO_3$ computed with a smearing of 0.01 Ha. Blue states are occupied at $T = 0$ K, and red ones are not. The material is indeed metallic

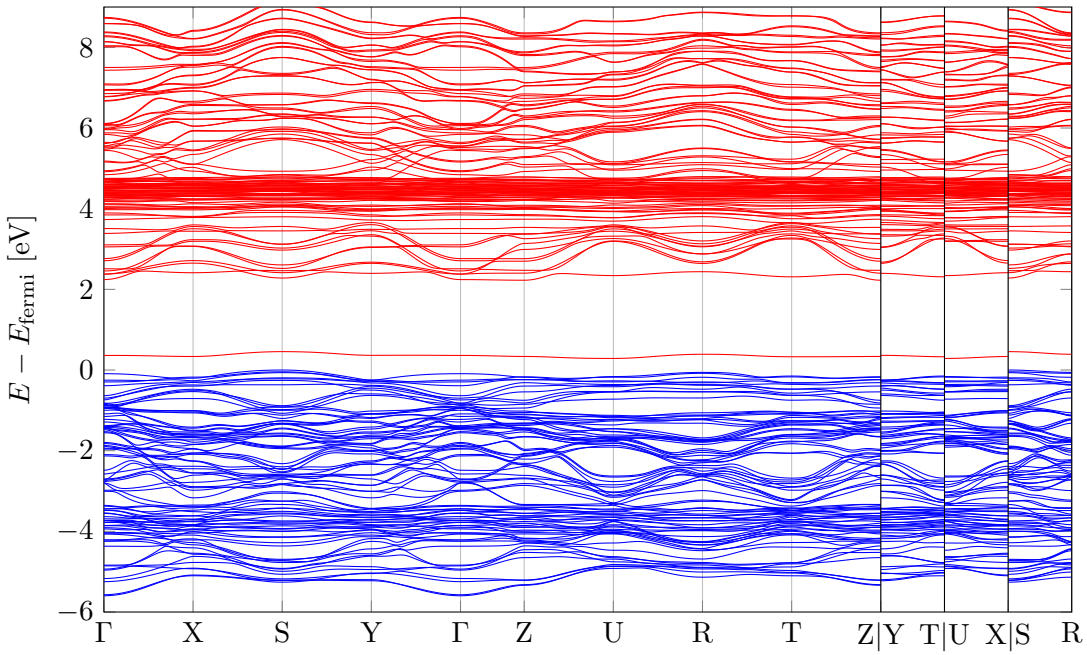

Figure 5.16: Band structure of polaronic $La_{0.75}Sr_{0.25}CrO_3$ computed with a smearing of 0.01 Ha. The crystal structure that has been used for this computation is the one calculated with VASP. Blue states are occupied at $T = 0$ K, and red ones are not.

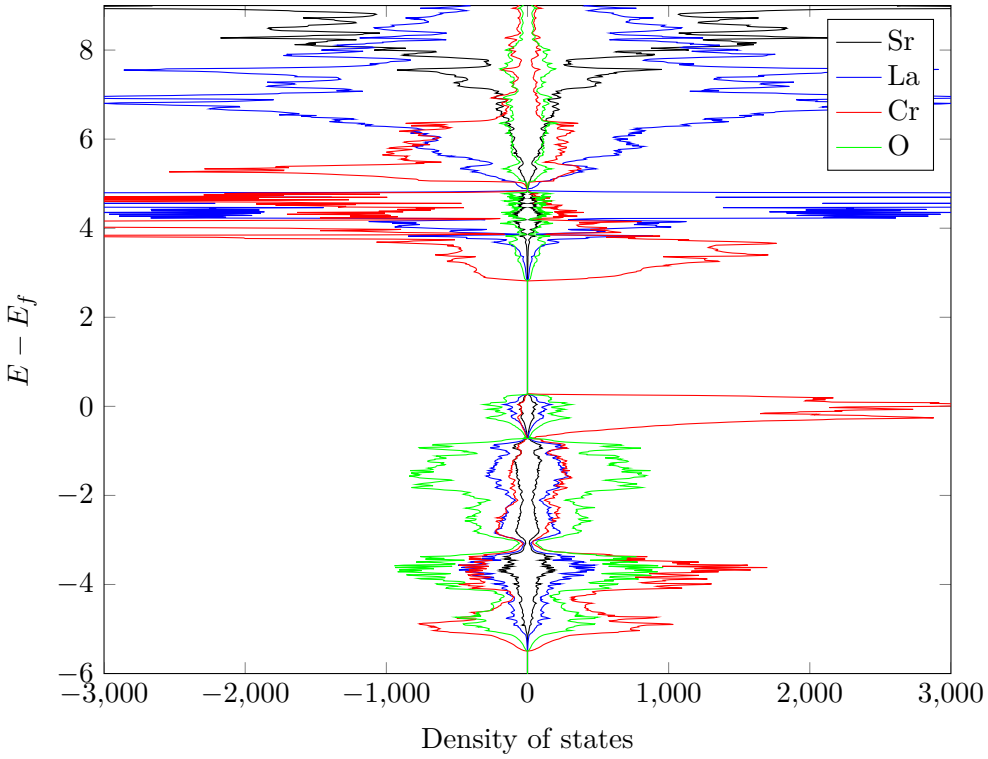

Figure 5.17: Comparison between the sum of the projections of the DOS on atomic orbitals around the atoms of metallic $La_{0.75}Sr_{0.25}CrO_3$.

appearing in the forbidden band, as mentioned by Zhang *et al.* (see Fig. 2.11(d)). The other Cr atoms keep the same configuration as in $LaCrO_3$ (see Fig. 5.3(b)). When the material is metallic (when the smearing temperature is high enough), the hole is delocalized over the four Cr atoms, as it is represented in Fig. 5.12. In this case, there is no localized state in the forbidden band because there is no split of the t_{2g} orbitals.

Polaron energy

The difference of energy between the polaronic and metallic $La_{0.75}Sr_{0.25}CrO_3$ can be computed. These two configurations have been obtained for different smearing temperatures, and the total energies are therefore not directly comparable. Indeed, in order to compare the total energies, the same smearing should be used to find the two structures, which was not possible here. A comparable energy is obtained by subtracting only half of the the entropy contribution to the internal energy. In other words, a smearing-independent energy can be computed by taking the mean between the free energy and the internal energy. This is realized in Fig. 5.23. The computations have been realized with VASP and with a fixed k-points grid. More precise values would be obtained by using denser grids for lower smearing temperatures. It can be seen in this figure that the mean energy jumps to a higher value at the transition temperature T^*. The difference of energy is of 63 meV and is thus equal to the energy needed to go from the polaronic state to the metallic one : the polaronic state is energetically favourable compared to the metallic one.

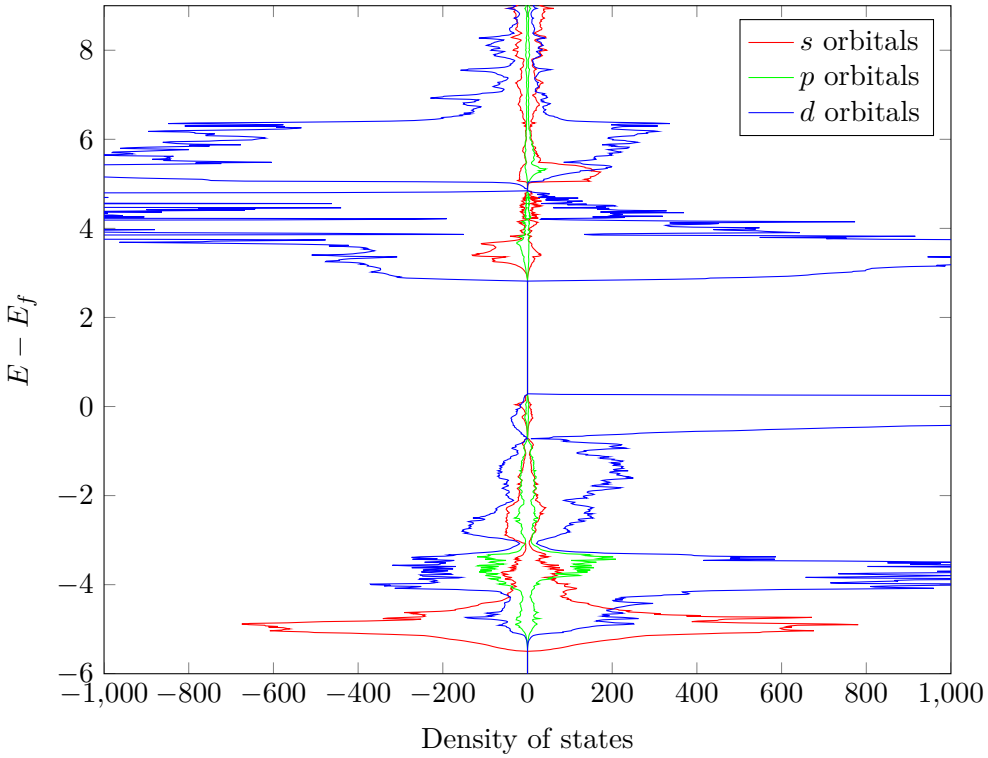

Figure 5.18: Comparison between the projections of the DOS on atomic orbitals around a Cr atom in metallic $La_{0.75}Sr_{0.25}CrO_3$.

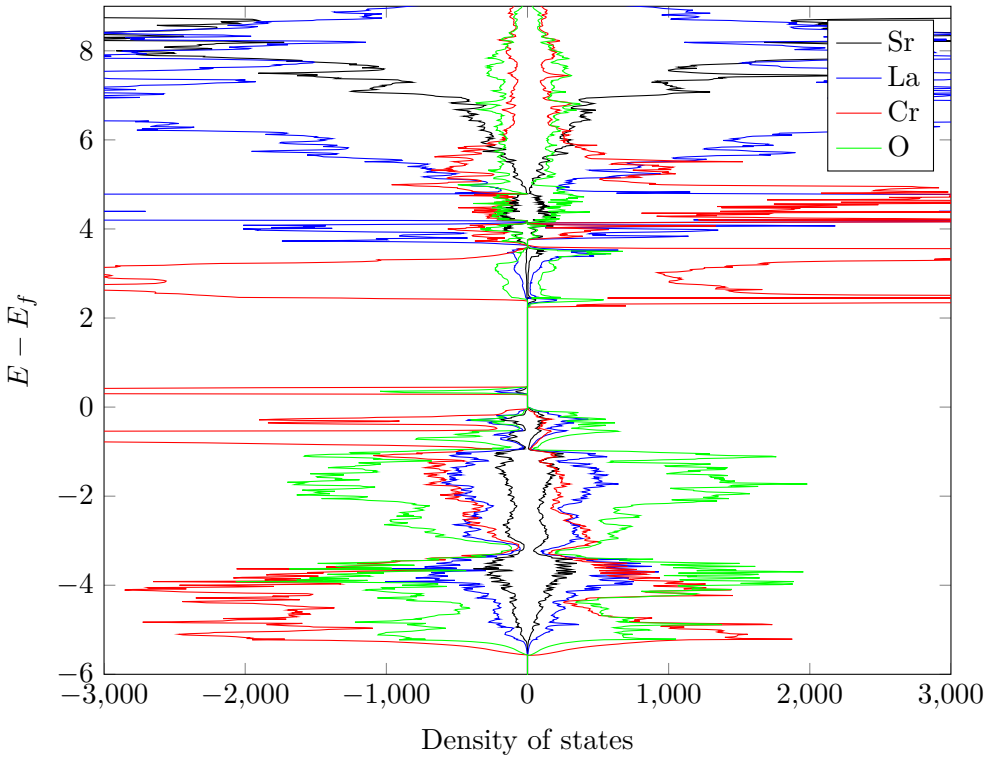

Figure 5.19: Comparison between the sum of the projections of the DOS on atomic orbitals around the atoms of polaronic $La_{0.75}Sr_{0.25}CrO_3$.

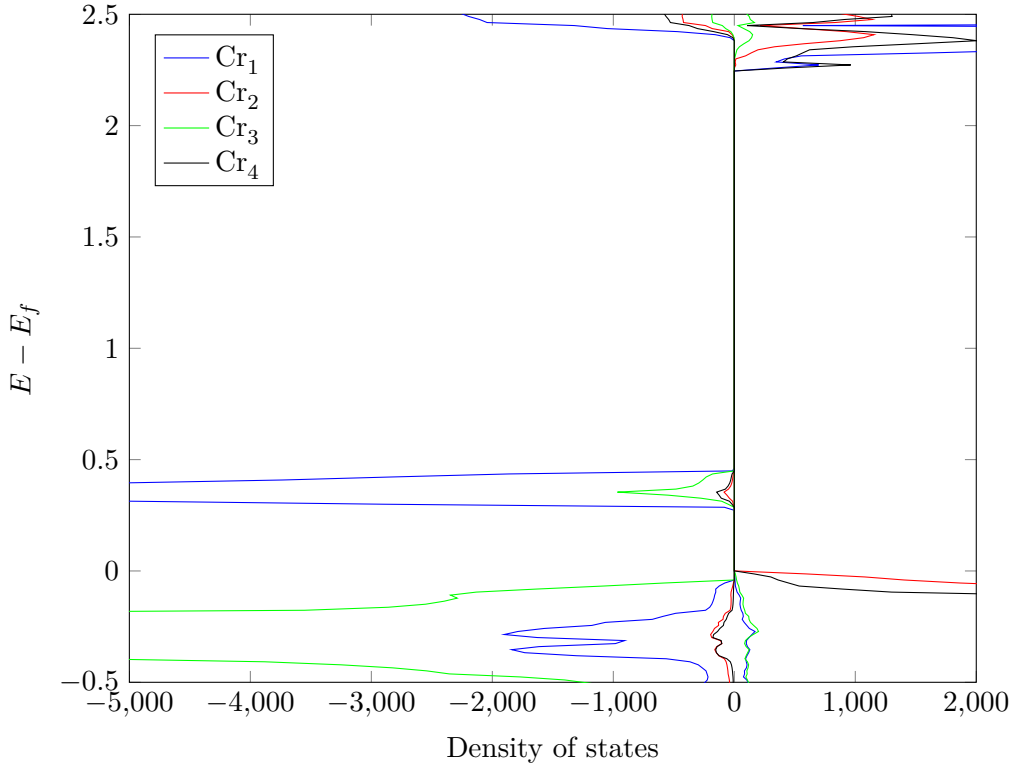

Figure 5.20: Comparison between the sum of the projections of the DOS on atomic orbitals around the Cr atoms in polaronic $La_{0.75}Sr_{0.25}CrO_3$.

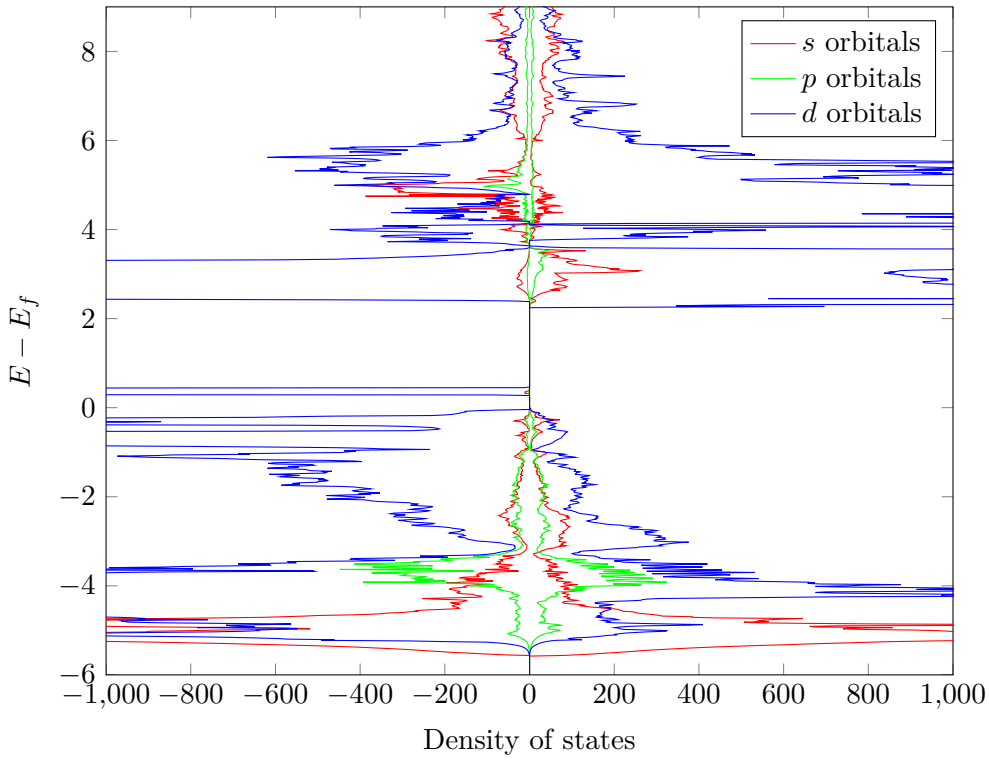

Figure 5.21: Comparison between the projections of the DOS on atomic orbitals around the localized Cr atom in polaronic $La_{0.75}Sr_{0.25}CrO_3$.

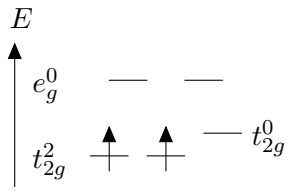

Figure 5.22: Schematic representation of the effect of the localization on the Cr $3d$ states in polaronic $La_{0.75}Sr_{0.25}CrO_3$.

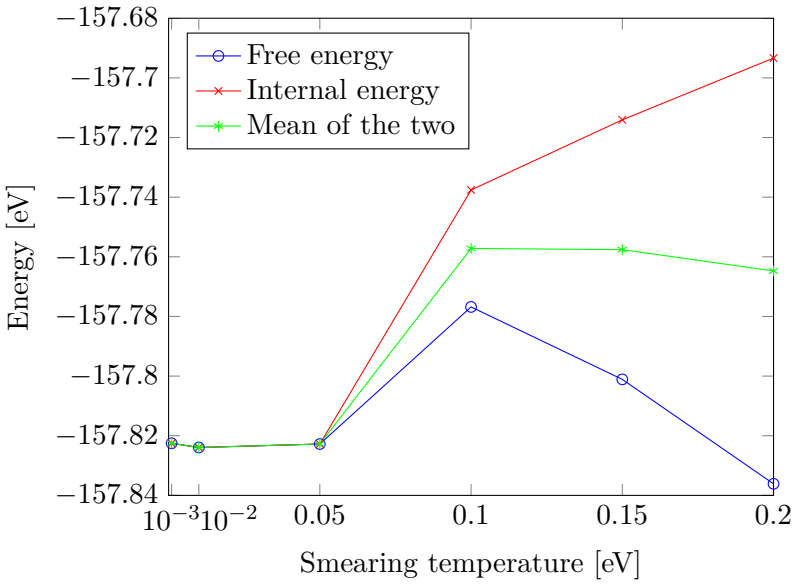

Figure 5.23: Evolution of the energy of $La_{0.75}Sr_{0.25}CrO_3$ with the smearing temperature. The computations have been realized with VASP for a fixed k-points grid.

5.4.2 $La_{0.50}Sr_{0.50}CrO_3$

Crystal structure and magnetic properties

Again, only one structure with one unit cell has been considered in the case of $x = 0.50$. The atomic positions are given in Table E.3 and the unit cell parameters are given in Table 5.2. The structure is represented in Fig. 5.24. This computation has been realized with a Gaussian smearing of 0.01 Ha.

The magnetic moments around the Cr atoms are given in Table 5.4. The localization around one of the Cr atoms is clear, but two holes should be localized and two Cr atoms should have a lower magnetic moment. This would be the case of a pure polaronic system. A possibility is that one of the holes is delocalized. Another indication of this phenomenon is the fact that four of the six Cr-O bond lengths around only one of the Cr atoms decrease from around 1.97 to 1.91 Å (the other two bonds keep the same length of 1.97 Å) : the O atoms are localized around only one of the Cr atoms like in the case of $x = 0.25$, and not around two of them. In order to determine precisely the behavior of this material, a study of the evolution of the structure with the smearing temperature should be realized : it is possible that 0.01 Ha is close to the transition temperature between the polaronic and the metallic $La_{0.50}Sr_{0.50}CrO_3$.

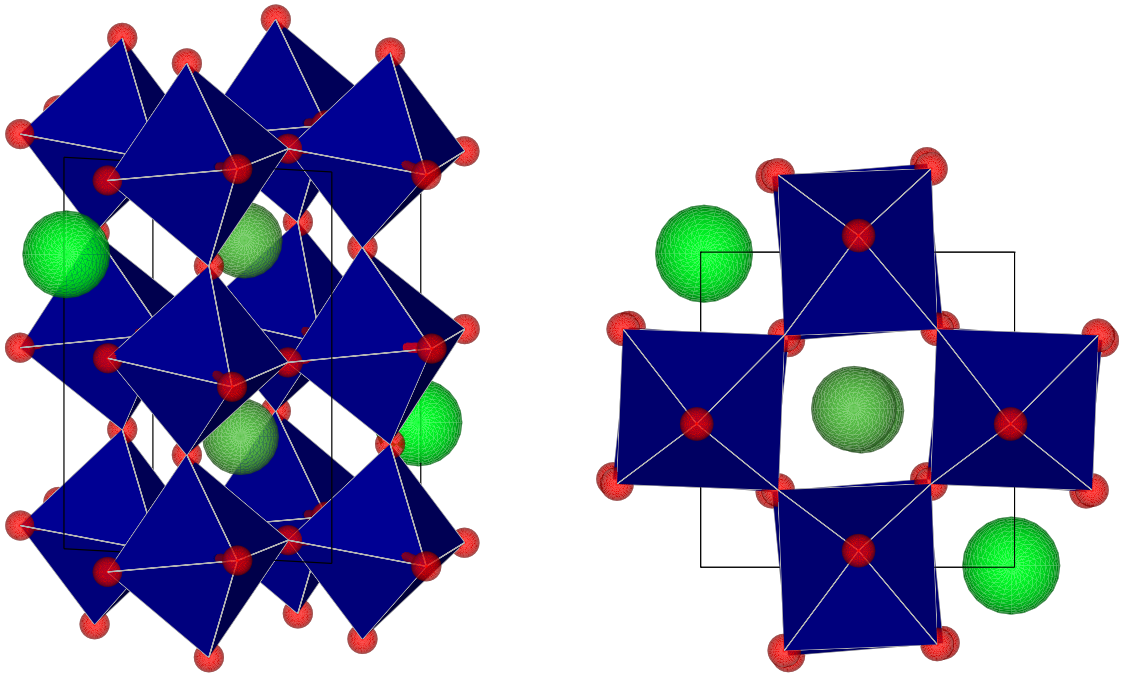

(a) (b)

Figure 5.24: (a) Computed unit cell of $La_{0.50}Sr_{0.50}CrO_3$. (b) View of the unit cell along the **c** axis. Dark green : La, light green : Sr, red : O.

Band structure

The band structure obtained for $La_{0.50}Sr_{0.50}CrO_3$ is represented in Fig. 5.25. In this case, two flat states appear inside the forbidden band, lying 0.37 and 1.74 eV above the valence band and with bandwidths of 0.13 and 0.19 eV. But there is also an unoccupied state at the top of the valence band, and the material is thus metallic. The system seems to be at a transition between the polaronic and the metallic states. In order to determine the actual behavior of this material, a complete study of its evolution with the smearing temperature should be realized.

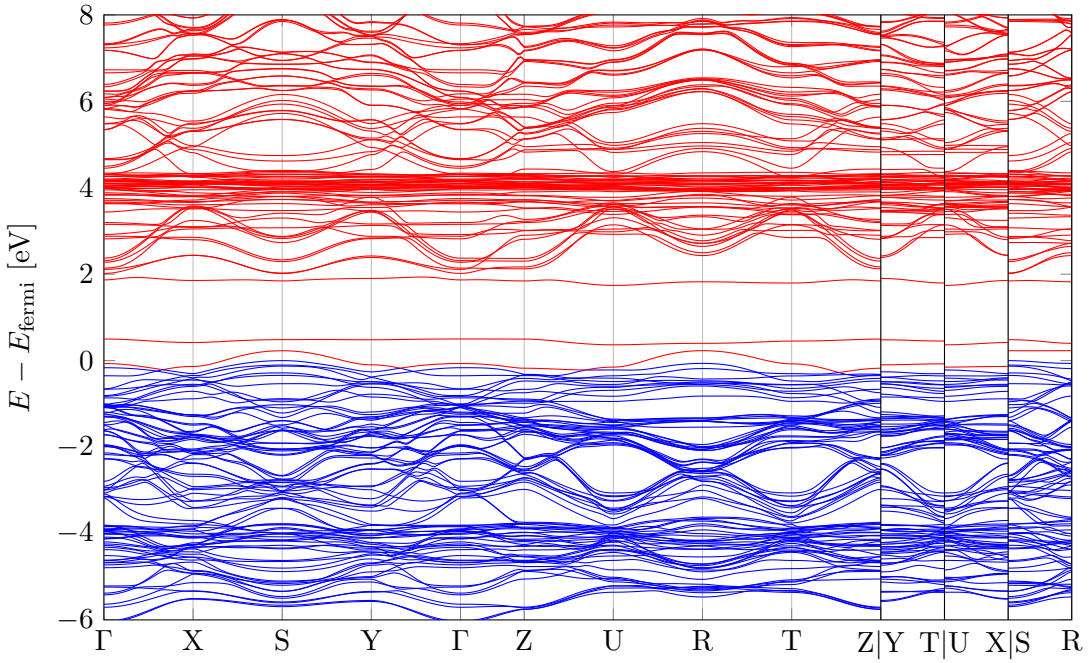

Figure 5.25: Band structure of $La_{0.50}Sr_{0.50}CrO_3$ computed with a smearing of 0.01 Ha. Blue states are occupied at $T = 0$ K, and red ones are not.

5.4.3 $La_{0.25}Sr_{0.75}CrO_3$

Crystal structure and magnetic properties

Only one structure with one unit cell has also been considered for $x = 0.75$. The atomic positions are given in Table E.4. The unit cell parameters are given in Table 5.2. In this case, the O atoms are more localized around 3 of the 4 Cr atoms : the lengths of 4 of the bonds decrease from 1.99 to 1.9 Å (the other 2 bonds keep the same length of 1.99 Å).

The magnetic moments around Cr atoms have been calculated and reported in Table 5.4. Three of them are in the Cr^{4+} states, characterized by the same magnetic moment as in $SrCrO_3$, while the last one has a magnetic moment corresponding to the Cr^{3+} state.

Band structure

Fig. 5.27 represents the band structure of $La_{0.25}Sr_{0.75}CrO_3$. Three levels are present in the forbidden band. The band is quite broad, and even goes under the Fermi energy. It has been reported by Zhang *et al.* that above $x = 0.65$, the material becomes metallic and the band conduction prevails [2].

Indeed, in the case of a lower fraction of Sr atoms, the Cr^{4+} atoms constituting the polarons do not interact so much with each other and the states associated to the localized holes are very flat (see Figs. 5.16 and 5.25). When there are more Cr^{4+}, they are closer to each other, and their interactions become important. The small polarons are then lost, the bands associated to holes around Cr^{4+} are more dispersive and the material begins to act like a metal. It is already the case for $x = 0.75$, as it can be seen in Fig. 5.27.

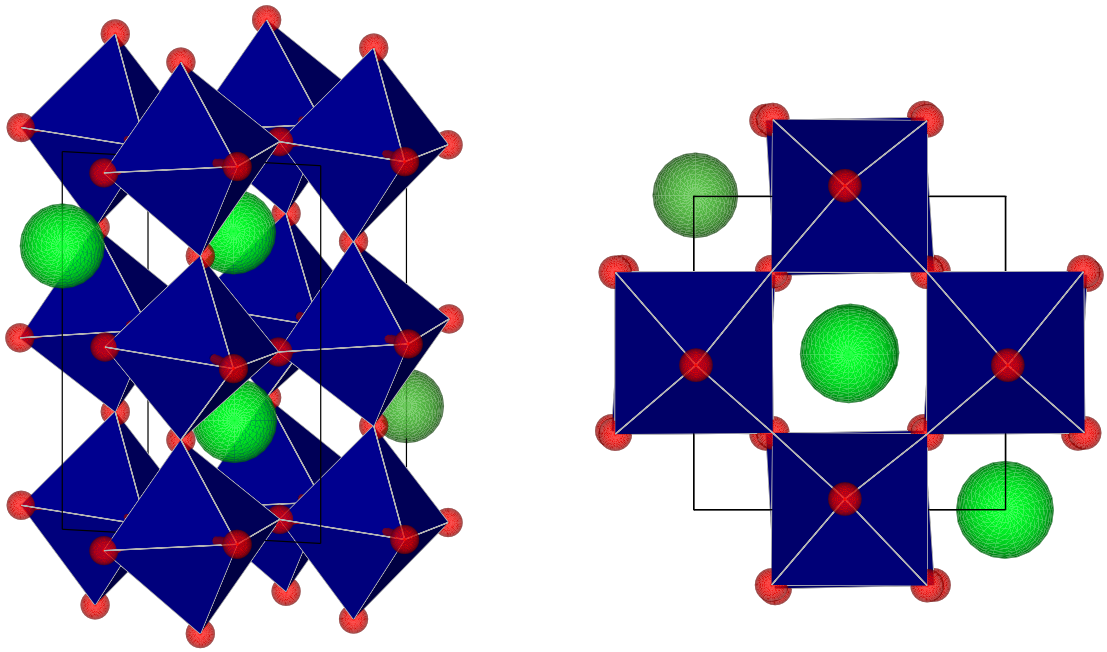

(a) (b)

Figure 5.26: (a) Computed unit cell of $La_{0.25}Sr_{0.75}CrO_3$. (b) View of the unit cell along the **c** axis. Dark green : La, light green : Sr, red : O.

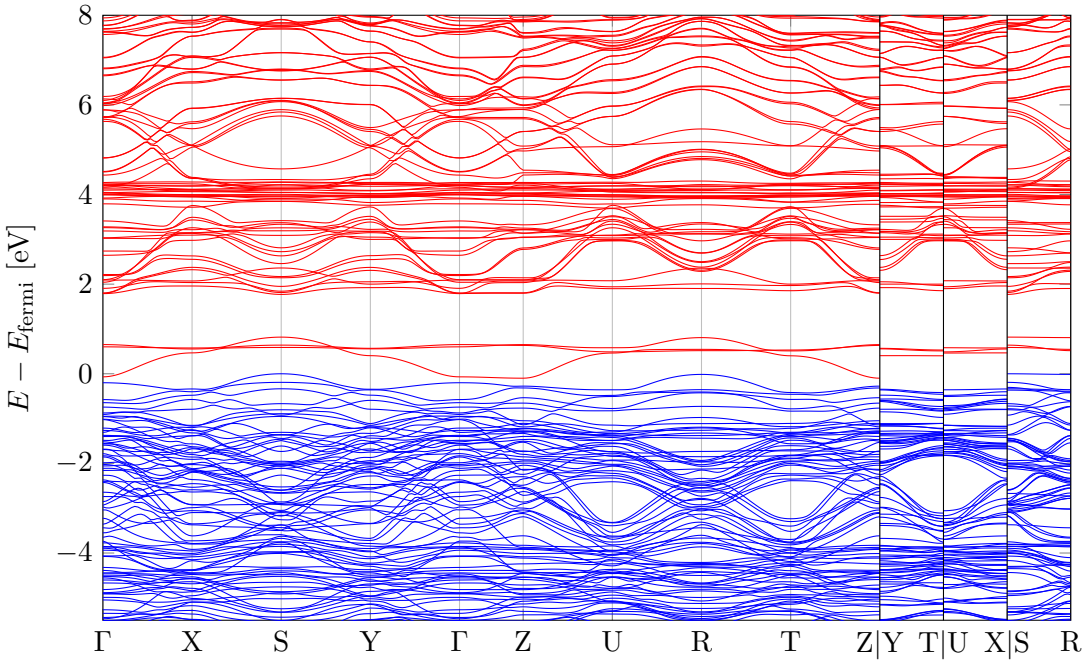

Figure 5.27: Band structure of $La_{0.25}Sr_{0.75}CrO_3$ computed with a smearing of 0.01 Ha. The material is metallic. Blue states are occupied at $T = 0$ K, and red ones are not.

5.5 $SrCrO_3$

The second boundary of $La_{1-x}Sr_xCrO_3$ is now analysed. The same steps as for $LaCrO_3$ are followed.

5.5.1 Crystal structure

The same kind of computation has been realized for $SrCrO_3$. Because the purpose is to be able to compare the results of the doped material with $LaCrO_3$ and $SrCrO_3$, the structure which has been chosen as the starting point of the structural relaxation is the relaxed structure of $LaCrO_3$. The relaxed structure could thus not be the most stable one. Indeed, at room-temperature, the measured space group is $Pm3m$ and the structure is cubic. Nevertheless, the most stable structure at low temperature has not yet been determined experimentally. A simple computation of the cubic structure with the same parameters has led to the conclusion that the orthorhombic structure is more stable : it lies 25 meV/at. below the cubic one. The unit cell parameters are given in Table 5.2 and cannot be compared to any experimental values. The structure is represented in Fig. 5.28, and the atomic positions are given in Table E.5. These computations have been realized with a smearing of 0.01 Ha (0.27 eV). In order to have an idea of the effect of the temperature on the occupation of $SrCrO_3$, and the effect of the broadening, the structure has also been computed using a larger smearing (corresponding to 0.04 Ha). Fig. 5.29 compares the two structures as seen along the **c** axis. It can be seen that the octahedra around Cr atoms are slightly distorted when the smearing is small compared to the situation with a larger smearing. Table 5.5 compares the Cr-O bond lengths for the two smearing temperatures.

5.5.2 Magnetic properties

Again, the magnetic moment around each Cr atom has been computed. In $SrCrO_3$, all the Cr atoms are in the Cr^{4+} state, and the magnetic moment should therefore be around $\pm 2\mu_B$ on each one of them. The approximate value of $\pm 1.9\mu_B$ has been obtained and reported in Table 5.4. The ferromagnetic structure has also been computed, and is less energetically favourable than the antiferromagnetic one, as expected from experiments.

Table 5.5: Computed Cr-O_i bond lengths in a $SrCrO_3$ octahedron.

	$T_{\text{smearing}} = 0.01$ Ha	$T_{\text{smearing}} = 0.04$ Ha	Δ [%]
Cr-O_1 [Å]	1.89273	1.94105	2.49
Cr-O_2 [Å]	1.89273	1.94105	2.49
Cr-O_3 [Å]	1.99472	1.94105	−2.7
Cr-O_4 [Å]	1.99472	1.94105	−2.7
Cr-O_5 [Å]	1.90670	1.94090	1.77
Cr-O_6 [Å]	1.90670	1.94090	1.77

5.5.3 Band structure

The band structure has also been computed for $SrCrO_3$. First, the small smearing (0.01 Ha) has been used. The result is given in Fig. 5.30. It can be observed on this band structure that four flat states appear in the forbidden band. An analysis of the nature of these states indicates that they correspond mainly to d orbitals of Cr atoms (see Fig. 5.33). That means that each Cr atom has localized a hole. The band constituted by these localized states lies 0.65 eV above the valence band and its bandwidth is of 0.1 eV. It is however difficult to characterize the transport in $SrCrO_3$ with small polarons, because in this case each Cr atom has a localized hole. The material is insulating.

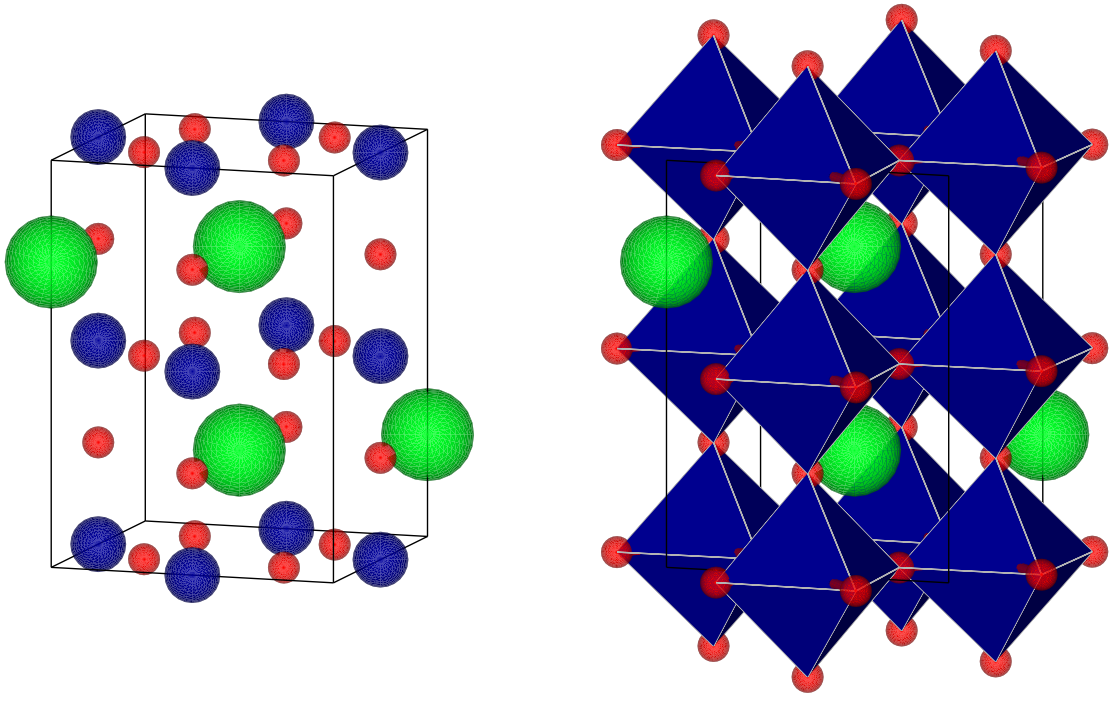

(a) (b)

Figure 5.28: (a) Computed unit cell of $SrCrO_3$. (b) Representation of the octahedra around Cr atoms. Light green : Sr, blue : Cr, red : O.

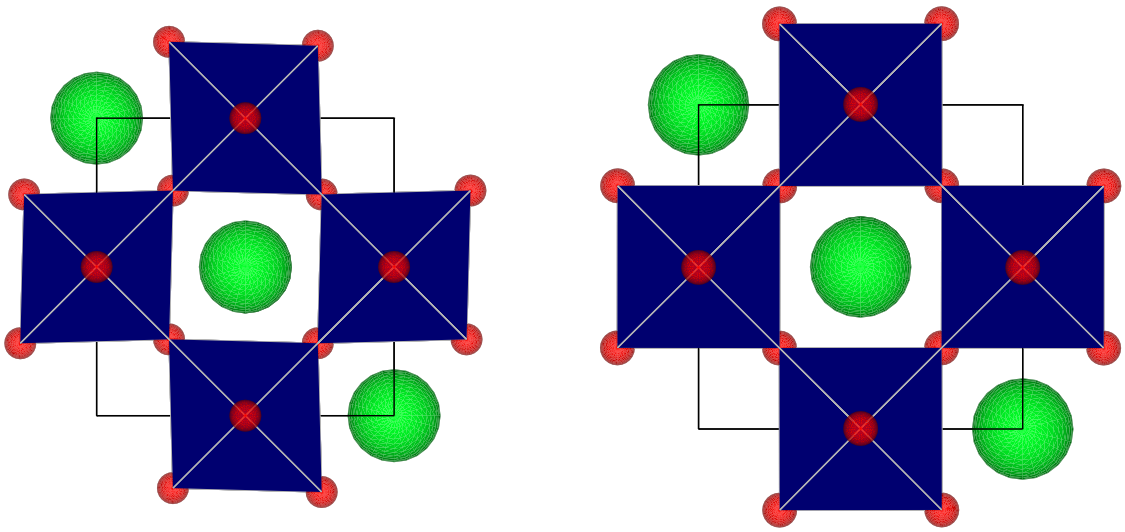

(a) (b)

Figure 5.29: View of the unit cell of $SrCrO_3$ along the **c** axis for (a) a smearing of 0.01 Ha and (b) a smearing of 0.04 Ha. Light green : Sr, red : O.

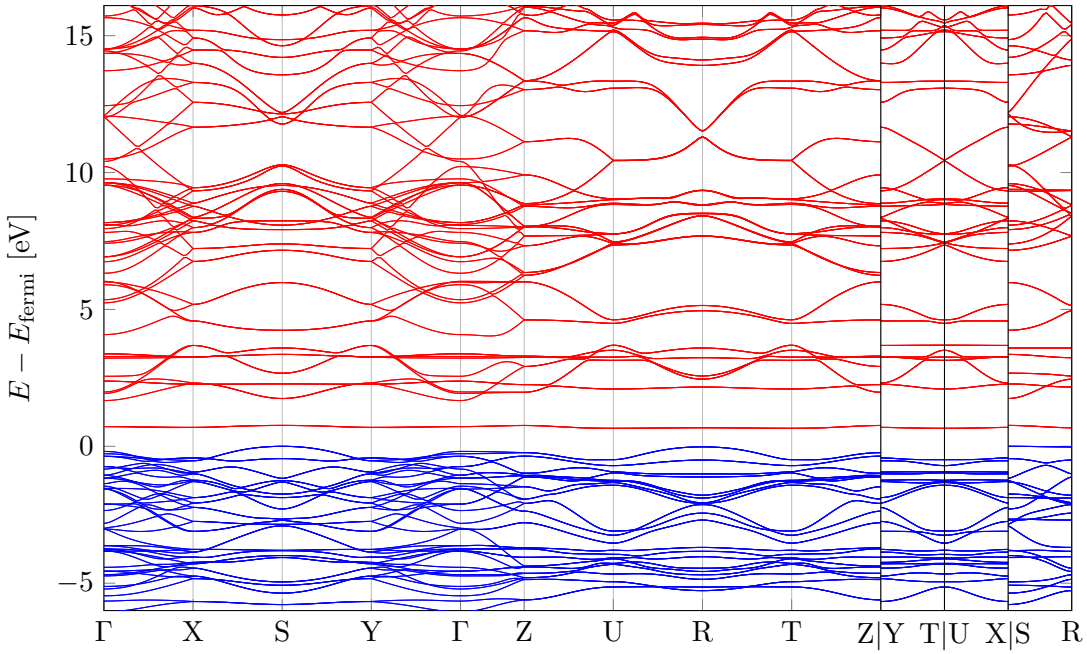

Figure 5.30: Band structure of antiferromagnetic $SrCrO_3$ computed with a smearing of 0.01 Ha. Blue states are occupied at $T = 0$ K, and red ones are not.

The band structure has also been computed with the larger smearing (0.04 Ha) and is represented in Fig. 5.31. With this smearing, the states in the forbidden band disappear and the material becomes metallic. Like in the case of $La_{0.75}Sr_{0.25}CrO_3$, it is the structure obtained with the smaller smearing that is at the origin of the localization : the computation of the band structure with a smearing of 0.01 Ha but using the crystal structure obtained with the smearing of 0.04 Ha showed that there are no states in the forbidden band.

5.5.4 Density of states

The important results for the insulating material are represented in Figs. 5.32 and 5.33. The states appearing in the middle of the forbidden band mainly correspond to d orbitals of Cr atoms. This situation is similar to the one described for $La_{0.75}Sr_{0.25}CrO_3$. However, in this case, all the Cr atoms are in the Cr^{4+} state, as represented in Fig. 5.22. The contribution of the O p orbitals is also not negligible in this band.

The results for the metallic $SrCrO_3$ are represented in Figs. 5.34 and 5.35. In this case, the Cr d orbitals contain holes which are delocalized over the crystal.

5.5.5 Difference of energy between the insulating and the metallic states

As in the case of $La_{0.75}Sr_{0.25}CrO_3$, both insulating and metallic states of $SrCrO_3$ have been found. However, in this case, the insulating material is less stable than the metallic one. Indeed, Cr^{4+} atoms interact with each other and tend to a metallic behavior : this structure is more stable by 43 meV. This confirms the metallic evolution of the resistivity measured by Zhang *et al.* Experiments showed that for $x > 0.65$, the material becomes metallic. This indicates that the relative position of the mean energies before and after the transition temperature could depend on the value of x : there would be a x^* (supposably close to 0.65) under which the insulating state would be energetically favourable compared to the metallic one, because the holes would be localized on the Cr atoms and the interaction between these Cr^{4+} ions would not be too important. Above x^*, the opposite would be true. In order to assess this hypothesis, the difference of energy between the insulating (or polaronic) state and the metallic one should be

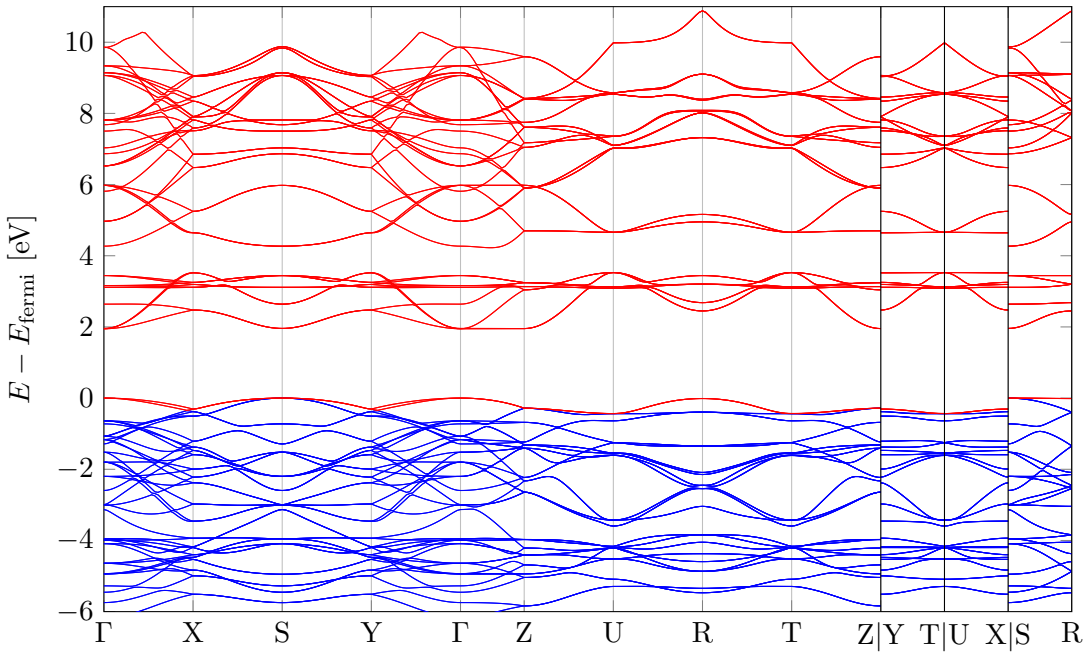

Figure 5.31: Band structure of antiferromagnetic $SrCrO_3$ computed with a smearing of 0.04 Ha. Blue states are occupied at $T = 0$ K, and red ones are not.

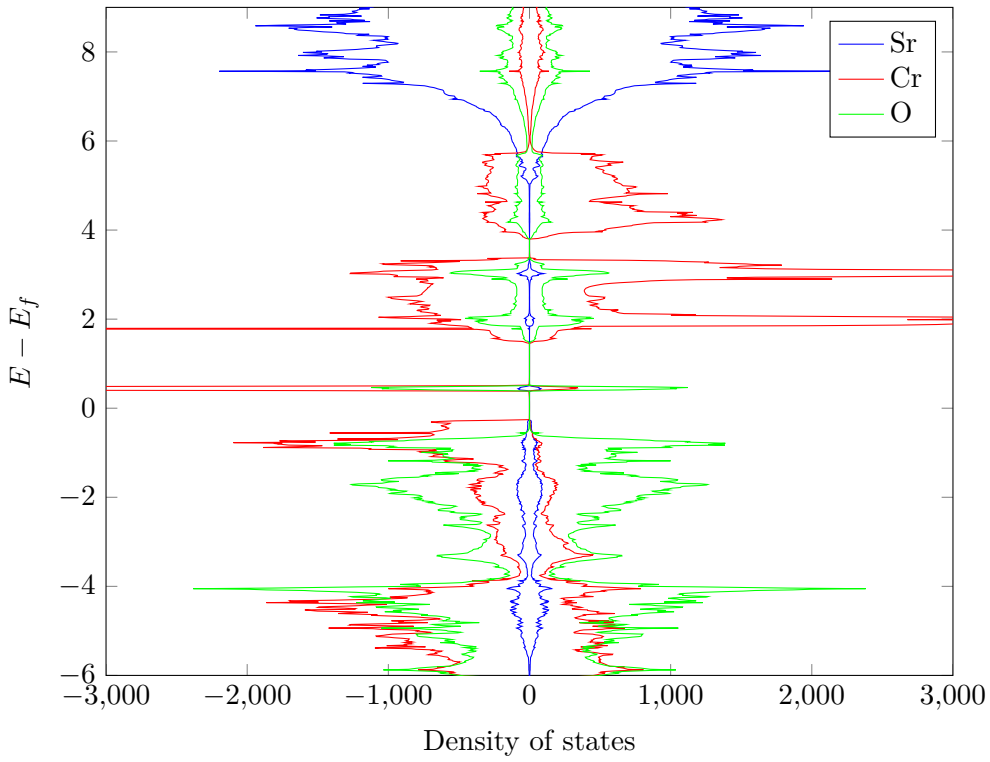

Figure 5.32: Comparison between the sum of the projections of the DOS on atomic orbitals around the atoms in insulating $SrCrO_3$.

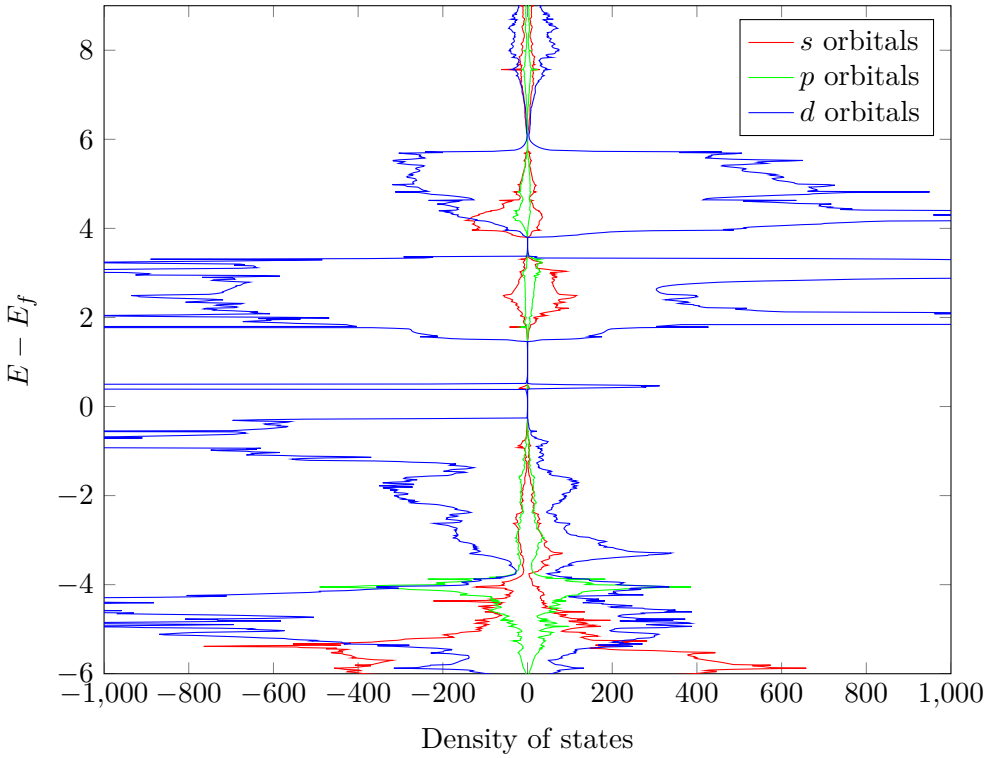

Figure 5.33: Comparison between the projections of the DOS on atomic orbitals around a Cr atom in insulating $SrCrO_3$.

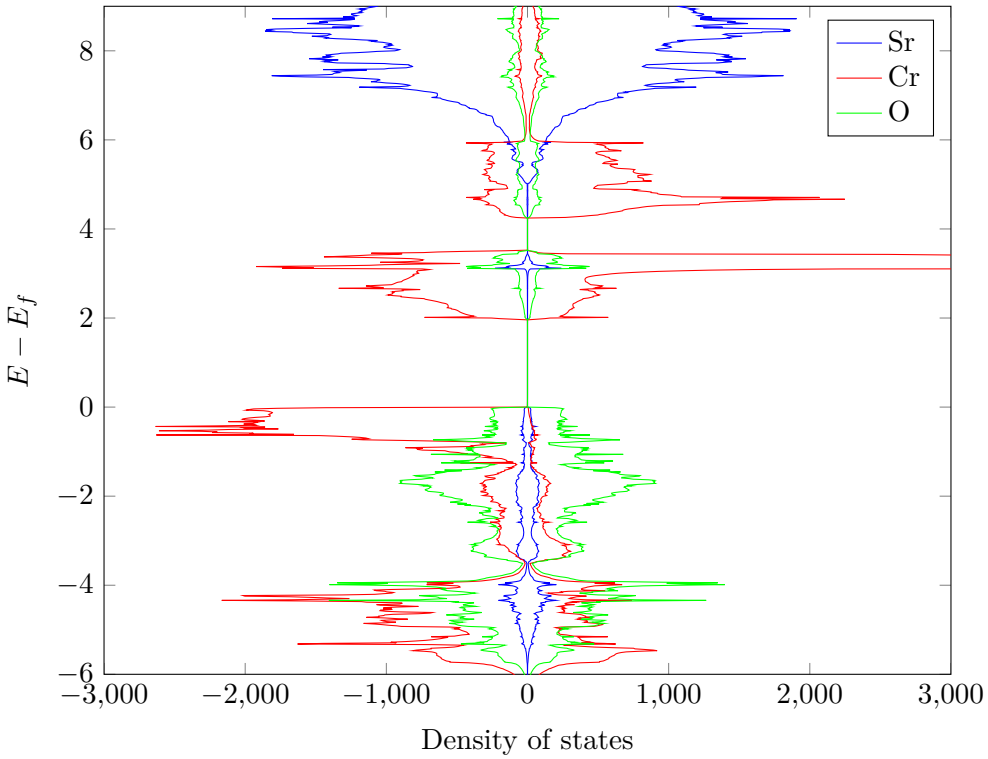

Figure 5.34: Comparison between the sum of the projections of the DOS on atomic orbitals around the atoms in metallic $SrCrO_3$.

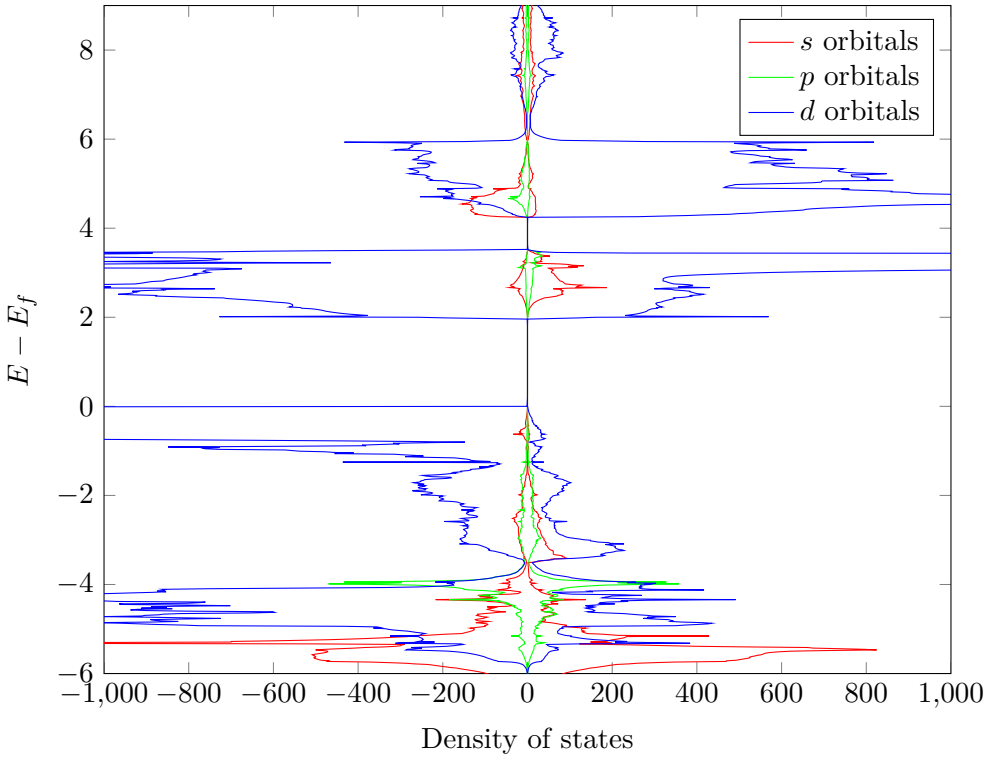

Figure 5.35: Comparison between the projections of the DOS on atomic orbitals around a Cr atom in metallic $SrCrO_3$.

computed for many different values of x. This means that for each case, the study of the energy and magnetic moments as functions of the smearing temperature should be realized. This is a long work which has not been realized for this dissertation, but should be in order to completely characterize $La_{1-x}Sr_xCrO_3$.

5.6 Formation energies

The formation energy $E_f(x)$ of $La_{1-x}Sr_xCrO_3$ as a function of x can be written as

$$E_f(x) = E(x) - xE(x=1) - (1-x)E(x=0) \tag{5.1}$$

where E is the total energy of the compound computed with ABINIT. $E(x=0)$ is the energy of the insulating $LaCrO_3$ and $E(x=1)$ is the energy of the metallic $SrCrO_3$, this state being the most stable one. The formation energy is represented in Fig. 5.36. As it can be seen, the formation energy is quite small (it is never greater than 100 meV), and would actually be strictly equal to zero if the relationship $E(x)$ was exactly linear. These low values indicate that the miscibility of this alloy is high. Indeed, Table 5.2 and Figs. 5.2 and 5.28 show that the structures of $LaCrO_3$ and $SrCrO_3$ are quite similar, and it does not change too much when Sr atoms replace La ones, even when polarons are formed. The energy of the cubic $SrCrO_3$ has also been computed and represented. It can be seen that this system is much less stable than the orthorhombic one.

5.7 Optical properties

In this section, the absorption coefficient of $LaCrO_3$ is presented. In order to do so, the frequency dependent linear optical dielectric tensor has been computed using the Optic utility of the

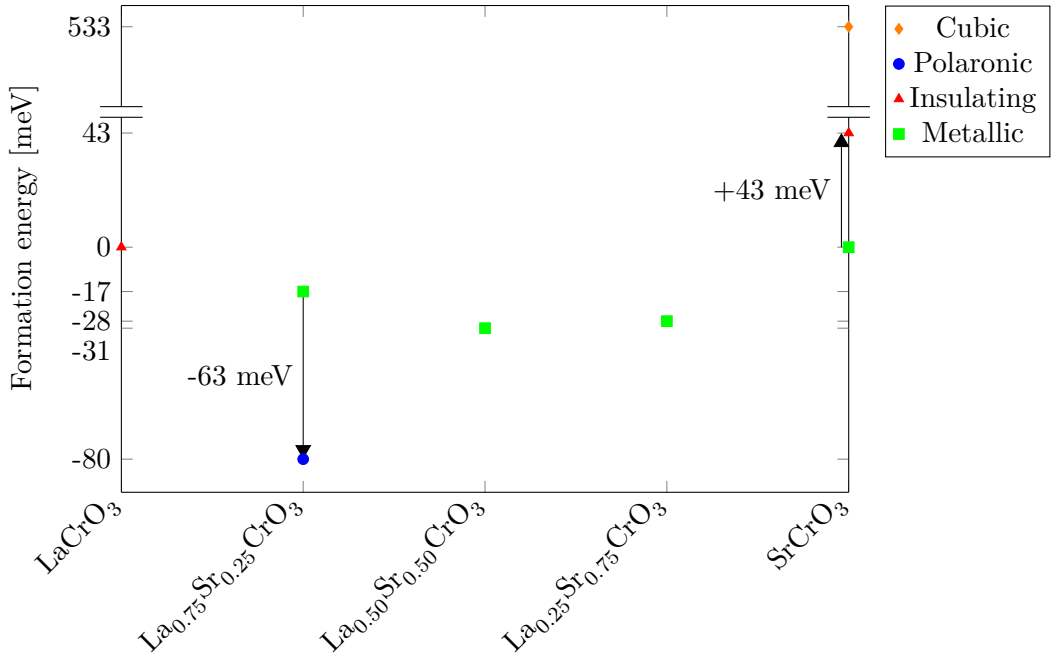

Figure 5.36: Formation energy of $La_{1-x}Sr_xCrO_3$ as a function of x.

ABINIT package. First, the theoretical background behind this utility is introduced. The results are then presented.

5.7.1 First order dielectric tensor from first principles

The purpose is to measure the response of a material to incoming light. This will be realized using the frequency components $\mathbf{X}(\omega)$ of the different fields $\mathbf{X}$ with the definition [40]

$$\mathbf{X}(t) = \sum_n \mathbf{X}(\omega_n) \exp(-i\omega_n t) \tag{5.2}$$

where the summation covers positive and negative frequencies ω_n. The electric field associated to the incoming light polarizes the material. This polarization can be written as

$$\mathbf{P}^a(\omega) = \chi^{(1)}_{ab}\mathbf{E}^b(\omega) + \chi^{(2)}_{abc}\mathbf{E}^b(\omega)\mathbf{E}^c(\omega) + \dots \tag{5.3}$$

where $\mathbf{P}^a(\omega)$ is the a component of the polarizability, $\chi^{(1)}_{ab}$ is the ab component of the first order electric susceptibility and $\chi^{(2)}$ is the second order susceptibility. The Einstein convention is adopted for the subscripts : they are to be summed if repeated.

Optic is able to compute both susceptibilities from first principles, but only the linear one will be considered here. It may be shown that (see Ref. [41] for the details of the demonstration)

$$\chi^{(1)}_{ab}(\omega) = \frac{e^2}{\hbar\Omega}\sum_{nm\mathbf{k}} f_{nm}(\mathbf{k})\frac{\mathbf{r}^a_{nm}(\mathbf{k})\mathbf{r}^b_{mn}(\mathbf{k})}{\omega_{mn}(\mathbf{k}) - \omega} \tag{5.4}$$

where Ω is the volume of the Brillouin zone, n and m are electronic states, $\mathbf{k}$ is the wave vector inside the Brillouin zone, $\hbar\omega_{mn} = \hbar\omega_m - \hbar\omega_n$, $f_{nm}(\mathbf{k}) = f_n(\mathbf{k}) - f_m(\mathbf{k})$ with f the Fermi-Dirac occupation function, and $\mathbf{r}^a_{nm}(\mathbf{k})$ are the position matrix elements. These are given by

$$\begin{array}{lcll} \mathbf{r}^a_{nm}(\mathbf{k}) & = & \frac{\mathbf{V}^a_{mn}(\mathbf{k},t)}{i\omega_{mn}} & \text{if } \omega_{mn} \neq 0 \\ \mathbf{r}^a_{nm}(\mathbf{k}) & = & 0 & \text{if } \omega_{mn} = 0 \end{array} \tag{5.5}$$

with

$$\mathbf{V}^a_{mn} = \frac{\mathbf{p}^a_{mn}}{m}, \tag{5.6}$$

p being the momentum matrix elements and m the mass of the free electron.

Moreover,

$$\chi^{(1)}_{ab}(\omega) = \frac{\epsilon_{ab}(\omega) - \delta_{ab}}{4\pi} \tag{5.7}$$

where ϵ_{ab} is the ab component of the dielectric tensor. In order to determine the relative permittivity with Optic, it is first necessary to determine the ground state wavefunction and the matrix elements of the position operator (via the derivative with respect to **k**, see Ref. [42] for more details). This first step is realized with ABINIT. Eq. (5.4) is then solved by Optic.

5.7.2 Absorption coefficient

Once the relative permittivity is known in each direction, it is possible to derive the absorption coefficient of the material. The following equations rely on Ref. [9]. Only the diagonal components of the tensors will be considered here ($a = b$). The relative permittivity is

$$\epsilon_{aa} = \Re(\epsilon_{aa}) + i\Im(\epsilon_{aa}) = \tilde{n}^2_{aa} \tag{5.8}$$

where $\tilde{n}_{aa}$ is the complex refraction coefficient in the aa direction. This coefficient can be decomposed as

$$\tilde{n}_{aa} = n_{aa} + i\kappa_{aa} \tag{5.9}$$

where n is the normal refraction index and κ is the absorption coefficient. These equations lead to

$$n_{aa} = \sqrt{\frac{\Re(\epsilon_{aa}) + \sqrt{\Re(\epsilon_{aa})^2 + \Im(\epsilon_{aa})^2}}{2}} \tag{5.10}$$

$$\kappa_{aa} = \sqrt{\frac{-\Re(\epsilon_{aa}) + \sqrt{\Re(\epsilon_{aa})^2 + \Im(\epsilon_{aa})^2}}{2}}. \tag{5.11}$$

At normal incidence, the reflectance R is

$$R_{aa} = \frac{(n_{aa} - 1)^2 + \kappa^2_{aa}}{(n_{aa} + 1)^2 + \kappa^2_{aa}} \tag{5.12}$$

and the transmittance T is

$$T_{aa} = 1 - R_{aa}. \tag{5.13}$$

The xx, yy and zz components of the absorption have been computed. The absorption coefficient spectrum of $LaCrO_3$ is represented in Fig. 5.37 and its transmittance is depicted in Fig. 5.38. It can be seen that the maximal transmittance is higher than what has been reported by Zhang *et al.* This could be due to the fact that their measure took into account the contribution of the substrate.

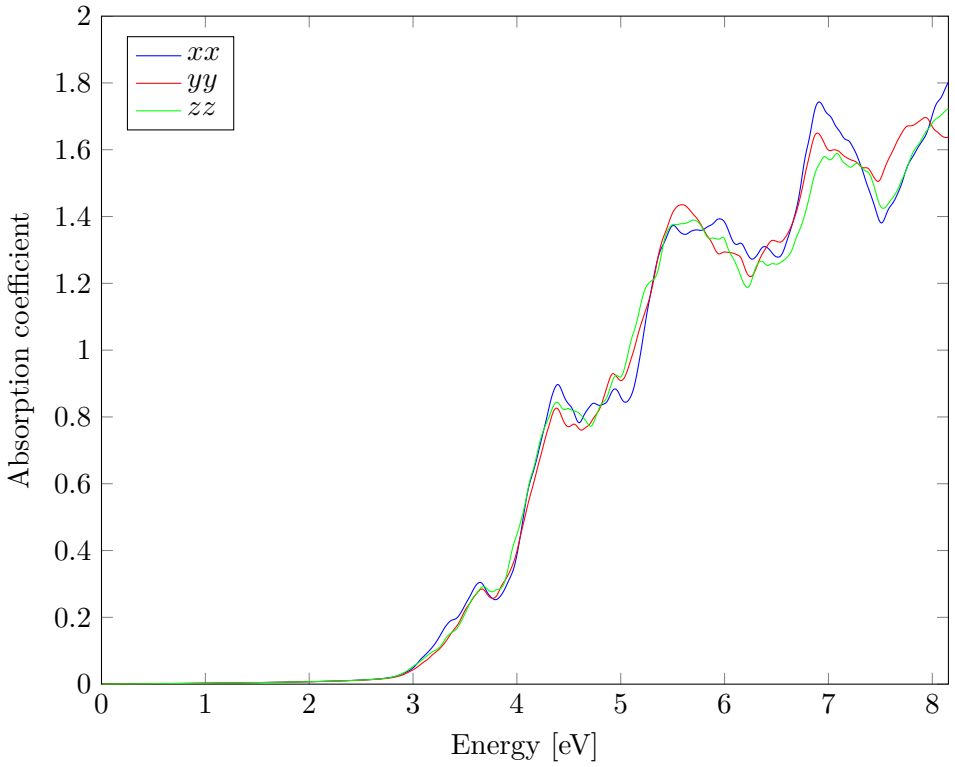

Figure 5.37: Computed absorption spectrum of $LaCrO_3$ along the three principal directions.

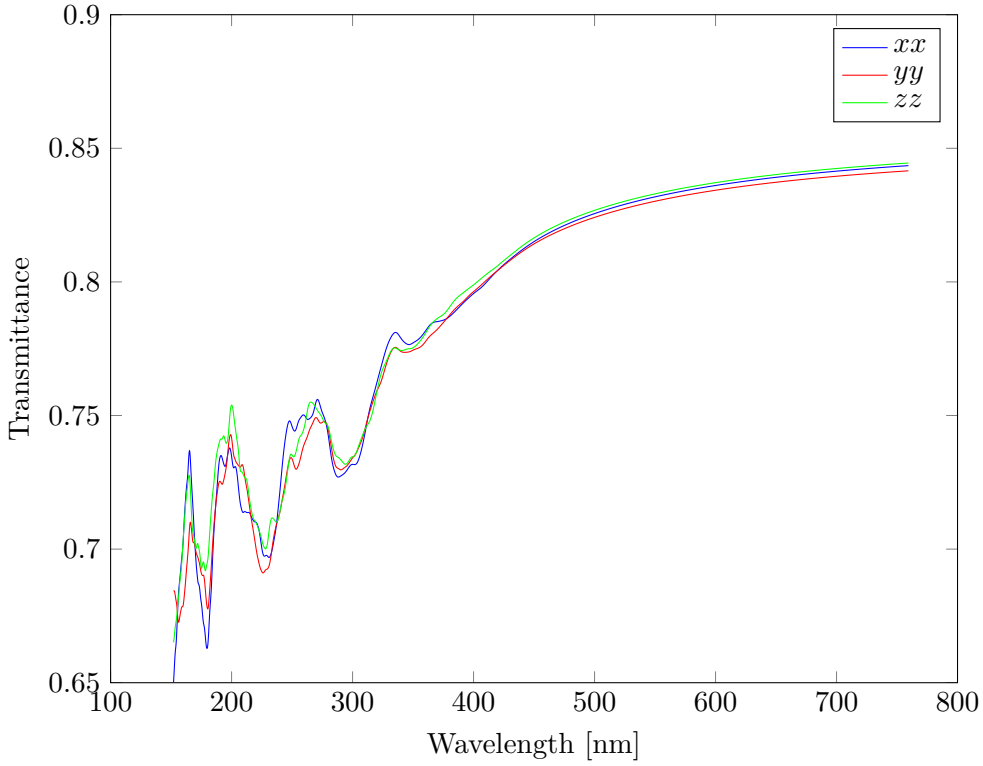

Figure 5.38: Computed transmittance of $LaCrO_3$ along the three principal directions.

5.8 Conclusion

It is now possible to summarize the *ab initio* results obtained for $La_{1-x}Sr_xCrO_3$.

The crystal structure of $LaCrO_3$ has been confirmed to be a distorted perovskite. The computed cell parameters are in good agreement with experiment (within 2%). The antiferromagnetic ordering is indeed preferred compared to the ferromagnetic one : the magnetic moments around the Cr atoms cancel each other in a *G*-type configuration. The values of these magnetic moment approximately correspond to what was expected of the Cr^{3+} ions : they have a magnetic moment of $\pm 2.7\mu_B$. The experimental band gap of 2.8 eV has been obtained by choosing $U = 2.85$ eV. At the band gap, the transition happens mainly between Cr d orbitals hybridized with a little bit of O p orbitals. All these computations have been realized with a Gaussian smearing of 0.01 Ha (= 0.27 eV) of the occupation function.

The same computations have been realized for $x = 0.25$, $x = 0.50$ and $x = 0.75$. It has been observed that with the same parameters as for $LaCrO_3$, the polaronic state is not found in the case of $x = 0.25$. The use of VASP and the tetrahedron method allowed to understand that the used smearing of 0.01 Ha was too large, and the material was metallic. A transition is indeed observed in the evolution of the magnetic moments around Cr atoms with the used smearing. For very low smearing temperatures, the polaronic state is found : one of the Cr is in the Cr^{4+} state, and the other three are in the Cr^{3+} state. Above a certain smearing temperature, all magnetic moments have a same average value : the four Cr atoms are in a sort of $Cr^{3.25}$ state. The determination of this transition temperature would be possible by computing the crystal structures for many smearing temperatures with a Fermi-Dirac distribution. Both crystal structures have been computed, and it can be seen that the O atoms are more localized around one of the Cr atoms in the case of the polaronic material. One of the four holes is localized around one of the Cr atoms, constituting the polaron. In the metallic material, this hole is delocalized over the four Cr atoms. The energy associated to the transition from the polaronic to the non-polaronic material has been roughly computed. The value of 63 meV has been obtained, the polaronic state being lower in energy than the metallic one.

In the case of $x = 0.50$, a mix between the polaronic state and the metallic state has been found with a smearing of 0.01 Ha. In this case, two states appear at different positions in the forbidden band. Only one Cr atom is in the Cr^{4+} state and the material is metallic as well. But these conclusions should be carefully considered, and calculations with smaller and higher smearing temperatures should be realized.

The case of $x = 0.75$ has also been considered. Three of the four Cr atoms are in the Cr^{4+} states while the last one is in the Cr^{3+} state. The O atoms around these three Cr atoms are more localized than around the other one. Three states appear in the forbidden band, and the bandwidth is quite large. The band constituted by these states even goes slightly under the Fermi level, which makes of this material a metal. This is due to the higher interactions between the Cr^{4+} atoms, which are closer in this material. It is expected that there is a fraction x^* above which the material becomes preferably a metal compared to polaronic. This hypothesis should be verified with a deeper analysis of $La_{1-x}Sr_xCrO_3$ for many different values of x. If this is the case, the value of x^* could be determined by considering supercells in order to model different structures close to $x = 0.65$ (experimental value of x^*).

$SrCrO_3$ has also been characterized. The obtained crystal structure is a perovskite too, but not a cubic one as it has been measured at room temperature. The computation of the ground state of this cubic structure showed that it is higher in energy at low temperature, but it still has to be confirmed experimentally. It has been observed that in the case of the small smearing, a band appears in the forbidden band and the material is insulating. This band disappears when the smearing is large, and the material becomes metallic. The crystal structure changes too when the smearing increases : the O atoms are more localized around the Cr atoms in the case of the small smearing. The crystal is also antiferromagnetic, and the magnetic moments around the Cr^{4+} are around $1.9\mu_B$. An analysis of the projected density of states led to the

conclusion that the states inside the forbidden band of the insulating material are mainly of Cr d character, again hybridized with a little bit of O p orbitals. That shows that the holes are localized around the Cr atoms. In the case of the metallic material, the holes are delocalized over the crystal. A comparison between the mean energies of the two states of $SrCrO_3$ led to the conclusion that the metallic state is more stable than the insulating one : the former lies 43 meV under the latter. Indeed, experiments show that $SrCrO_3$ is a metal.

The formation energy of the different structures has been defined and computed as well. In all cases, it is quite small, which indicates that the stabilization of the structures is possible. Finally, the absorption coefficient and the transmittance of $LaCrO_3$ have been computed. These computations have not been realized for the other structures, but could be in order to see the influence of the polaronic bands on the absorption spectra. It would then be possible to compare these spectra with the results obtained by Zhang *et al.* for $La_{1-x}Sr_xCrO_3$.

Conclusion

The continuing search for new efficient p-type TCOs led to the finding of $La_{1-x}Sr_xCrO_3$, which has been experimentally characterized by Zhang *et al.* The material showed interesting properties that needed to be investigated in order to determine their origins. This is what has been realized in this dissertation : *ab initio* computations have been carried out on $LaCrO_3$, $SrCrO_3$, and three different Sr fraction ($x = 0.25$, $x = 0.50$ and $x = 0.75$). The ABINIT package has been mainly used, but the VASP code has also been useful in the case of $x = 0.25$.

From the experimental behavior of the electrical conductivity, small polarons were expected to be found in the materials with $0 < x < 0.65$. These polarons have been identified by different factors : the magnetic moment around a Cr atom decreases to the value found in $SrCrO_3$ when it has a localized hole, the O atoms of the octahedron come closer to this Cr atom, and a localized state appear in the forbidden band, with the corresponding hole density localized around the same Cr atom. It has been observed that there is a transition from the polaronic state to the metallic one with the smearing temperature used for the occupation : there is a temperature T^* for above which the material is metallic rather than insulating. This temperature could be determined if the Fermi-Dirac distribution was used. In the case of $x = 0.25$, it has been possible to approximate the difference of energy between the two states of the material to about 63 meV : the polaronic state is more stable than the metallic one. In the case of $x = 0.75$, the material found is metallic. In the case of $SrCrO_3$, it has been possible to determine that the difference of energy between the insulating and the metallic state is approximately of 43 meV : the metallic state is in this case more stable, as opposed to the case of $x = 0.25$. This leads to a hypothesis : there exists a fraction of Sr x^* above which the metallic state is lower in energy than the insulating (or polaronic) one. This idea also comes from the fact that when x increases, the interactions between the Cr^{4+} ions also increase, and the polarons are therefore harder to form (a polaron is in principle isolated from the other polarons in a system). In order to test this hypothesis, many different structures for many values of x should be considered. The evolution of the energy with the smearing should be realized for each one of them.

$La_{1-x}Sr_xCrO_3$ is thus very interesting from the p-type TCO point of view. Indeed, despite the very low hole effective mass due to the small-polaron hopping, it has a high conductivity thanks to the very high extents of the doping levels achieved. A small-polaron system has another advantage compared to usual TCOs : the lower bound in the frequency window for the transmittance does not vary too much with the carrier concentration, like it is the case with the plasma frequency. However, the doping level x^* should not be reached : indeed, above this value, the material becomes metallic and reflects light. This is obviously not wanted in a TCO application.

The study of this system should not stop here, as it has already been mentioned many times. The transition with the smearing temperature should be studied with adapted k-points grids for each values of x. The optical properties should be studied for these fractions of Sr atoms. In order to consider more values of x, supercells would have to be used, which would increase the computation time. These studies would allow a more precise characterization of the $La_{1-x}Sr_xCrO_3$ system, and maybe lead to a new design rule for the development of future p-type TCOs.

Bibliography

[1] K. H. Zhang, Y. Du, A. Papadogianni, O. Bierwagen, S. Sallis, L. F. Piper, M. E. Bowden, V. Shutthanandan, P. V. Sushko, and S. A. Chambers, "Perovskite Sr-Doped $LaCrO_3$ as a New p-Type Transparent Conducting Oxide," *Advanced Materials*, vol. 27, no. 35, pp. 5191–5195, 2015.

[2] K. Zhang, Y. Du, P. Sushko, M. E. Bowden, V. Shutthanandan, S. Sallis, L. F. Piper, and S. A. Chambers, "Hole-induced insulator-to-metal transition in $La_{1-x}Sr_xCrO_3$ epitaxial films," *Physical Review B*, vol. 91, no. 15, p. 155129, 2015.

[3] H. Liu, V. Avrutin, N. Izyumskaya, Ü. Özgür, and H. Morkoç, "Transparent conducting oxides for electrode applications in light emitting and absorbing devices," *Superlattices and Microstructures*, vol. 48, no. 5, pp. 458–484, 2010.

[4] S. Sohn and H.-m. Kim, "Transparent Conductive Oxide (TCO) Films for Organic Light Emissive Devices (OLEDs)," 2011.

[5] T. J. Coutts, T. O. Mason, J. Perkins, and D. S. Ginley, "Transparent conducting oxides: status and opportunities in basic research," in *Photovoltaics for the 21st Century: Proceedings of the International Symposium*, pp. 274–286, The Electrochemical Society: Philadelphia, PA, USA, 1999.

[6] G. Hautier, A. Miglio, G. Ceder, G.-M. Rignanese, and X. Gonze, "Identification and design principles of low hole effective mass p-type transparent conducting oxides," *Nature communications*, vol. 4, 2013.

[7] H. Ohta and H. Hosono, "Transparent oxide optoelectronics," *Materials Today*, vol. 7, no. 6, pp. 42–51, 2004.

[8] J. E. Medvedeva, "Combining optical transparency with electrical conductivity: Challenges and prospects," *Transparent Electronics: From Synthesis to Applications*, p. 29, 2010.

[9] X. Gonze, *LMAPR2014 - Physics of functional materials*, 2014–2015.

[10] V. Avrutin, N. Izyumskaya, and H. Morkoç, "Semiconductor solar cells: Recent progress in terrestrial applications," *Superlattices and Microstructures*, vol. 49, no. 4, pp. 337–364, 2011.

[11] J.-H. Lim, D.-K. Hwang, H.-S. Kim, J.-Y. Oh, J.-H. Yang, R. Navamathavan, and S.-J. Park, "Low-resistivity and transparent indium-oxide-doped ZnO ohmic contact to p-type GaN," *Applied physics letters*, vol. 85, no. 25, pp. 6191–6193, 2004.

[12] A. Facchetti and T. Marks, *Transparent electronics: from synthesis to applications*. John Wiley & Sons, 2010.

[13] M. Tseggai, P. Nordblad, R. Tellgren, H. Rundlöf, G. Andrè, and F. Bourèe, "Synthesis, nuclear structure, and magnetic properties of $LaCr_{1-y}Mn_yO_3$ ($y = 0, 0.1, 0.2$, and 0.3)," *Journal of Alloys and Compounds*, vol. 457, no. 1, pp. 532–540, 2008.

[14] T. Hashimoto, N. Tsuzuki, A. Kishi, K. Takagi, K. Tsuda, M. Tanaka, K. Oikawa, T. Kamiyama, K. Yoshida, H. Tagawa, *et al.*, "Analysis of crystal structure and phase transition of $LaCrO_3$ by various diffraction measurements," *Solid State Ionics*, vol. 132, no. 3, pp. 181–188, 2000.

[15] S. Gražulis, A. Daškevič, A. Merkys, D. Chateigner, L. Lutterotti, M. Quiró, N. R. Serebryanaya, P. Moeck, R. T. Downs, and A. Le Bail, "Crystallography Open Database (COD): an open-access collection of crystal structures and platform for world-wide collaboration," *Nucleic Acids Research*, vol. 40, no. D1, pp. D420–D427, 2012.

[16] S. Gražulis, D. Chateigner, R. T. Downs, A. F. T. Yokochi, M. Quirós, L. Lutterotti, E. Manakova, J. Butkus, P. Moeck, and A. Le Bail, "Crystallography Open Database – an open-access collection of crystal structures," *Journal of Applied Crystallography*, vol. 42, pp. 726–729, Aug 2009.

[17] R. T. Downs and M. Hall-Wallace, "The American Mineralogist Crystal Structure Database," *American Mineralogist*, vol. 88, pp. 247–250, 2003.

[18] K. Maiti and D. Sarma, " Electronic structure of $La_{1-x}Sr_xCrO_3$," *Physical Review B*, vol. 54, no. 11, p. 7816, 1996.

[19] V. Nithya, R. J. Immanuel, S. Senthilkumar, C. Sanjeeviraja, I. Perelshtein, D. Zitoun, and R. K. Selvan, "Studies on the structural, electrical and magnetic properties of $LaCrO_3$, $LaCr_{0.5}Cu_{0.5}O_3$ and $LaCr_{0.5}Fe_{0.5}O_3$ by sol–gel method," *Materials Research Bulletin*, vol. 47, no. 8, pp. 1861–1868, 2012.

[20] P. V. Sushko, L. Qiao, M. Bowden, T. Varga, G. J. Exarhos, F. K. Urban III, D. Barton, and S. A. Chambers, "Multiband optical absorption controlled by lattice strain in thin-film $LaCrO_3$," *Physical review letters*, vol. 110, no. 7, p. 077401, 2013.

[21] K. Zhang, Y. Du, P. Sushko, M. E. Bowden, V. Shutthanandan, L. Qiao, G. Cao, Z. Gai, S. Sallis, L. Piper, *et al.*, "Electronic and magnetic properties of epitaxial perovskite $SrCrO_3$ (001)," *Journal of Physics: Condensed Matter*, vol. 27, no. 24, p. 245605, 2015.

[22] J.-S. Zhou, C.-Q. Jin, Y.-W. Long, L.-X. Yang, and J. Goodenough, "Anomalous electronic state in $CaCrO_3$ and $SrCrO_3$," *Physical review letters*, vol. 96, no. 4, p. 046408, 2006.

[23] R. Ropp, *Encyclopedia of the Alkaline Earth Compounds*. Elsevier Science, 2012.

[24] A. S. Alexandrov, *Polarons in advanced materials*, vol. 103. Springer Science & Business Media, 2008.

[25] Wikipedia, "*Polaron*." https://en.wikipedia.org/wiki/Polaron, February 20, 2016.

[26] J. T. Devreese, "Optical properties of few and many Fröhlich polarons from 3D to 0D," in *Polarons in Advanced Materials*, pp. 3–61, Springer, 2007.

[27] N. A. Deskins and M. Dupuis, "Electron transport via polaron hopping in bulk TiO_2: A density functional theory characterization," *Physical Review B*, vol. 75, no. 19, p. 195212, 2007.

[28] J. J. Plata, A. M. Marquez, and J. F. Sanz, "Electron mobility via polaron hopping in bulk ceria: a first-principles study," *The Journal of Physical Chemistry C*, vol. 117, no. 28, pp. 14502–14509, 2013.

[29] Y. A. Firsov, "Small polarons: transport phenomena," in *Polarons in Advanced Materials*, pp. 63–105, Springer, 2007.

[30] S. Mildner, J. Hoffmann, P. Blöchl, S. Techert, and C. Jooss, "Temperature-and doping-dependent optical absorption in the small-polaron system $Pr_{1-x}Ca_xMnO_3$," *Physical Review B*, vol. 92, no. 3, p. 035145, 2015.

[31] ABINIT group, "ABINIT - Tutorial on DFT+U," April 28, 2016.

[32] B. Himmetoglu, A. Floris, S. Gironcoli, and M. Cococcioni, "Hubbard-corrected DFT energy functionals: The LDA+U description of correlated systems," *International Journal of Quantum Chemistry*, vol. 114, no. 1, pp. 14–49, 2014.

[33] M. Cococcioni and S. De Gironcoli, "Linear response approach to the calculation of the effective interaction parameters in the LDA+U method," *Physical Review B*, vol. 71, no. 3, p. 035105, 2005.

[34] H. Tasaki, "From Nagaoka's ferromagnetism to flat-band ferromagnetism and beyond: An introduction to ferromagnetism in the Hubbard model," *arXiv preprint cond-mat/9712219*, 1997.

[35] H. Tasaki, "The Hubbard model-an introduction and selected rigorous results," *Journal of Physics: Condensed Matter*, vol. 10, no. 20, p. 4353, 1998.

[36] ABINIT groupe, "ABINIT - What is ABINIT ?," May 5, 2016.

[37] F. Jollet, M. Torrent, and N. Holzwarth, "Generation of Projector Augmented-Wave atomic data: A 71 element validated table in the XML format," *Computer Physics Communications*, vol. 185, no. 4, pp. 1246–1254, 2014.

[38] A. Jain, S. P. Ong, G. Hautier, W. Chen, W. D. Richards, S. Dacek, S. Cholia, D. Gunter, D. Skinner, G. Ceder, and K. A. Persson, "The Materials Project: A materials genome approach to accelerating materials innovation," *APL Materials*, vol. 1, no. 1, p. 011002, 2013.

[39] W. Setyawan and S. Curtarolo, "High-throughput electronic band structure calculations: Challenges and tools," *Computational Materials Science*, vol. 49, no. 2, pp. 299–312, 2010.

[40] J. L. Hughes and J. Sipe, "Calculation of second-order optical response in semiconductors," *Physical Review B*, vol. 53, no. 16, p. 10751, 1996.

[41] S. Sharma and C. Ambrosch-Draxl, "Second-harmonic optical response from first principles," *Physica Scripta*, vol. 2004, no. T109, p. 128, 2004.

[42] R. Nunes and X. Gonze, "Berry-phase treatment of the homogeneous electric field perturbation in insulators," *Physical Review B*, vol. 63, no. 15, p. 155107, 2001.

[43] L. Piraux, *MAPR1492 - Materials physics*, 2013.

[44] D. Flandre and V. Bayot, *ELEC1330 - Physics of electronics*, 1994.

[45] J.-C. Charlier and L. Piraux, *LMAPR2471 - Transport phenomena in solids and nanostructures*, 2014–2015.

[46] G.-M. Rignanese, J.-C. Charlier, and X. Gonze, *LMAPR2451 - Atomistic and nanoscopic simulations*, 2014–2015.

[47] Wikipedia, "*Density Functional Theory*." https://en.wikipedia.org/wiki/Density_functional_theory, April 12, 2015.

[48] P. E. Blöchl, "Projector augmented-wave method," *Physical Review B*, vol. 50, no. 24, p. 17953, 1994.

[49] G. Kresse and D. Joubert, "From ultrasoft pseudopotentials to the projector augmented-wave method," *Physical Review B*, vol. 59, no. 3, p. 1758, 1999.

Rue Archimède, 1 bte L6.11.01, 1348 Louvain-la-Neuve **www.uclouvain.be/epl**